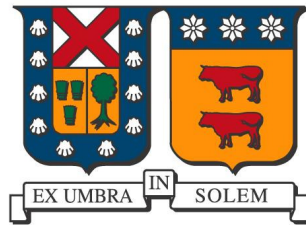


Universidad Técnica Federico Santa María



Departamento de Física

A thesis submitted for the degree of Magister en Ciencias,
Mención Física

Propagating spin-wave normal modes on extended ferromagnetic nanostructures

Pablo Alvarado Seguel

Supervisor Rodolfo Gallardo

March 2022



AUTORIZACIÓN PARA PUBLICAR MONOGRAFÍA ACADÉMICA

1.- Identificación del Autor

Nombre del Autor(a): Pablo Alvarado Seguel
 Carrera: Magister en ciencias, mención física RUT: 19.488.374-9
 Teléfono/Celular: 9 9543 9817 E-mail: pablo.alvarados@sansano.usm.cl
 Dirección: Paris 1190, Viña del Mar

2.- Identificación de la Publicación

Título de la Publicación: Propagating spin-wave normal modes on extended ferromagnetic nanostructures

Campus/Sede: Casa central Departamento/Área: Física
 Carrera: Magíster en ciencias, mención física Profesor Guía: Rodolfo Gallardo
 Palabras Clave (separar por comas): Spinwaves, ferromagnetism

Uso interno Biblioteca

Código de barra: Fecha de Ingreso a RI:

3.- Autorización a Publicar

En conformidad a las Leyes 17.336 sobre "Propiedad Intelectual" y 20.435 que modifica la anterior, en mi calidad de Autor de la obra antes identificada, informo a la Dirección de Información y Documentación Bibliográfica Institucional (DIDBI) mi decisión acerca de publicar en formato digital mi **Monografía Académica (Tesis/Trabajo de Título/Memoria)**:


Autorizo a que se publique en (favor marcar con X una de las categorías):

<input checked="" type="checkbox"/>	A. Internet abierta www.repositorio.usm.cl y otros repositorios a que la USM se adscriba
<input type="checkbox"/>	B. Solamente disponible para consulta en sala (opción por defecto)
<input type="checkbox"/>	C. Documento con embargo de publicar hasta(mes/año).

4.- Unidad Académica avala la publicación

El Profesor Guía que suscribe en representación del Departamento/Carrera, en virtud de la calidad técnica y originalidad del documento, determina (marcar con X una opción) Si No, respaldar, la publicación abierta en Internet, o el embargo solicitado, dadas las siguientes razones:

.....

Fecha: 13/09/2023	Nombre:	Nombre: Uso interno
	Fecha:	Fecha:
Firma:	Firma:	Firma:
Firma del Autor y Fecha	Profesor Guía	Catalogador Monografía

Pablo Alvarado Seguel

Propagating spin-wave normal modes on extended ferromagnetic nanostructures

A thesis submitted for the degree of Magister en Ciencias, Mención Física, March 2022

Committee: Pedro Landeros, Rodrigo Arias, Patricio Guzmán and Alejandro Roldán-Molina

Supervisor: Rodolfo Gallardo

Universidad Técnica Federico Santa María

Departamento de Física

Av. España 1680, Valparaíso, Chile

A la memoria de Aurelio

Abstract

In this master thesis we develop a versatile computational tool, the Dynamic Matrix Method, that enables a systematic study of the propagating spin waves normal modes of a wide class of extended ferromagnetic nanostructures. A generalization of the method to account for magnonic crystals is included. We provide a detailed analytical treatment of the magnetic dipole-dipole interaction. The method was applied in the study of different kinds of magnetic systems, with an emphasis on understanding the physics behind spin wave non-reciprocal phenomena. The results obtained in this work showcase the potential of the Dynamic Matrix Method as a powerful research tool in magnonics and other related areas.

Agradecimientos

A Rodolfo Gallardo, por incentivar-me a dar mis primeros pasos en el mundo de la investigación científica. A Pedro Landeros, por su accesibilidad y buena disposición.

A Mateo Barría y Valentina Gallardo, por todas las veces que deambulamos sin rumbo por la ciudad, por los cafés compartidos en tiempos de pandemia. A mis amigos, cuya compañía me mantuvo cuerdo durante la redacción de este manuscrito. A mis compañeros de pregrado en física, junto a quienes cohabité la madriguera, que a ratos se sentía como un (estrecho) segundo hogar. Un agradecimiento especial a Gabriel Gray, por acerme entrega a último minuto del formato usado en esta tesis.

A mi padre, Claudio, por no perder oportunidad en recordarme que no estaba trabajando en mi tesis. A mi madre, Verónica, por lo contrario.

A los proyectos FONDECYT 1161403 y 1210607, por financiar esta investigación. A la Beca de arancel de la UTFSM y al Programa Incentivo a la Iniciación Científica de la UTFSM.

Contents

1	Introduction	1
2	Micromagnetism	7
2.1	Basic concepts	8
2.2	Dynamics	10
2.2.1	Spin precession	10
2.2.2	Landau-Lifshitz equation	11
2.3	Energies and fields	13
2.3.1	Zeeman interaction	14
2.3.2	Anisotropy interaction	14
2.3.3	Exchange interaction	15
2.3.4	Dipolar interaction	17
3	Dynamic Matrix Method	21
3.1	Eigenvalue Problem	22
3.1.1	Continuous Symmetry	23
3.1.2	Discrete Symmetry	24
3.2	Effective Fields	26
3.2.1	Exchange Interaction	26
3.2.2	Dipolar Interaction	27
4	Applications of the theory	35
4.1	Spin-wave non-reciprocity in magnetization-graded ferromagnetic films	36
4.2	Band structure of a one-dimensional bilayer magnonic crystal	44
4.3	Spin-wave focusing induced by dipole-dipole interaction in synthetic antiferromagnets	56

4.4 Propagation of localized spin-wave modes within magnetization-graded stripes	66
5 Conclusions and Perspectives	75
Bibliography	77



Introduction

Magnonics is a young field of research in condensed matter physics with a strong interdisciplinary character that nourishes from the conversation of fundamental research in magnetism, the design of metamaterials, and the perspective of future technological applications. It is mainly concerned with magnons (the quanta of spin waves), and their use for transmitting, storing, and processing information. Its object of study, spin waves, are collective excitations of the magnetic order. The propagation of spin waves has a precessional nature mediated by an array of physical processes that emanate from the interactions of the underlying atomic magnetic moments. Here, the interplay between the short-range exchange interaction and the non-local magnetic dipole-dipole interaction plays a predominant role. Spin-waves can exhibit complex band-structures and various ways of manipulating their behavior, which represent the main attraction for the scientific community. Among their many salient features, spin waves have a strong anisotropic dispersion. For example, in an in-plane magnetized ferromagnetic thin film, the spectra of the spin waves differ significantly depending on whether the propagation is parallel (backward volume modes) or perpendicular (Damon-Eshbach modes) to the equilibrium magnetization. Moreover, spin waves have the ability to transport energy and angular momentum without the motion of electrons, which enables Joule-heat-free transport at high frequencies [1]–[4]; they have the potential to operate over a wide range of frequencies with a large group velocity; and their wavelengths can also be much shorter than the electromagnetic waves at the same gigahertz frequency [5], thereby offering excellent prospects for magnonic-device miniaturization [6]. The interdisciplinary aspects of the broad field of magnonics are summarized in some excellent works that highlight the role of spin waves in different areas like magnon spintronics [2], [7], spin caloritronics [8], magnonic logic circuits [9], [10], metamaterials and magnonic crystals [10]–[12], spin textures [13], [14], magnonic-phononic crystals [15], [16], among others.

With the hopes of developing magnonic devices at the nanoscale as a viable alternative to electronics, fueled by promises of technological breakthroughs, a surge of current research has been directed to the spin-wave properties of magnetic nanostructures. There is an ongoing exploration in search of novel behaviors and ways to tinker known properties of spin waves, a necessary step for envisioning and designing magnonic devices, where non-reciprocal phenomena play a pivotal role. Frequency non-reciprocity (a situation where the wave dispersion depends on the sign of the wave vector), in particular, opens the gate for spin-wave caustics with highly non-reciprocal focusing patterns, the excitation of non-trivial localized modes, and motivates the investigation of magnonic crystals. An overview of the topics mentioned above is given in the following paragraphs. These topics will highlight the need for flexible theoretical tools for solving and understanding, in a systematic way, the spin-waves dynamics of a wide range of magnetic systems.

To begin with, non-reciprocal spin-wave propagation has been observed in magnetic systems with broken symmetries, where two counter-propagating waves exhibit different dynamic features (amplitude, frequency, or phase) at the same wave vector magnitude. A great variety of magnonic structures manifest this non-reciprocal effect [17], such as heavy-metal/ferromagnet interfaces [18]–[24], non-centrosymmetric chiral magnets [25]–[30], curvilinear magnetic shells [31], [32], magnetization-graded ferromagnetic films [33], ferromagnetic bilayers [4], [14], [34]–[42], bilayered magnonic crystals [43], [44], and arrays of magnetic nanopillars coupled by dipolar interaction [45], among others. From a technological point of view, non-reciprocity turns out fundamental to envision magnonic applications, for instance, in circulators, isolators, phase shifters, and logic devices [46]–[50]. Indeed, under proper conditions, the non-reciprocal magnon propagation can even be forbidden in one direction, and the system may behave as a magnonic diode [14], [34], [47]. In most of these systems, the origin of the non-reciprocity lies in the dipole-dipole interaction, while in ferromagnet/heavy-metal bilayers and non-centrosymmetric crystals, the cause can be found in the Dzyaloshinskii-Moriya interaction, which is outside the scope of this thesis. In antiferromagnetically coupled bilayers (synthetic antiferromagnets), an appreciable non-reciprocity in frequency is observed due to the dynamic dipolar interaction [4], [14], [34]–[42], [50]. This non-reciprocity can be comparable to the one induced by the interfacial

Dzyaloshinskii-Moriya interaction in thin ferromagnetic layers, but it becomes more prominent for thick films [42], [50].

Moving on, in optics, the concept of caustics is linked to enveloped rays, which can be achieved either through reflection or refraction in curved objects [51]–[53]. Caustics have been extensively studied in several fields of mathematics, and theoretical physics [54]–[57], and also in the main fields of condensed matter physics, such as phononics [58]–[62], plasmonics [63], [64], electronics [65]–[68] and magnonics [68]–[78]. In such cases, one relevant physical ingredient is the anisotropy of the system, which causes the group velocity to point in a different direction compared to the phase velocity of the associated wave. In the context of spin-waves, highly focused beams have been observed [68]–[79], where non-reciprocity is an essential feature for creating and controlling caustic spin waves. The spin-wave asymmetry causes a crucial modification in the iso-frequency curve formed in the wave-vector space, where caustics appear at points at which its curvature is zero, resulting in a divergence in the power flow [77]. Nevertheless, even when the curvature is small, but nonzero, a substantial focusing of the energy can also be reached (we speak of caustic-like or focalized waves) [70], [78].

Next, spin waves are susceptible to the magnetic texture and the internal field landscape, and hence they are prone to propagate in a localized way. If the magnetic material presents a domain wall (a kind of texture), localized modes are excited and channeled along the domain wall center [4], [79]–[84]. However, the channeling of spin waves may be compromised if the magnetic texture changes, making the stability of the domain wall a problem. Another example is given by a magnetic system with one or two finite dimensions, for which the demagnetizing field is reduced at the edges, and, consequently, edge modes are excited [85]–[87]. It should be noted that such edge modes may be challenging to detect due to the small regions of the magnet where the spins are precessing. Nonetheless, these drawbacks can be overcome by proper material manipulation, where a gradual change in some magnetic parameters may be the key to the steering of spin-waves without relying on unstable domain walls or low cross-section edge modes. In these cases, the propagation of waves can be confined to nano-scale channels, which is fundamental for the development of magnonic devices [47]–[49], [70], [78], [88], [89]. Exploring gradual changes in a given physical property is not a

new business. Indeed, inside a conventional step-index optical fiber, the index of refraction is controlled using different dielectric materials, usually with a high-index core covered with another material of smaller index [90], which allows channeling the light due to the total internal reflection phenomenon [91]. In graded-index optical fibers, the index of refraction changes continuously and is more noticeable at the center of the dielectric material, which helps to bend the light into the fiber axis [92], [93]. A similar phenomenon should be expected for spin waves, as has been observed at the interface of materials with different saturation magnetization [94]–[96]. However, owing to their strongly anisotropic nature, the refraction of spin-waves is a highly nontrivial issue that depends on several factors such as the frequency, angle of incidence, magnetic parameters or external field [97], [98]. Indeed, under proper conditions, the refraction can even be negative [96], [99], [100]. In the realm of graded-index magnonics, the main idea is to manipulate the internal field landscape to create potential wells that allow steering the spin-waves [98], [101]. This graduation can be realized in several ways, for instance, by changing the applied field, magnetic parameters, or shape of the material. For finite nano-magnets, the nonuniform demagnetizing field creates the proper conditions to channel spin waves because the internal field acts as a confining potential well, leading to wave localization [102]–[106] and mode quantization [107], [108]. It is also possible to manipulate the already nonuniform internal field by introducing gradual changes in the magnetization saturation [109]–[111]. Other graded-index magnonics systems have been fabricated, with graduation either in the anisotropy constant [112]–[115], or in the exchange coupling strength [116]–[118].

Finally, magnetic materials with periodically modulated properties (magnonic crystals) represent another venue of research with promising perspectives of data processing applications [2], [9], [12]. The spin-wave spectra of magnonic crystals exhibit well-defined frequency band-gaps, frequency intervals over which the propagation of waves is forbidden, which sets them apart from other non-periodic systems. An essential advantage of magnonics crystals lies in its incredible repertoire of possible designs [2]. For instance, magnonic crystals can be created by modulating the geometry [119]–[128], the magnetic properties [129]–[138] or by coupling different systems [24], [139]–[141]. In two-dimensional bicomponent magnonic crystals, it has been experimentally demonstrated that the spin-wave spectra change significantly depending upon the direction of the external bias field

[137]. The magnonic band gaps in these crystals can also be controlled by the filling fraction, the lattice constant, and the applied magnetic field [133], [134], [137]. For dipolar spin waves (crystals with large lattice constants), the widths and center frequencies of the band gaps decrease and increase, respectively, with increasing applied magnetic field [129], [131], [133], while in the case of exchange spin waves (small lattice constant), the band-gap widths are independent of the field strength [134]. All in all, this vast array of properties illustrated in the previous paragraphs open up many opportunities for engineering magnonic bands.

In this thesis, we are interested in the theoretical study of the normal modes of propagating spin waves along the symmetry axes of certain kinds of extended ferromagnetic nano-structures (stripes and layers). Our theoretical inquiry proceeds in the framework of micromagnetism under the lenses of a semi-analytical theory called the Dynamic Matrix Method. Roughly speaking, this method is a way to extend solutions of low-dimensional systems to 3D systems in the form of finite-dimensional eigenvalue problems. In a sense, this theoretical method is similar to what is done in micromagnetic simulations. However, this method exploits the assumed physical symmetries to maintain a distinctive theoretical character and thus should not be thought of as a merely numerical tool. Hence, the purpose of this thesis is to develop the Dynamic Matrix Method, extend it to tackle periodic systems (adapting the so called Plane Wave Method), and then apply it to solve the spin-wave dynamics of many ferromagnetic nanostructures in different coupling configurations. For example, we study how the non-reciprocal phenomena in a ferromagnetic film can be modified by grading its magnetization saturation or how the band gaps in a coupled bilayer magnonic crystal are affected by modifying its geometric parameters. Among the systems explored in this thesis, we found magnetization-graded ferromagnetic films and stripes, coupled bilayer magnonic crystals, and synthetic antiferromagnets, for which various properties are studied such as frequency non-reciprocity, band gaps, localization, and focalization of waves. The relevance of this work lies in the development of a versatile theoretical tool that is able to describe the spin-wave dynamics of a wide range of magnetic systems: thick or thin, with uniform or graded parameters, or even magnonic crystals; among various possible geometric and coupling configurations. When we speak of versatility, we do not refer exclusively to the scope of applications as previously illustrated, but also to the relative ease with which the method can

be extended to consider other kinds of systems and interactions, fertile ground for future research, as we discuss in chapter 5. Although similar results can be obtained from micromagnetic simulations, the semi-analytical character of the Dynamic Matrix Methods allows, on the one hand, to heavily cut down the required computational time, and on the other, to contrast the numerical results with analytical expressions for the different interactions, as is demonstrated in chapter 4. The calculations found in chapter 3, related to the Dynamic Matrix Method, are the main result of the thesis work.

The thesis is organized as follows. In chapter 2 a brief overview of micromagnetism is given, followed by a discussion of spin-waves dynamics and its underlying interactions in the micromagnetic regime. Chapter 3 gives a detailed treatment of the Dynamic Matrix Method and its extension to periodic systems. Chapter 4 shows how the above method can be applied in current research in magnonics, such as the study of i) spin-wave frequency non-reciprocity in magnetization-graded ferromagnetic films, ii) the magnon band structure of a coupled bilayer magnonic crystal, iii) spin-wave focusing in synthetic antiferromagnets, and iv) the propagation of localized spin-wave modes within magnetization-graded stripes. Finally, chapter 5 presents the conclusions of the thesis work and offers perspectives for future lines of research.

Micromagnetism

Micromagnetism is a mesoscopic theory of magnetism. That is, a theory concerned with a medium scale between atomic and bulk physics, usually in the nanoscale. We say that a theory or calculation about magnetic matter is micromagnetic when the atomic structure is ignored in favor of a continuum approach. Micromagnetism, then, stands as a translation from quantum to classical physics. The classical framework enables further analysis of inherently quantum mechanical phenomena, such as spin and magnetic order, that does not yield easily to theoretical developments in its original quantum description. In practice, we are trading the difficulties brought about by noncommutative algebras for the nonlinearity of partial differential equations. However, the trade-off is particularly convenient when dealing with the Dynamic Matrix Method, the main topic of this thesis (see Chapter 3).

The Landau-Lifshitz equation can correctly describe the dynamics of spin waves in ferromagnetic nanostructures. In this differential equation, an effective field captures the various physical processes by which the magnetic moments interact between them and with their environment. We consider four kinds of interactions: (i) Zeeman, (ii) anisotropy, (iii) dipolar, and (iv) exchange. The Zeeman interaction refers to the coupling of a magnetic moment with an external field. Anisotropy is a (phenomenological) umbrella term that considers the atomic and macroscopic structure of the material. The dipolar interaction refers to the classical magnetic dipole-dipole interaction. Exchange, like spin, is an inherently quantum phenomenon and has no classical analog. For the moment, it is enough to think of it as strongly coupling spins parallel to each other. In this chapter, we motivate the Landau-Lifshitz equation using variational methods. Also, we show how the underlying interactions can be taken to the continuum and written as an effective field in the micromagnetic approach.

Regarding the organization of this chapter. First, in Section 2.1 we review some basic concepts of magnetism. Then, in Section 2.2 we study the dynamics of spin waves. Finally, in Section 2.3 we consider the Zeeman, anisotropy, exchange, and dipolar interactions.

2.1 Basic concepts

The fundamental concept in the study of magnetic materials is the magnetic moment μ . In an atom, this vector quantity has two contributions: (i) orbital angular momentum, related to the spatial symmetries of charged particles (think of a current loop), and (ii) spin angular momentum, related to the internal symmetries of particles. Hence we write $\mu = \gamma\mathbf{J}$, where γ is the gyromagnetic ratio and \mathbf{J} the total angular momentum.

One way of classifying magnetic materials is to look at their response to an external magnetic field. In most cases, the magnetic moments are the only relevant contributions to the atomic magnetic moment. It turns out that, under an applied external field, the electronic (orbital) spin magnetic moment aligns (anti-) parallel to the field, which later gives rise to what is called (diamagnetic) paramagnetic behavior. In weakly interacting systems, the bulk behavior depends exclusively on the interplay of these two opposing tendencies. As a general rule, when the atomic magnetic moment ground state is not zero, paramagnetism is the significant contribution, and we see a net magnetization parallel to the applied field. In such a case, we speak of a paramagnetic material. On the other hand, if the atomic magnetic moment ground state is zero, the atomic spin must be zero; thus, there is no paramagnetism, so that diamagnetism prevails, and we see a net magnetization antiparallel to the applied field. Hence, we speak of a diamagnetic material. In both cases, there is no spontaneous magnetization at zero applied field. In contrast to the previously discussed systems, ferromagnets present a spontaneous magnetization at zero applied field. This effect is present because the exchange interaction strongly couples the atomic magnetic moments in ferromagnets. In these materials, exchange favors a ground state of (locally) parallel spins, allowing for long-range magnetic order, i.e., spontaneous magnetization. Ferromagnetism is, in fact, a state of magnetic matter,

with a phase transition at high temperatures, where spontaneous magnetization is lost. Thus, in the process of cooling a hot ferromagnet, there is a transition from a state of high symmetry (magnetic moments are oriented randomly and isotropically) to a state of lower symmetry (magnetic moments align themselves parallel to an arbitrary direction). The temperature at which certain magnetic materials undergo such a change of their magnetic properties is called *Curie Temperature*. This transition is an example of spontaneous symmetry breaking.

We are interested in ferromagnetic materials (e.g., Permalloy, Cobalt, and Nickel). Depending on the prevalent behavior of the electrons on a ferromagnet, two kinds of models are available for their description: localized and itinerant magnetism. In the localized models, the ferromagnet is seen as a fixed lattice of magnetic moments (i.e., each electron is attached to an atom). On the contrary, itinerant models consider conduction electrons that generate displaced bands that, in the end, are responsible for magnetization. In this thesis, we work with localized models of magnetism in the micromagnetic regime.

In the continuum limit, we work with a magnetization density $\mathbf{M} : \mathbf{R}^3 \rightarrow \mathbf{C}^3$, defined as the mesoscopic average of the magnetic moments $\boldsymbol{\mu}$ in a lattice. Namely, $\mathbf{M}(\mathbf{r}) = \sum_{\Delta V} \boldsymbol{\mu} / \Delta V$, where ΔV is a volume centered at \mathbf{r} that is big enough to ignore the discrete nature of the lattice but small enough for other interactions, aside from exchange, to play a significant role. At microscopic scales, exchange reigns supreme, as it is by far the strongest interaction, aligning all magnetic moments parallel to each other in their vicinity. This, save some pathological cases, justifies thinking of \mathbf{M} as a continuous function. As we zoom out and pass thorough the nanoscale, other forces begin to exert their influence. For example, the magnetic dipole-dipole interaction would rather have the magnetic moments oriented in such a way as to form closed magnetic loops. This energetic competition forces the magnetization to bend, forming textures and domain walls. In general, the magnitude of the magnetization, $M = |\mathbf{M}|$, is temperature dependent (heat provokes random misalignments from the ground state). In this thesis, however, we will always remain in the low-temperature regime, and thus take M to equal the saturation magnetization M_S of the material (the maximum magnetization that can be achieved in a ferromagnet). Complex functions are assumed from the beginning, as they facilitate the symbolic manipulations.

2.2 Dynamics

For our purposes, a magnon is an excitation of the ground state ferromagnetic order (picture a lattice of aligned magnetic moments where one of them flips). In the context of low temperature and low energy excitations, we refer to the (macroscopic) collective excitations of the ferromagnetic order (or magnetization, in the micromagnetic regime) as *spin waves*. A natural question to ask is, how do these waves propagate in a given magnetic material? We start an answer by pondering about the dynamics of a spin under an external magnetic field, then deviating a bit by considering the related question of what is the ground state of a ferromagnet, and then coming up with an answer in the form of a differential equation.

2.2.1 Spin precession

Consider a single fixed spin \mathbf{S} under an external magnetic field \mathbf{H} . The Hamiltonian is known to be $\mathcal{H} = -\gamma\mu_0\mathbf{S} \cdot \mathbf{H}$, with γ being the absolute value of the gyromagnetic ratio. In the Heisenberg picture of quantum mechanics, the time evolution of the spin operator \mathbf{S} is given by $d\mathbf{S}/dt = i[\mathcal{H}, \mathbf{S}]$. From the commutation relation $[\mathbf{S} \cdot \mathbf{H}, \mathbf{S}] = i\gamma\mathbf{S} \times \mathbf{H}$, it follows that

$$\frac{d}{dt}\mathbf{S} = -\gamma\mu_0\mathbf{S} \times \mathbf{H}. \quad (2.1)$$

Now that we have derived the dynamical equation for the spin operator, we switch to a classical description; that is, we treat operators as if they were vector variables. The dynamical equation tells us that, for a constant field \mathbf{H} , the spin \mathbf{S} precesses around the axis defined by \mathbf{H} with constant magnitude S . The equilibrium condition, $d\mathbf{S}/dt = 0$, is given by $\mathbf{S} \times \mathbf{H} = 0$. In particular, since the energy is equal to $-\gamma\mu_0\mathbf{S} \cdot \mathbf{H}$, the only stable equilibrium, a configuration that (locally) minimizes energy, corresponds to the spin being aligned parallel to the external field.

Now, we consider a harmonic linear perturbation around the stable equilibrium \mathbf{S}_{eq} . Namely, $\mathbf{S}(t) = \mathbf{S}_{\text{eq}} + \mathbf{s}e^{i\omega t}$, where \mathbf{s} is a vector coefficient perpendicular to \mathbf{S}_{eq} . Replacing in the dynamical equation, to first order in \mathbf{s} , we have that

$$\omega \mathbf{s} = i\gamma\mu_0 \mathbf{H} \times \mathbf{s}. \quad (2.2)$$

This equation represents an eigenvalue problem on \mathbf{s} , with the associated characteristic equation

$$\det \begin{vmatrix} \omega & i\gamma H \\ -i\gamma H & \omega \end{vmatrix} = 0, \quad (2.3)$$

which has $\omega = \gamma H$ as a physical solution. Regarding the role of damping, we consider the modified dynamic equation

$$\frac{d}{dt} \mathbf{S} = -\gamma\mu_0 \mathbf{S} \times \mathbf{H} + \alpha \mathbf{S} \times \frac{d}{dt} \mathbf{S}, \quad (2.4)$$

where α is a phenomenological (fixed by experiment) damping parameter. Doing the same linear perturbation, we see that solving the modified eigenvalue problem is equivalent to making the substitution $H \mapsto H + i\omega\alpha S_{\text{eq}}/\gamma$ in the previous characteristic equation, and hence $\omega \mapsto \beta\omega$, where $\beta = (1 + i\alpha S_{\text{eq}})/(1 + \alpha^2 S_{\text{eq}}^2)$. Performing a series expansion on α , we have that $\text{Re}(\beta) = 1 - \alpha^2 S_{\text{eq}}^2$. This last term suggests that, regarding the study of normal modes, damping is a second-order perturbation and is henceforth omitted in this thesis.

2.2.2 Landau-Lifshitz equation

This section considers the general problem of equilibrium in a magnetic solid with constant saturation magnetization, see the books by Gurevich et al. [5] and Aharoni [142]. We seek conditions that (a well-behaved) magnetization function must satisfy to guarantee an equilibrium configuration. In particular, we are interested in the extrema of the energy functional. This is a task most suited to the calculus of variations.

For simplicity, instead of working with the magnetization function, we will use an arbitrary function and later make the required substitutions. Henceforth we omit

the use of differentials in integral expressions, as their use is clear from the context. Consider a functional U given by

$$U(\boldsymbol{\eta}) = \int_{\Omega} u(\boldsymbol{\eta}, \nabla \boldsymbol{\eta}) + \oint_{\partial\Omega} w(\boldsymbol{\eta}), \quad (2.5)$$

where u is an energy density, w is a superficial energy density, and $\boldsymbol{\eta} : \mathbf{R}^3 \rightarrow \mathbf{R}^3$ is a well-behaved function under the constraint $\eta = 1$. This is formally the same as deriving the Lagrange equations of a constrained mechanical system from Hamilton's Principle of Least Action. Following the approach outlined in Lemos [143], let $\Phi : \mathbf{R} \rightarrow \mathbf{R}$ be a real function such that $\Phi(\epsilon) = U(\boldsymbol{\eta} + \epsilon \bar{\boldsymbol{\eta}})$ for $\epsilon > 0$, where $\bar{\boldsymbol{\eta}} : \mathbf{R}^3 \rightarrow \mathbf{R}^3$ is a well-behaved function, and let $\delta U / \delta \boldsymbol{\eta} = (d\Phi/d\epsilon)_{\epsilon=0}$ be the functional derivative of U respect to $\boldsymbol{\eta}$. We have that

$$\left(\frac{d\Phi}{d\epsilon} \right)_{\epsilon=0} = \int_{\Omega} \left(\frac{\partial u}{\partial \boldsymbol{\eta}} \cdot \bar{\boldsymbol{\eta}} + \frac{\partial u}{\partial (\nabla \boldsymbol{\eta})} : \nabla \bar{\boldsymbol{\eta}} \right) + \oint_{\partial\Omega} \frac{\partial w}{\partial \boldsymbol{\eta}} \cdot \bar{\boldsymbol{\eta}}, \quad (2.6)$$

$$= \int_{\Omega} \left(\frac{\partial u}{\partial \boldsymbol{\eta}} - \nabla \cdot \frac{\partial u}{\partial (\nabla \boldsymbol{\eta})} \right) \cdot \bar{\boldsymbol{\eta}} + \oint_{\partial\Omega} \left(\hat{\mathbf{n}} \cdot \frac{\partial u}{\partial (\nabla \boldsymbol{\eta})} + \frac{\partial w}{\partial \boldsymbol{\eta}} \right) \cdot \bar{\boldsymbol{\eta}}. \quad (2.7)$$

Due to the constraint $\eta = 1$ the spatial components of the variation $\bar{\boldsymbol{\eta}}$ are not independent. We use the Lagrange multipliers method to take this into account. The constraint $\eta = 1$ holds over any variation of η , in particular $|\boldsymbol{\eta} + \epsilon \bar{\boldsymbol{\eta}}|^2 = 1$. It follows that $(d\Phi/d\epsilon)_{\epsilon=0}$ remains invariant inde the substitution $\Phi \mapsto \Phi' = \Phi + \lambda \epsilon \int_{\Omega} \boldsymbol{\eta} \cdot \bar{\boldsymbol{\eta}}$, where $\lambda \in \mathbf{R}$ is the Lagrange multiplier. By imposing the equilibrium condition $\delta U / \delta \boldsymbol{\eta} = 0$ and making the substitution $\Phi \mapsto \Phi'$ it follows [143] that the equilibrium configuration of $\boldsymbol{\eta}$ must satisfy the differential equation

$$\frac{\partial u}{\partial \boldsymbol{\eta}} - \nabla \cdot \frac{\partial u}{\partial (\nabla \boldsymbol{\eta})} + \lambda \boldsymbol{\eta} = 0, \quad (2.8)$$

with boundary condition

$$\hat{\mathbf{n}} \cdot \frac{\partial u}{\partial (\nabla \boldsymbol{\eta})} + \frac{\partial w}{\partial \boldsymbol{\eta}} = 0. \quad (2.9)$$

Taking the vector product of the above equations with $\boldsymbol{\eta}$ and then setting $\boldsymbol{\eta} = \mathbf{M}/M_s$, we obtain Brown's equations of equilibrium:

$$\mathbf{M} \times \left(\frac{\partial u}{\partial \mathbf{M}} - \nabla \cdot \frac{\partial u}{\partial (\nabla \mathbf{M})} \right) = 0, \quad (2.10)$$

for $\mathbf{M} \in \Omega$, and

$$\mathbf{M} \times \left(\hat{\mathbf{n}} \cdot \frac{\partial u}{\partial (\nabla \mathbf{M})} + \frac{\partial w}{\partial \mathbf{M}} \right) = 0, \quad (2.11)$$

for $\mathbf{M} \in \partial\Omega$. We note that Brown's equations are a necessary but not sufficient condition for stable equilibrium. Henceforth, we will assume that every equilibrium is stable unless otherwise stated.

Comparing Brown's (bulk) equation with the condition of equilibrium of spin precession in section 2.1, we see that the magnetic field \mathbf{H} can be replaced by an effective field

$$\mu_0 \mathbf{H}_{\text{eff}} = -\frac{\partial u}{\partial \mathbf{M}} + \nabla \cdot \frac{\partial u}{\partial (\nabla \mathbf{M})}, \quad (2.12)$$

where care was taken with the sign of the expression so that $\mu_0 \mathbf{H} = -\partial u / \partial \mathbf{M}$ in the case of an external field. This definition motivates us to postulate an analogous replacement in the equation of motion. Thus, we obtain the Landau-Lifshitz equation of motion

$$\frac{d}{dt} \mathbf{M} = -\gamma \mathbf{M} \times \mathbf{H}_{\text{eff}}. \quad (2.13)$$

In what follows, we denote the effective field simply by \mathbf{H} .

2.3 Energies and fields

The manifestation of magnetic properties in condensed matter can be explained by the collective behavior of magnetic moments. This section will describe some of the different types of interactions by which magnetic moments interact between them and their environment. These interactions are first considered in a discrete system (localized magnetism) and then transferred to the continuum (micromagnetic regime). We follow the treatment given by Aharoni [142].

2.3.1 Zeeman interaction

The energy of a magnetic moment $\boldsymbol{\mu}$ in an applied magnetic field \mathbf{H}_Z , called Zeeman interaction, is given by $E_Z = -\boldsymbol{\mu} \cdot \mathbf{H}_Z$. Thus, in the micromagnetic regime, the Zeeman energy of a ferromagnet Ω is given by

$$E_Z = -\mu_0 \int_{\Omega} \mathbf{M} \cdot \mathbf{H}_Z. \quad (2.14)$$

It is easy to see that the formula for the effective field does indeed give the desired answer.

2.3.2 Anisotropy interaction

The anisotropy energies are associated with preferential directions of the magnetization. There exist various kinds of anisotropy, the most common being the magnetocrystalline anisotropy due to the spin-orbit interaction. Electronic orbits are constrained to the crystal lattice, and due to their interactions, spins prefer to align in specific directions. Thus, there are directions in which it is easier to magnetize a crystal. This difference is expressed as a direction-dependent energy term. Usually, the magnetocrystalline energy is weak compared to the exchange energy. However, since the exchange is isotropic, the magnetization's direction is uniquely determined by the anisotropy and the ferromagnet's shape (dipolar interaction). Although first principle computations for the spin-orbit interaction are feasible, as with the exchange integrals, their precision is not always adequate. Thus, the anisotropy energies are written as phenomenological expressions, power series that consider the crystal symmetry, whose coefficients are taken from experiment. Individual expressions can be written for only some crystal symmetries.

The anisotropy of a hexagonal crystal, called uniaxial anisotropy, is a function of only one parameter, the angle between the a -axis and the magnetization. It is an experimental fact that the energy is symmetric concerning the (perpendicular) plane of the hexagonal lattice, so that odd powers of the cosine of the angle can be discarded from the energy series expansion. For cubic crystals, we talk of cubic anisotropy. The series expansion should be invariant under permutations of the

crystallographic axes $\mathbf{c}_1, \mathbf{c}_2, \mathbf{c}_3$ (with $\mathbf{c}_i \cdot \mathbf{c}_j = \delta_{ij}$). Again, odd powers are discarded. Also, the lowest-order combination, $\sum_{i=1}^3 (\mathbf{M} \cdot \mathbf{c}_i)^2 = M_s^2$, is a constant, and hence is omitted. The combined energy series expansion, to the first non-vanishing order, is then given by [144]

$$E_a = -\frac{K_u}{\mu_0 M_s^2} \int_{\Omega} (\mathbf{M} \cdot \mathbf{a})^2 + \frac{K_c}{\mu_0 M_s^4} \int_{\Omega} \sum_{i=1}^3 \left[\sum_{j \neq i} (\mathbf{M} \cdot \mathbf{c}_j)^2 \right] (\mathbf{M} \cdot \mathbf{c}_i)^2. \quad (2.15)$$

Here the first term accounts for a uniaxial anisotropy of constant K_u , while the second stands for a cubic anisotropy of constant K_c . In a lot of hexagonal crystals, the \mathbf{a} -axis is an easy axis ($K_u > 0$); that is, the energy is minimized when the magnetization is parallel to \mathbf{a} . If $K_c > 0$, the easy axes are the cubic crystallographic axes. While, if $K_c < 0$, the easy axes are along the crystal diagonals (e.g. the (111) direction).

The effective anisotropy field is given by $\mu_0 \mathbf{H}_a = -\partial u_a / \partial \mathbf{M}$, where u_a is the anisotropy energy density ($E_a = \int_{\Omega} u_a$). Thus,

$$\mathbf{H}_a = \frac{2K_u}{\mu_0^2 M_s^2} (\mathbf{M} \cdot \mathbf{a}) \mathbf{a} - \frac{2K_c}{\mu_0^2 M_s^4} \sum_{i=1}^3 \left[\sum_{j \neq i} (\mathbf{M} \cdot \mathbf{c}_j)^2 \right] (\mathbf{M} \cdot \mathbf{c}_i) \mathbf{c}_i. \quad (2.16)$$

2.3.3 Exchange interaction

The origin of ferromagnetism lies in the exchange interaction, which appears by the tendency of the electrons to reduce the Coulomb interaction. Exchange has no classic analog since it is caused by the overlap of neighboring wave functions. Because of Pauli's exclusion principle, the antisymmetric character of the electronic states gives way to a coupling between the spin state and the spatial wave function. Namely, if two electrons have parallel spins (symmetric spin state), they tend to repel each other, a characteristic of antisymmetric spatial wave functions, which reduces the average electrostatic energy. This reduction in energy favors both parallel spin alignment and the surge of a magnetic moment in atoms and ions in their ground states.

In a model of localized magnetism the exchange interaction is often described in terms of the Heisenberg Hamiltonian,

$$\mathcal{H}_{\text{ex}} = - \sum_{ij} J_{ij} \mathbf{S}_i \cdot \mathbf{S}_j, \quad (2.17)$$

where \mathbf{S}_i is a spin localized at the i -th lattice point, and J_{ij} is the exchange integral that gives the intensity of the coupling between spins i and j . Usually, it is considered that $J_{ij} = J$ for near neighbors (nn), and $J_{ij} = 0$ otherwise. J is positive for ferromagnets, which favors parallel alignment, and negative for antiferromagnets, but that is outside the scope of this thesis.

Misaligned spins in a ferromagnet always carry a heavy energy cost due to exchange. Starting from the Heisenberg Hamiltonian and aiming for the continuum limit, we treat operators as vectors and write $\mathbf{S}_i \cdot \mathbf{S}_j = S^2 \cos \phi_{ij}$, where ϕ_{ij} is the angle between the spins. Since the exchange interaction is robust at short range, the nn angles are always small, $|\phi_{ij}| \ll 1$, such that to first order we have

$$E_{\text{ex}} = \frac{JS^2}{2} \sum_{\text{nn}} \phi_{ij}^2, \quad (2.18)$$

where we have omitted a constant term that corresponds to the ground state (all spins point in the same direction). This term plays no role in the calculations performed in this thesis, and hence is omitted, which is equivalent to redefining the energy zero. We note that the previous discussion also holds for the more encompassing concept of magnetic moment $\boldsymbol{\mu}$.

Now, to take the continuum limit, we assume a unitary magnetization distribution \mathbf{m} such that $\mathbf{m}(\mathbf{r}_i) = \boldsymbol{\mu}_i$, where $\boldsymbol{\mu}_i$ is the unitary magnetic moment at site i . Then, we fix the lattice i and write $\mathbf{m}(\mathbf{r}_i + \mathbf{r}_{ij}) = \boldsymbol{\mu}_j$, where \mathbf{r}_{ij} is the relative position of site j respect to site i . For nn lattice sites, we have that $|\phi_{ij}| \ll 1$, thus $|\phi_{ij}| \approx |\mathbf{m}(\mathbf{r}_i) - \mathbf{m}(\mathbf{r}_i + \mathbf{r}_{ij})|$, and hence $|\phi_{ij}| \approx |\mathbf{r}_{ij} \cdot (\nabla \mathbf{m})(\mathbf{r}_i)|$. The exchange energy can then be written as

$$E_{\text{ex}} = \frac{JS^2}{2} \sum_i \sum_{\mathbf{r}_{ij}} |\mathbf{r}_{ij} \cdot (\nabla \mathbf{m})(\mathbf{r}_i)|^2, \quad (2.19)$$

where the first sum runs over the lattice sites, while the second one runs over its nn sites. For crystals with cubic symmetry, the sum over the nn sites results in

$$\sum_{\mathbf{r}_{ij}} |\mathbf{r}_{ij} \cdot (\nabla \mathbf{m})(\mathbf{r}_i)|^2 = 2a^2 c \|\nabla \mathbf{m}(\mathbf{r}_i)\|^2, \quad (2.20)$$

where c is the number of atomic sites in a cubic cell of side a . For a simple cubic lattice $c = 1$, for a bcc $c = 2$, and for a fcc lattice $c = 4$. In this way, when taking the continuum limit of the lattice sum, the exchange energy can be written as

$$E_{\text{ex}} = A_{\text{ex}} \int_{\Omega} \|\nabla \mathbf{m}\|^2. \quad (2.21)$$

Here A_{ex} is the so-called stiffness constant of the ferromagnet and is defined by $A_{\text{ex}} = JS^2c/a$ for materials with crystalline cubic structure. For hexagonal crystals, like cobalt, $A_{\text{ex}} = 4\sqrt{2}JS^2/a$. The exchange length, $\ell_{\text{ex}} = \sqrt{2A_{\text{ex}}/\mu_0 M_s^2}$, is usually taken as a natural scale for length.

Finally, the exchange energy density is given by $u_{\text{ex}}(\nabla \mathbf{m}) = A_{\text{ex}} \|\nabla \mathbf{m}\|^2$. The effective exchange field is given by $\mathbf{H}_{\text{ex}} = \nabla \cdot \partial u_{\text{ex}} / \partial (\nabla \mathbf{M})$. Thus,

$$\mathbf{H}_{\text{ex}} = \mu_0 \ell_{\text{ex}}^2 \nabla^2 \mathbf{M}, \quad (2.22)$$

where we have used that $\mathbf{M} = M_s \mathbf{m}$.

2.3.4 Dipolar interaction

The dipolar or magnetostatic energy has its origin in the classical interaction between magnetic dipoles inside a magnetic material. An excellent book in classical electromagnetism is that of Zangwill [145]. Consider a lattice of localized magnetic dipoles, with $\boldsymbol{\mu}_i$ the magnetic moment of site i , and \mathbf{h}_i the field in site i due to all other dipoles. In the absence of thermal fluctuations, the potential energy of the system is

$$E_{\text{dip}} = -\frac{\mu_0}{2} \sum_i \boldsymbol{\mu}_i \cdot \mathbf{h}_i, \quad (2.23)$$

where the 1/2 factor is introduced to avoid the double counting of interactions.

Now, picture a “physically small” sphere centered at site i of radius R , more significant than the unitary cell but not too large, to ensure a uniform magnetization inside the sphere. Then, when computing the field at site i , we take all the dipoles outside the sphere as a continuum. Thus, the field \mathbf{h}_i can be evaluated by taking the field \mathbf{H}_{dip} of a continuum material, subtracting the field due to the continuum material inside the sphere ($-\mathbf{M}/3$), and adding the field \mathbf{h}'_i due to the discrete dipoles inside the sphere. Namely, $\mathbf{h}_i = \mathbf{H}_{\text{dip}} + \frac{1}{3}\mathbf{M} + \mathbf{h}'_i$, where

$$\mathbf{h}'_i = \frac{1}{4\pi} \sum_{r_{ij} < R} \left(-\frac{\boldsymbol{\mu}_j}{r_{ij}^3} + \frac{3(\boldsymbol{\mu}_j \cdot \mathbf{r}_{ij})\mathbf{r}_{ij}}{r_{ij}^5} \right). \quad (2.24)$$

Inside the sphere i the dipoles are constant ($\boldsymbol{\mu}_j = \boldsymbol{\mu}_i$), so that

$$\mathbf{h}'_i = \frac{\boldsymbol{\mu}_i}{4\pi} \sum_{r_{ij} < R} \left(\frac{3\mathbf{r}_{ij} \otimes \mathbf{r}_{ij} - r_{ij}^2 \mathbf{I}}{r_{ij}^5} \right). \quad (2.25)$$

Here, the symbol \otimes stands for tensor multiplication. For example, $\hat{\mathbf{x}} \cdot (\mathbf{r} \otimes \mathbf{r}) = xr$. Assuming that the magnetization distribution \mathbf{M} can be approximated by a constant inside the sphere, we can see that $\mathbf{h}'_i = \boldsymbol{\Lambda} \cdot \mathbf{M}$, where $\boldsymbol{\Lambda}$ is a tensor that only depends on the crystal symmetry, which is null for cubic symmetries. Indeed, if the crystal has cubic symmetry, the sum over the mixed components (e.g., $x_{ij}y_{ij}$) cancels out since, for any term in the sum, there is an equal and opposite contribution. This holds for almost any other symmetry. Furthermore, in a cubic symmetry, the cartesian coordinates x, y, z are interchangeable, so that $3 \sum x_{ij}^2/r_{ij}^5 = \sum 1/r_{ij}^3$, similarly for other components, and hence the above sum is equal to zero. For other kinds of symmetries, the sum is not zero. Finally, substituting these expressions into the dipolar energy and replacing the sum by an integral (continuum limit), we get that the magnetostatic energy can be written as

$$E_{\text{dip}} = -\frac{\mu_0}{2} \int_{\Omega} \mathbf{M} \cdot \left(\mathbf{H}_{\text{dip}} + \frac{1}{3}\mathbf{M} + \boldsymbol{\Lambda} \cdot \mathbf{M} \right). \quad (2.26)$$

The second term is proportional to the saturation magnetization squared, M_s^2 , which is a function of temperature but not of space. Thus, it can be omitted, implying only a zero magnetostatic energy redefinition. The last term, $\mathbf{M} \cdot \boldsymbol{\Lambda} \cdot \mathbf{M}$, has the form and behavior of an anisotropy ($\boldsymbol{\Lambda}$ is not a function of space, only of the crystal

structure), thus it is absorbed in the anisotropy energy and is not considered as part of the dipolar term. In this way, the magnetostatic energy is reduced to

$$E_{\text{dip}} = -\frac{\mu_0}{2} \int_{\Omega} \mathbf{M} \cdot \mathbf{H}_{\text{dip}}, \quad (2.27)$$

where

$$\mathbf{H}_{\text{dip}}(\mathbf{r}, t) = -\frac{\nabla}{4\pi} \int_{\Omega} \mathbf{M}(\mathbf{r}', t) \cdot \nabla' \left(\frac{1}{|\mathbf{r} - \mathbf{r}'|} \right) \quad (2.28)$$

$$= \frac{\nabla}{4\pi} \left(\int_{\Omega} \frac{\nabla' \cdot \mathbf{M}(\mathbf{r}', t)}{|\mathbf{r} - \mathbf{r}'|} - \oint_{\partial\Omega} \frac{\hat{\mathbf{n}}' \cdot \mathbf{M}(\mathbf{r}', t)}{|\mathbf{r} - \mathbf{r}'|} \right) \quad (2.29)$$

Dynamic Matrix Method

In low-dimensional magnetic structures, that is, systems with at least one of the sides comparable with the typical exchange length ℓ_{ex} of the material, simple functional assumptions about the magnetization can accurately describe the dynamical state of the system. Concretely, regarding the mathematical modeling, the far edges of the sample are assumed to be at infinity, while the spatial dependence of the magnetization between the close boundaries is assumed to be constant. As way of illustration, imagine a spin near the center of a thin ferromagnetic layer. The spins at the far edges are too weakly coupled to exert a significant influence; thus, they are ignored. On the other hand, meaningful variations of the magnetization along the film's thickness (on the scale of ℓ_{ex}) come at a heavy energy cost; hence it is reasonable to expect the low energy modes to be uniform along this direction.

However, what happens with an extended 3D magnetic structure? No simple assumptions can be made a priori, as it is no longer possible to ignore the modulation of the magnetization along the bounded directions. Solving the related system of partial differential equations with their boundary conditions is usually not feasible using simple analytical expressions.

One possible way forward is to leave the continuous nature of the problem on the wayside and consider a related discrete problem instead. We start from a semi-analytical theory called the Dynamic Matrix Method (DMM) [144]. This method dictates slicing an extended magnetic structure Ω into N (low-dimensional) micro-magnetic cells $\Omega^1, \dots, \Omega^N$ that are coupled by exchange and dipolar interactions. Assuming we know how to solve the low-dimensional systems and how to describe their interactions, the discrete problem reduces to a finite-dimensional eigenvalue problem. Of course, the continuum problem is expected to correspond to the limit behavior of the discrete problem as $N \rightarrow \infty$, though convergence is usually reached rather quickly.

This chapter is organized as follows. Section 3.1 provides a detailed description of DMM, as applied to different classes of extended magnetic structures; later, we use the Plane Wave Method to generalize DMM for the treatment of periodic systems (magnonic crystals). In Section 3.2 we derive the required analytical expressions for the Zeeman, anisotropy, exchange, and dipolar interactions.

3.1 Eigenvalue Problem

The study of magnetization dynamics in the framework of classical mechanics leads naturally to a system of partial differential equations. By making use of two different kinds of approximations,

1. first-order perturbation theory; and
2. discretization into micromagnetic cells;

we can (1) linearize our system of differential equations and give it the algebraic structure of an eigenvalue problem; and (2) reduce the dimension of the resulting vector space from uncountable to countable, and then, finite. We require of an extended magnetic system $\Omega \subset \mathbf{R}^3$ that:

1. If Ω is unbounded in some direction, then it is invariant under continuous or discrete translations along that direction;
2. Ω can be partitioned into a finite number N of cells $\Omega^1, \dots, \Omega^N$ whose geometry exhibits continuous translation symmetry.

Since we have a finite number N of cells, we can label them by assigning each one an integer $\mu \in \{1, \dots, N\}$. Thus, the magnetization of the μ -th body is denoted by $\mathbf{M}^\mu : \mathbf{R}^3 \rightarrow \mathbf{C}^3$. As part of the discretization into micromagnetic cells, we take the equilibrium configuration and magnetic parameters of each cell to be uniform or periodic. In general, the equilibrium configuration is not the same for every cell, so we introduce a right-handed orthonormal basis $\mathbf{e}_1^\mu, \mathbf{e}_2^\mu, \mathbf{e}_3^\mu$ such that \mathbf{e}_3^μ points in the direction of the equilibrium configuration of \mathbf{M}^μ . By convention, unless otherwise

stated, the spatial components of vectors and tensors are taken with respect to the local basis of each layer. That is, $A_j^\mu = \mathbf{e}_j^\mu \cdot \mathbf{A}^\mu$ and $B_{ij}^{\mu\nu} = \mathbf{e}_i^\mu \cdot \mathbf{B}^{\mu\nu} \cdot \mathbf{e}_j^\nu$.

Different kinds of interactions are accounted through the effective magnetic fields $\mathbf{H}^\mu : \mathbf{R}^3 \rightarrow \mathbf{C}^3$ that are relevant for describing the magnetization's temporal evolution. The dynamics of the μ -th cell is modeled by the Landau-Lifshitz equation

$$\frac{d}{dt}\mathbf{M}^\mu(\mathbf{r}, t) = -\gamma\mu_0\mathbf{M}^\mu(\mathbf{r}, t) \times \mathbf{H}^\mu(\mathbf{r}, t), \quad (3.1)$$

where γ is the absolute value of the gyromagnetic ratio. To linearize the equations of motion, both the magnetization and the effective fields are written in terms of static (zeroth order) and dynamic (first-order) magnetization components; higher-order terms are neglected. We also assume that the dynamic magnetization components behave like monochromatic plane waves, with the wave vector \mathbf{k} confined to the symmetry axes (extended directions). Thus,

$$\mathbf{M}^\mu(\mathbf{r}, t) = \mathbf{M}_{\text{eq}}^\mu + \mathbf{m}^\mu e^{i(\mathbf{k}\cdot\mathbf{r}-\omega t)} \quad (3.2)$$

and

$$\mathbf{H}^\mu(\mathbf{r}, t) = \mathbf{H}_{\text{eq}}^\mu + \mathbf{h}^\mu e^{i(\mathbf{k}\cdot\mathbf{r}-\omega t)}, \quad (3.3)$$

where $\mathbf{m}^\mu, \mathbf{h}^\mu \in \mathbf{C}^3$ are perpendicular to the equilibrium direction ($\mathbf{H}_{\text{eq}}^\mu \parallel \mathbf{M}_{\text{eq}}^\mu$), and M_{eq}^μ is equal to the saturation magnetization M_s^μ . By keeping terms up to first order in \mathbf{m}^μ and \mathbf{h}^μ , we obtain the following system of linear equations,

$$\omega\mathbf{m}^\mu = i\gamma\mu_0(\mathbf{H}_{\text{eq}}^\mu \times \mathbf{m}^\mu + \mathbf{h}^\mu \times \mathbf{M}_{\text{eq}}^\mu), \quad (3.4)$$

for $1 \leq \mu \leq N$.

3.1.1 Continuous Symmetry

Here we assume the magnetic parameters are uniform along the extended directions; that is, all translation symmetries are continuous. By means of dynamic multi-element tensors $\Lambda^{\mu\nu}$ a convenient linear structure is assumed for the dynamic components of the effective field, namely $\mathbf{h}^\mu = -\sum_p \Lambda^{\mu p} \cdot \mathbf{M}^p$. With this in mind,

the above system of linear equations [see Eq. (3.4)] becomes homogeneous and can be interpreted as an eigenvalue problem of the form $\mathbf{T}\mathbf{m} = \omega\mathbf{m}$, where $\mathbf{T} \in \mathcal{L}(\mathbf{C}^{2N})$ is a linear operator acting on the vector \mathbf{m} , where $\mathbf{m}^T = (m_1^1, \dots, m_1^N, m_2^1, \dots, m_2^N)$. Concerning the canonical basis of \mathbf{C}^{2N} , the matrix representation of \mathbf{T} is given by

$$T_{ql} = i\gamma\mu_0 \times \begin{cases} -M_s^\mu \Lambda_{21}^{\mu\nu}, & 1 \leq q, l \leq N \\ -M_s^\mu \Lambda_{22}^{\mu\nu} - H_{\text{eq}}^\mu \delta_{\mu\nu}, & 1 \leq q \leq N < l \leq 2N \\ M_s^\mu \Lambda_{11}^{\mu\nu} + H_{\text{eq}}^\mu \delta_{\mu\nu}, & 1 \leq l \leq N < q \leq 2N \\ M_s^\mu \Lambda_{12}^{\mu\nu}, & N < q, l \leq 2N \end{cases} \quad (3.5)$$

where $\mu = q \pmod{N}$ and $\nu = l \pmod{N}$.¹ Equivalently

$$T_{ql} = i\gamma\mu_0 \left((-1)^{j-1} H_{\text{eq}}^\mu \delta_{\mu\nu} \delta_{ij} + (-1)^{i-1} M_s^\mu \Lambda_{ij}^{\mu\nu} \right), \quad (3.6)$$

where $1 \leq i, j \leq 2$ and $1 \leq \mu, \nu \leq N$ are integers uniquely defined by $q = (2-i)N + \mu$ and $l = (j-1)N + \nu$, for each $1 \leq q, l \leq 2N$. Here δ_{ij} stands for the Kronecker delta symbol.

3.1.2 Discrete Symmetry

Now we study the spin wave propagation along (one-dimensional) periodic systems (magnonic crystals), where a generalization of the previous discussion is needed. We adapt the first-order perturbation by explicitly writing out the Fourier expansions of $\mathbf{M}_{\text{eq}}^\mu$, \mathbf{m}^μ , $\mathbf{H}_{\text{eq}}^\mu$, and \mathbf{h}^μ ; a common approach known in the literature as the Plane Wave Method. It follows that

$$\mathbf{M}^\mu(\mathbf{r}, t) = \sum_{n \in \mathbf{Z}} \tilde{\mathbf{M}}_{\text{eq}}^\mu(n) e^{i\mathbf{G}_n \cdot \mathbf{r}} + \sum_{n \in \mathbf{Z}} \tilde{\mathbf{m}}^\mu(n) e^{i((\mathbf{k} + \mathbf{G}_n) \cdot \mathbf{r} - \omega t)}. \quad (3.7)$$

¹Here $(\text{mod } N)$ signals that we are working in modular arithmetic under the identification $\mu + N \equiv \mu$, in other words, $\mu = q \pmod{N}$ if and only if $\mu - q$ is an integer multiple of N

Here $\mathbf{G}_n = (2\pi/a)\hat{\mathbf{x}}$ is the reciprocal lattice vector, where we have assumed the periodicity to be along the x -axis. A similar structure is given for \mathbf{H}^μ . A slight generalization of the dynamic multi-element tensor approach yields

$$\tilde{\mathbf{h}}^\mu(n) = - \sum_{\nu=1}^N \sum_{p \in \mathbf{Z}} \Gamma^{\mu\nu}(n, p) \cdot \tilde{\mathbf{m}}^\nu(p). \quad (3.8)$$

Hence, concerning the magnetization's Fourier coefficients, we obtain the following homogeneous system of linear equations

$$\omega \tilde{\mathbf{m}}^\mu(n) = i\gamma\mu_0 \sum_{p \in \mathbf{Z}} \left(\tilde{\mathbf{H}}_{\text{eq}}^\mu(n-p) \times \tilde{\mathbf{m}}^\mu(p) + \tilde{\mathbf{M}}_{\text{eq}}^\mu(n-p) \times \sum_{\nu=1}^N \sum_{q \in \mathbf{Z}} \Gamma^{\mu\nu}(p, q) \cdot \tilde{\mathbf{m}}^\nu(q) \right), \quad (3.9)$$

for $1 \leq \mu \leq N$ and $n \in \mathbf{Z}$. In order to obtain a finite-dimensional eigenvalue problem (because computational resources are finite), we need to consider only a finite-dimensional subspace of reciprocal space. Thus, we discard higher order Fourier coefficients after a certain threshold c , for c a nonnegative integer. Taking this truncation into account, the above linear system can be read as an eigenvalue problem of the form $\mathbf{T}\mathbf{m} = \omega\mathbf{m}$, where $\mathbf{T} \in \mathcal{L}(\mathbf{C}^{2N(2c+1)})$ is a linear operator acting on the dynamic magnetization vector \mathbf{m} , where

$$\mathbf{m}^{\mathbf{T}} = \left(\tilde{m}_1^1(-c), \dots, \tilde{m}_1^1(c), \dots, \tilde{m}_1^N(-c), \dots, \tilde{m}_1^N(c), \right. \\ \left. \tilde{m}_2^1(-c), \dots, \tilde{m}_2^1(c), \dots, \tilde{m}_2^N(-c), \dots, \tilde{m}_2^N(c) \right). \quad (3.10)$$

A generalization of Eq. (3.6) leads to

$$T_{ql} = i\gamma\mu_0 \left((-1)^{j-1} H_{\text{eq}}^\mu(n-p) \delta_{\mu\nu} \delta_{ij} + (-1)^{i-1} \sum_u M_s^\mu(n-u) \Gamma_{ij}^{\mu\nu}(u, p) \right), \quad (3.11)$$

where $1 \leq i, j \leq 2$, $1 \leq \mu, \nu \leq N$, and $-c \leq n, p \leq c$ are integers uniquely defined by $q = (2c+1)((2-i)N + \mu) + (n+c+1)$ and $l = (2c+1)((j-1)N + \nu) + (p+c+1)$, for each $1 \leq q, l \leq 2N(2c+1)$.

3.2 Effective Fields

Various kinds of interactions play a role in how spins are coupled with each other and their ambient. For this thesis, we consider Zeeman, anisotropy, exchange, and dipolar interactions. In the context of the DMM, the different ways that micromagnetic cells can be coupled are collected in effective fields. That is, $\mathbf{H}^\mu = \mathbf{H}_Z + \mathbf{H}_{\text{an}}^\mu + \mathbf{H}_{\text{ex}}^\mu + \mathbf{H}_{\text{dip}}^\mu$. Furthermore, the equilibrium condition requires that $\mathbf{H}_{\text{eq}}^\mu = (\mathbf{e}_3^\mu \otimes \mathbf{e}_3^\mu) \cdot (\mathbf{H}_Z + \mathbf{H}_{\text{eq-an}}^\mu + \mathbf{H}_{\text{eq-ex}}^\mu + \mathbf{H}_{\text{eq-dip}}^\mu)$, while the dynamic multi-element tensor can be decomposed as $\Lambda^{\mu\nu} = \Lambda_{\text{an}}^{\mu\nu} + \Lambda_{\text{ex}}^{\mu\nu} + \Lambda_{\text{dip}}^{\mu\nu}$. Here, the Zeeman interaction is accounted for by a static external field \mathbf{H}_Z . As for anisotropy, we note that the field expressions given in chapter 2 already have an adequate form. We perform a first order perturbation in Eq. (2.16) and obtain that $\mathbf{h}_a = -\Lambda_a \cdot \mathbf{m}$, where

$$\Lambda_a = -\frac{2K_u}{\mu_0^2 M_s^2} \mathbf{a} \otimes \mathbf{a} + \frac{2K_c}{\mu_0^2 M_s^4} \sum_{i=1}^3 \sum_{j \neq i} \left[(\mathbf{M}_{\text{eq}} \cdot \mathbf{c}_j)^2 \mathbf{c}_i \otimes \mathbf{c}_i + 2(\mathbf{M}_{\text{eq}} \cdot \mathbf{c}_j)(\mathbf{M}_{\text{eq}} \cdot \mathbf{c}_i) \mathbf{c}_j \otimes \mathbf{c}_i \right] \quad (3.12)$$

To take into account the interaction between different cells, we write $\Lambda_a^{\mu\nu} = \delta_{\mu\nu} \Lambda_a$. Exchange and dipolar interactions require further treatment, which is given in the forthcoming subsections.

Before getting ahead of ourselves, it proves convenient to introduce the following notation. Henceforth, when writing down integral expressions, we omit the differential elements to visualize the formulas easily. Regarding the geometry of the micromagnetic cells, we denote by \int_μ the operator that integrates a function over the μ -th cell cross-section. For example, if we deal with ferromagnetic stripes, $\int_\mu \eta$ corresponds to the integral of a function η over an interval determined by a rectangle cross-section.

3.2.1 Exchange Interaction

Exchange interaction is considered by employing two terms. One of them is associated with the exchange interaction within each cell. This inner exchange field of the

μ -th cell is equal to $\ell_{\text{ex}}^2 \nabla^2 \mathbf{M}^\mu$. However, since overall this expression is not constant along the cell's cross section, the effective exchange field is defined as the cross section average, that is, $\mathbf{H}_{\text{ex1}}^\mu = (\int_\mu \ell_{\text{ex}}^2 \nabla^2 \mathbf{M}^\mu) / (\int_\mu)$. The other term is related to the exchange interaction between neighboring cells. In this case, the exchange energy density between two neighbor cells is $\epsilon_{\text{ex2}}^{\mu\nu} = -J^{\mu\nu} / (M_s^\mu M_s^\nu) \mathbf{M}^\mu \cdot \mathbf{M}^\nu$, where $J^{\mu\nu}$ is a coupling parameter. Note that $\mu_0 \mathbf{H}_{\text{ex2}}^\mu = -\sum_\nu (\delta \epsilon^{\mu\nu} / \delta \mathbf{M}^\mu) / b$, where b stands for the length of the cross-section traverse to the contact interface. Taking into account both contributions, i.e., adding them together, it follows that

$$\Lambda_{\text{ex}}^{\mu\nu} = \ell_{\text{ex}}^2 k^2 \delta_{\mu\nu} - \frac{J}{\mu_0 M_s^\mu M_s^\nu b} (\delta_{\mu,\nu+1} + \delta_{\mu,\nu-1}), \quad (3.13)$$

and

$$\mathbf{H}_{\text{eq-ex}}^\mu = \frac{J}{\mu_0 M_s^\mu b} \sum_\nu (\delta_{\mu,\nu+1} + \delta_{\mu,\nu-1}) \mathbf{e}_3^\nu. \quad (3.14)$$

If the system is divided into many cells, the continuous approach allows establishing that $J = 2A_{\text{ex}}/b$ [4], where A_{ex} is the exchange constant of the magnetic material defined in the continuous limit.

3.2.2 Dipolar Interaction

The magnetic field $\mathbf{H}_{\text{dip}}^{(\nu)}$ generated by the micromagnetic cell Ω^ν is given by

$$\mathbf{H}_{\text{dip}}^{(\nu)}(\mathbf{r}, t) = -\frac{\nabla}{4\pi} \int_{\Omega^\nu} \mathbf{M}^\nu(\mathbf{r}', t) \cdot \nabla' \left(\frac{1}{|\mathbf{r} - \mathbf{r}'|} \right), \quad (3.15)$$

$$= \frac{\nabla}{4\pi} \left(\int_{\Omega^\nu} \frac{\nabla' \cdot \mathbf{M}^\nu(\mathbf{r}', t)}{|\mathbf{r} - \mathbf{r}'|} - \oint_{\partial\Omega^\nu} \frac{\hat{\mathbf{n}}' \cdot \mathbf{M}^\nu(\mathbf{r}', t)}{|\mathbf{r} - \mathbf{r}'|} \right). \quad (3.16)$$

If there is no periodicity, we can say that $\mathbf{H}_{\text{dip}}^{(\nu)}(\mathbf{r}, t) = \mathbf{H}_{\text{eq-dip}}^{(\nu)}(\mathbf{r}) + \mathbf{h}_{\text{dip}}^{(\nu)}(\mathbf{r}) e^{i(\mathbf{k} \cdot \mathbf{r} - \omega t)}$, where the spatial dependence of $\mathbf{H}_{\text{eq-dip}}^{(\nu)}$ and $\mathbf{h}_{\text{dip}}^{(\nu)}$ is restricted to the bounded directions. This spatial dependence is a consequence of the translation-invariant symmetry along the extended directions. However, we note that these functional forms do not fit well with DMM, which forces us to consider their cross-section

averages. Thus, we define the dynamic demagnetizing tensor $\Lambda_{\text{dip}}^{\mu\nu}$ in relation to the μ -th cross section average of the magnetic field $\mathbf{h}_{\text{dip}}^{(\nu)}$. Namely, we set

$$\frac{1}{\left(\int_{\mu}\right)} \int_{\mu} \mathbf{h}_{\text{dip}}^{(\nu)}(\mathbf{r}) = -\Lambda_{\text{dip}}^{\mu\nu} \cdot \mathbf{m}^{\nu}. \quad (3.17)$$

As for the effective equilibrium field $\mathbf{H}_{\text{dip}}^{\mu}$, it is worth noting that in the null wave-vector limit, we have

$$\frac{1}{\left(\int_{\mu}\right)} \int_{\mu} \mathbf{H}_{\text{eq-dip}}^{(\nu)}(\mathbf{r}) = -\lim_{\mathbf{k} \rightarrow 0} \Lambda_{\text{dip}}^{\mu\nu} \cdot \mathbf{M}_{\text{eq}}^{\nu}, \quad (3.18)$$

so that we have

$$\mathbf{H}_{\text{eq-dip}}^{\mu} = \frac{1}{\left(\int_{\mu}\right)} \sum_{\nu} \int_{\mu} \mathbf{H}_{\text{eq-dip}}^{(\nu)}(\mathbf{r}, t), \quad (3.19)$$

$$= -\lim_{\mathbf{k} \rightarrow 0} \sum_{\nu} \Lambda_{\text{dip}}^{\mu\nu} \cdot \mathbf{M}_{\text{eq}}^{\nu}. \quad (3.20)$$

In other words, the null wave-vector limit of the dynamic demagnetizing tensor is precisely the static demagnetizing tensor. Hence, we only focus on the dynamic case.

Nevertheless, what happens in the presence of periodicity? The previous discussion can be easily adapted for the Fourier coefficients of the effective field. A look at Eq. (3.7) tells us to make the substitution $\mathbf{k} \mapsto \mathbf{k} + \mathbf{G}_n$ for the dynamic component, and to describe the equilibrium component as if it were dynamic under the identification $\mathbf{k} = \mathbf{G}_n$. It follows that

$$\Gamma_{\text{dip}}^{\mu\nu}(n, p) = \delta_{np} \Lambda_{\text{dip}}^{\mu\nu} \Big|_{\mathbf{k} \mapsto \mathbf{k} + \mathbf{G}_n}, \quad (3.21)$$

and

$$\tilde{\mathbf{H}}_{\text{eq-dip}}^{\mu}(n) = -\lim_{\mathbf{k} \rightarrow 0} \sum_{\nu} \Gamma_{\text{dip}}^{\mu\nu}(n, n) \cdot \tilde{\mathbf{M}}_{\text{eq}}^{\nu}(n). \quad (3.22)$$

Hence, once we have the solutions for the uniform problem, we obtain the solutions for its periodic counterpart for free.

In the following, we find explicit expressions for the dynamic demagnetizing tensors. Two systems are under consideration, namely coupled uniform layers and coupled uniform stripes.

Layers Consider that our magnetic system Ω is such that it can be partitioned into N uniform thin layers $\Omega^1, \dots, \Omega^N$. By considering equation (3.16), we have that $\nabla \cdot \mathbf{M}^\nu(\mathbf{r}, t) = i\mathbf{k} \cdot \mathbf{m}^\nu e^{i(\mathbf{k} \cdot \mathbf{r} - \omega t)}$ and $\hat{\mathbf{n}} \cdot \mathbf{M}^\nu(\mathbf{r}, t) = \text{sgn}[y - (y^\nu + d/2)][(M_{\text{eq}}^\nu)_y + m_y^\nu e^{i(\mathbf{k} \cdot \mathbf{r} - \omega t)}]$. Then, it follows that

$$\mathbf{h}_{\text{dip}}^{(\nu)}(y) = \frac{\nabla}{4\pi} \left(\int_{\nu} \int_{\mathbf{R}^2} \frac{i\mathbf{k} e^{i\mathbf{k} \cdot \mathbf{r}'}}{|\mathbf{r} - \mathbf{r}'|} - \int_{\mathbf{R}^2} \frac{\hat{\mathbf{y}} e^{i\mathbf{k} \cdot \mathbf{r}'}}{|\mathbf{r} - \mathbf{r}'|} \Big|_{y'=y^\nu}^{y^\nu+d} \right) \cdot \mathbf{m}^\nu e^{-i\mathbf{k} \cdot \mathbf{r}}, \quad (3.23)$$

$$= \frac{i\mathbf{k} + \nabla}{2k} \left(i\mathbf{k} \int_{\nu} e^{-k|y-y'|} - \hat{\mathbf{y}} e^{-k|y-y'|} \Big|_{y'=y^\nu}^{y^\nu+d} \right) \cdot \mathbf{m}^\nu, \quad (3.24)$$

where we have used $\iint_{-\infty}^{\infty} dx dz e^{i(ax+bz)}/\sqrt{x^2+y^2+z^2} = 2\pi e^{-|y|\sqrt{a^2+b^2}}/\sqrt{a^2+b^2}$. Hence, solving equation (3.17) we arrive to

$$\Lambda_{\text{dip}}^{\mu\nu} = (1 - \cosh kd) \frac{e^{-k|y^\mu - y^\nu|}}{kd} \left(\hat{\mathbf{y}} \otimes \hat{\mathbf{y}} - i \text{sgn}(\mu - \nu) \frac{\hat{\mathbf{y}} \otimes \mathbf{k} + \mathbf{k} \otimes \hat{\mathbf{y}}}{k} - \frac{\mathbf{k} \otimes \mathbf{k}}{k^2} \right), \quad (3.25)$$

for $\mu \neq \nu$, and

$$\Lambda_{\text{dip}}^{\mu\mu} = \frac{1 - e^{-kd}}{kd} \left(\hat{\mathbf{y}} \otimes \hat{\mathbf{y}} - \frac{\mathbf{k} \otimes \mathbf{k}}{k^2} \right) + \frac{\mathbf{k} \otimes \mathbf{k}}{k^2}, \quad (3.26)$$

for $\mu = \nu$. To solve Eq. (3.26) it is crucial to take into account the singularity in (3.24) at $y = y'$ and write $\int_{\mu} \int_{\nu} \eta(y - y') = \lim_{\epsilon \rightarrow 0^+} \int_0^d (\int_0^{y-\epsilon} + \int_{y+\epsilon}^d) dy' dy \eta(y - y')$.

Stripes Now, consider that Ω can be partitioned into N thin stripes $\Omega^1, \dots, \Omega^N$. We will consider expressions of the form $\int_{\mu} \int_{\nu} \eta(\boldsymbol{\rho} - \boldsymbol{\rho}')$, where the ν -integral is over the primed coordinates, the μ -integral is over the non-primed coordinates, and η is a well-behaved function with a singularity at the origin. Thus

$$\int_{\mu} \int_{\nu} \eta(\boldsymbol{\rho} - \boldsymbol{\rho}') = \int_{\delta x^{\mu\nu}}^{\delta x^{\mu\nu}+b} \int_{\delta y^{\mu\nu}}^{\delta y^{\mu\nu}+d} \int_0^b \int_0^d dy' dx' dy dx \eta(\boldsymbol{\rho} - \boldsymbol{\rho}'), \quad (3.27)$$

for $\mu \neq \nu$, and

$$\int_{\mu} \int_{\nu} \eta(\boldsymbol{\rho} - \boldsymbol{\rho}') = \lim_{\epsilon, \delta \rightarrow 0^+} \int_{\delta}^{b-\delta} \int_{\delta}^{b+\delta} \int_{-\delta}^{b+\delta} \left(\int_{-\delta}^{y-\epsilon} + \int_{y+\epsilon}^{d+\delta} \right) dy' dx' dy dx \eta(\boldsymbol{\rho} - \boldsymbol{\rho}'), \quad (3.28)$$

for $\mu = \nu$, where $(\delta x^{\mu\nu}, \delta y^{\mu\nu})$ represents the relative position of the μ -th stripe respect to the ν -th stripe. It is interesting to consider the effect of changing the order of derivation and integration. If $\mu \neq \nu$, the operators commute. However, if $\mu = \nu$, it follows from the above equation that

$$\int_{\mu} \left(\nabla \int_{\mu} - \int_{\mu} \nabla \right) \eta(\boldsymbol{\rho} - \boldsymbol{\rho}') = d\hat{\mathbf{y}} \lim_{\epsilon, \delta \rightarrow 0^+} \int_{\delta}^{b-\delta} \int_{-\delta}^{d+\delta} dx' dx \eta(\boldsymbol{\rho} - \boldsymbol{\rho}') \Bigg|_{y'=y+\epsilon}^{y-\epsilon}. \quad (3.29)$$

Now, to compute the equilibrium field and demagnetizing tensor, we start from Eq. (3.15), thus

$$\begin{aligned} \mathbf{h}_{\text{dip}}^{(\nu)} &= -\frac{\nabla}{4\pi} \left(\int_{\nu} \int_{\mathbf{R}^2} e^{i\mathbf{k}\cdot\mathbf{r}'} \nabla' \left(\frac{1}{|\mathbf{r} - \mathbf{r}'|} \right) \right) \cdot \mathbf{m}^{\nu} e^{-i\mathbf{k}\cdot\mathbf{r}}, \\ &= \frac{i\mathbf{k} + \nabla}{2\pi} \left(\int_{\nu} (i\mathbf{k} + \nabla) K_0(k|\boldsymbol{\rho} - \boldsymbol{\rho}'|) \right) \cdot \mathbf{m}^{\nu}. \end{aligned} \quad (3.30)$$

Eq. (3.30) follows by noting that $\nabla|\mathbf{r} - \mathbf{r}'| = -\nabla'|\mathbf{r} - \mathbf{r}'|$, commuting the operators $\int_{\mathbf{R}} \nabla = \nabla \int_{\mathbf{R}}$, using the identity $\int_{-\infty}^{\infty} dz e^{iaz} / \sqrt{z^2 + b^2} = 2K_0(|ab|)$ for $a, b \in \mathbf{R}$, invoking the product rule $\nabla e^{i\mathbf{k}\cdot\mathbf{r}} \eta(\boldsymbol{\rho}) = e^{i\mathbf{k}\cdot\mathbf{r}} (i\mathbf{k} + \nabla) \eta(\boldsymbol{\rho})$ in succession, and canceling out the exponentials. Then, by using Eq. (3.17),

$$\Lambda_{\text{dip}}^{\mu\nu} = \int_{\mu} \int_{\nu} \mathbf{K}(\boldsymbol{\rho} - \boldsymbol{\rho}') + \delta_{\mu\nu} \hat{\mathbf{y}} \otimes \hat{\mathbf{y}}. \quad (3.31)$$

Here the innermost ν -integral is over the primed coordinates, the outermost μ -integral is over the non-primed coordinates, and the tensor field \mathbf{K} is defined by

$$\begin{aligned} \mathbf{K}(\boldsymbol{\rho}) &= \frac{1}{2\pi bd} \left(K_0(k\rho) \mathbf{k} \otimes \mathbf{k} + i \frac{K_1(k\rho)}{\rho/k} (\mathbf{k} \otimes \boldsymbol{\rho} + \boldsymbol{\rho} \otimes \mathbf{k}) \right. \\ &\quad \left. + \frac{K_1(k\rho)}{\rho/k} (\hat{\mathbf{x}} \otimes \hat{\mathbf{x}} + \hat{\mathbf{y}} \otimes \hat{\mathbf{y}}) - \frac{K_2(k\rho)}{\rho^2/k^2} \boldsymbol{\rho} \otimes \boldsymbol{\rho} \right), \end{aligned} \quad (3.32)$$

with K_l denoting the l -th Bessel function of the second kind. Equation (3.31) is obtained by considering the derivatives $K'_0 = -K_1$ and $K''_0 = (K_0 + K_2)/2$, the identity $2K_1(x) = x(K_2 - K_0)(x)$, and using the commutation property shown in Eq. (3.29), wherein the resulting integrals are evaluated by taking $K_1(x) = 1/x + \mathcal{O}(x)$. Note that \mathbf{K} is symmetric and traceless, so that the demagnetizing tensor $\Lambda_{\text{dip}}^{\mu\nu}$ is symmetric, with trace 1 if $\mu = \nu$ and trace 0 otherwise, as expected [Henry16, Newell93]. Also, $K_{xz}(x, y) = K_{yz}(y, x)$. Thus, in solving $\int_\mu \int_\nu \mathbf{K}(\boldsymbol{\rho} - \boldsymbol{\rho}')$, only four components need be considered: K_{xx} , K_{xy} , K_{xz} and K_{zz} . Here, the spatial components are taken concerning the $\hat{\mathbf{x}}, \hat{\mathbf{y}}, \hat{\mathbf{z}}$ basis.

Assuming there exists a tensor field \mathbf{J} such that $\mathbf{K} = \partial_{xx}\partial_{yy}\mathbf{J}$, it follows from equations (3.27) and (3.28) that

$$\Lambda_{\text{dip}}^{\mu\nu} = \sum_{s,t=-1}^1 (2 - 3|s|)(2 - 3|t|)\mathbf{J}(\delta x^{\mu\nu} + sb, \delta y^{\mu\nu} + td), \quad (3.33)$$

for $\mu \neq \nu$, and

$$\Lambda_{\text{dip}}^{\mu\mu} = \hat{\mathbf{y}} \otimes \hat{\mathbf{y}} + \lim_{\delta \rightarrow 0^+} \left(\mathbf{J}(\boldsymbol{\rho} - \boldsymbol{\rho}') \Big|_{y'=-\delta}^{d+\delta} \Big|_{y=\delta}^{d-\delta} + d \lim_{\epsilon \rightarrow 0^+} \frac{\partial \mathbf{J}}{\partial y}(\boldsymbol{\rho} - \boldsymbol{\rho}') \Big|_{y'=y+\epsilon}^{y-\epsilon} \right) \Big|_{x'=-\delta}^{b+\delta} \Big|_{x=\delta}^{b-\delta}, \quad (3.34)$$

for $\mu = \nu$.

However, no elementary representation of \mathbf{J} exists because Bessel functions do not have enough antiderivatives. On the other hand, it is possible to seek a solution in their series expansions. Known series expansions of K_0 , K_1 and K_2 , around $z = 0$, are

$$K_0(z) = -\alpha_E - \ln\left(\frac{z}{2}\right) + \mathcal{O}(z)^2, \quad (3.35)$$

$$K_1(z) = \frac{1}{z} + \left(-\frac{1}{2} + \alpha_E + \ln\left(\frac{z}{2}\right)\right) \frac{z}{2} + \mathcal{O}(z)^2, \quad (3.36)$$

$$K_2(z) = \frac{2}{z^2} - \frac{1}{2} + \mathcal{O}(z)^2, \quad (3.37)$$

where α_E stands for the Euler-Mascheroni constant (≈ 0.577). Hence, to first order, \mathbf{K} is determined by

$$K_{xx}(x, y) = \frac{1}{2\pi bd} \left[\frac{y^2 - x^2}{(x^2 + y^2)^2} + \frac{k^2 x^2 - y^2}{4 x^2 + y^2} \right] - \frac{K_{zz}(x, y)}{2}, \quad (3.38)$$

$$K_{xy}(x, y) = \frac{1}{2\pi bd} \left(\frac{k^2 xy}{2 x^2 + y^2} - \frac{2xy}{(x^2 + y^2)^2} \right), \quad (3.39)$$

$$K_{xz}(x, y) = \frac{ik_z}{2\pi bd} \left(\frac{x}{x^2 + y^2} - \frac{k^2}{4} x \right) - \frac{ik_z}{2} x K_{zz}(x, y), \quad (3.40)$$

$$K_{zz}(x, y) = -\frac{k^2}{2\pi bd} \left[\alpha_E + \ln \left(\frac{k}{2} \right) + \frac{1}{2} \ln(x^2 + y^2) \right], \quad (3.41)$$

with \mathbf{J} given by

$$J_{xx}(x, y) = \frac{1}{2\pi bd} \left(1 + \frac{k^2 x^2 + y^2}{2} \frac{1}{6} \right) \left[xy \arctan \left(\frac{y}{x} \right) + \frac{y^2 - x^2}{4} \ln(x^2 + y^2) \right] - \frac{1}{2} J_{zz}(x, y), \quad (3.42)$$

$$J_{xy}(x, y) = \frac{1}{2\pi bd} \left[\left(\frac{x^2 - y^2}{2} + \frac{k^2 x^4 - y^4}{2} \frac{1}{12} \right) \arctan \left(\frac{y}{x} \right) + \left(\frac{xy}{2} + \frac{k^2 x^3 y + xy^3}{2} \frac{1}{12} \right) \ln(x^2 + y^2) \right], \quad (3.43)$$

$$J_{xz}(x, y) = \frac{ik_z}{2\pi bd} \left[\frac{3x^2 y - y^3}{6} \arctan \left(\frac{y}{x} \right) + \frac{3xy^2 - x^3}{12} \ln(x^2 + y^2) - \frac{k^2 x^3 y^2}{2} \frac{1}{24} \right] - \frac{ik_z}{2} x J_{zz}(x, y), \quad (3.44)$$

$$J_{zz}(x, y) = -\frac{k^2}{2\pi bd} \left[\left(\alpha_E - \frac{25}{12} + \ln \left(\frac{k}{2} \right) \right) \frac{x^2 y^2}{4} + \frac{x^3 y - xy^3}{6} \arctan \left(\frac{y}{x} \right) + \frac{6x^2 y^2 - x^4 - y^4}{48} \ln(x^2 + y^2) \right]. \quad (3.45)$$

For $\mu \neq \nu$, explicit formulas for the demagnetizing tensor follow immediately from Eq. (3.33). The self-interaction case ($\mu = \nu$) requires a little more computational effort. Using equation (3.34), the components of the demagnetizing tensor $\Lambda_{\text{dip}}^{\mu\mu}$ are computed, this is

$$\begin{aligned} (\Lambda_{\text{dip}}^{\mu\mu})_{xx} = & \frac{1}{\pi} \left[2 \arctan \frac{d}{b} + \frac{b}{d} \ln b - \frac{d}{b} \ln d + \frac{1}{2} \left(\frac{d}{b} - \frac{b}{d} \right) \ln(b^2 + d^2) \right] \\ & + \frac{bdk^2}{48\pi} \left[-25 + 12\alpha_E + 12 \ln \frac{k}{2} + 8 \frac{b}{d} \arctan \frac{d}{b} + 6 \frac{b^2}{d^2} \ln b \right. \\ & \left. - 2 \frac{d^2}{b^2} \ln d + \left(6 + \frac{d^2}{b^2} - 3 \frac{b^2}{d^2} \right) \ln(b^2 + d^2) \right] \quad (3.46) \end{aligned}$$

and

$$\begin{aligned} (\Lambda_{\text{dip}}^{\mu\mu})_{zz} = & -\frac{bdk^2}{24\pi} \left[-25 + 12\alpha_E + 12 \ln \frac{k}{2} + 8 \left(\frac{b}{d} - \frac{d}{b} \right) \arctan \frac{d}{b} \right. \\ & \left. + 2 \frac{b^2}{d^2} \ln b + 2 \frac{d^2}{b^2} \ln d + \left(6 - \frac{b^2}{d^2} - \frac{d^2}{b^2} \right) \ln(b^2 + b^2) \right], \quad (3.47) \end{aligned}$$

and that $(\Lambda_{\text{dip}}^{\mu\nu})_{xy} = (\Lambda_{\text{dip}}^{\mu\mu})_{xz} = 0$. It is worth mentioning that the second term in Eq. (3.34) vanishes for all components.

The previous approximation holds as long as the relative distance between two sub-stripes falls below a certain threshold. In the case of self-interaction ($\mu = \nu$), it is expected that the threshold surpasses the characteristic length of the sub-stripes, namely, the diagonal $\sqrt{b^2 + d^2}$. We define the threshold as the value z at which the relative error of any of the K_0 , K_1 , or K_2 series expansion surpasses 0.05. This condition happens first for K_0 at around $z = 1/3$. Note that the argument of the Bessel functions is $z = k|\boldsymbol{\rho} - \boldsymbol{\rho}'|$. Thus, in the wave-vector regime $k \leq 30 \text{ rad } \mu\text{m}^{-1}$, this approximation holds for sub-stripes at a relative distance of no more than 11 nm. For relative distances more significant than 11 nm, a mean value approximation can be used in its place.

Applications of the theory

This chapter focuses on studying the dynamic phenomena in given systems by modifying their geometry or magnetic parameters. We will consider certain types of nanostructures that can be solved with the theoretical tools developed in Chapter 3. Ferromagnetic films, bilayer magnonic crystals, synthetic antiferromagnets, and ferromagnetic stripes will be addressed. We will discuss frequency non-reciprocity, band gaps, focalization, and localization of the spin waves. The Dynamic Matrix Method is used to solve the propagating spin-wave normal modes of the proposed systems in various settings. Then, equipped with the analytic expressions obtained in the previous chapter, we deepen the discussion of the underlying physical processes responsible for the dispersion relations and magnetization profiles. We want to highlight that the magnetic parameters for each section are not precisely the same because such sections represent different systems where the calculations were realized in different stages of this thesis. Also, we compare some results with micromagnetic simulations, where a reference is mentioned in each case.

This chapter is organized as follows. In Section 4.1 we study the spin-wave frequency non-reciprocity in magnetization-graded ferromagnetic films. Section 4.2 addresses the band structure of a bilayer magnonic crystal. In Section 4.3 we are concerned with the focusing of spin waves in synthetic antiferromagnets. Finally, Section 4.4 is about the localization of spin waves in magnetization-graded stripes.

4.1 Spin-wave non-reciprocity in magnetization-graded ferromagnetic films

DOI

Here we study the spin-wave dispersion relation of magnetization-graded ferromagnetic films. In particular, we are interested in the emergence of frequency non-reciprocity and the role played by the long-range dipole-dipole interaction. We consider thick ferromagnetic films so that the Dynamic Matrix Method is used to calculate the SW spectra because such a method takes into account the non-homogeneous dynamic magnetization profiles along the film thickness.

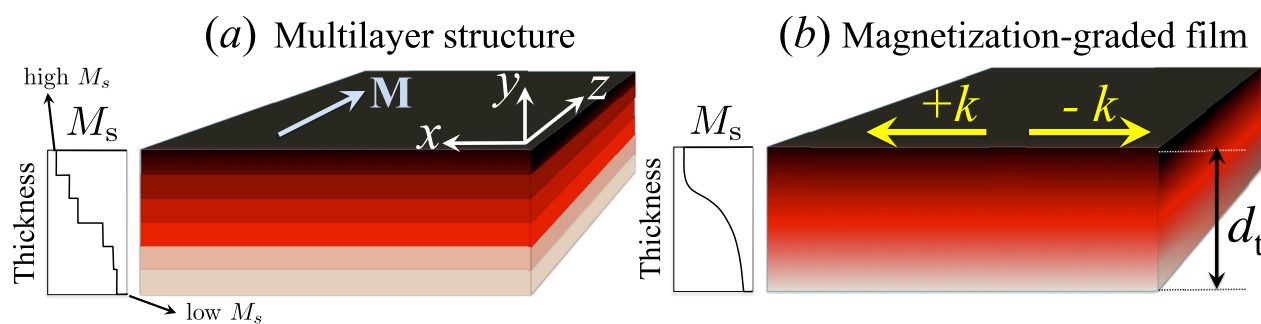


Fig. 4.1: (a) Thin film with graded magnetization along the thickness. This system is considered as a multilayer structure with varying saturation magnetization characterized by a profile $M_s(y)$. (b) Ferromagnetic film with a continuous variation of M_s . The insets show a schematic representation of the profile of $M_s(y)$ along the thickness d_t , where an increase of the saturation magnetization is given from the bottom to the top of the film. The equilibrium magnetization points along z and the spin waves always propagate along x , so that the so-called magnetostatic surface spin wave (MSSW), or Damon-Eshbach mode, will be considered.

To describe the spin-wave spectra of magnetization-graded films, we use typical parameters for Permalloy; $A_{\text{ex}} = 11$ pJ/m, and $\gamma/2\pi = 28.02$ GHz/T. In the cases where the saturation magnetization is varied, it will change from $M_s = 800$ kA/m up to $M_s = 1600$ kA/m. On the other side, for the case of constant M_s a saturation magnetization of 800 kA/m will be assumed.

The system under consideration is shown in Fig. 4.1, wherein Fig. 4.1(a) a multilayer system is shown, which is composed of sublayers with different magnetic properties. Then, by using the idea of the dynamic matrix method, the continuous variation of the magnetic characteristics is reached, as shown in Fig. 4.1(b). In the current

case, Damon-Eshbach modes are studied, where the spin-wave propagation is given perpendicular to the equilibrium magnetization.

In order to corroborate the theoretical results, we first analyze the case of uniform saturation magnetization ($M_s = 800$ kA/m) in a thick film of thickness $d_t = 60$ nm. The case is depicted in Fig. 4.2(a), where the low-frequency mode is illustrated for an external field $\mu_0 H_0 = 1.5$ mT applied along the z -direction. This field value is chosen as the minimal stabilization field in the micromagnetic simulations (some details of the simulations can be found in Refs. [33]). Here, the FM film has been modeled as a single layer with $N = 1$ (dotted line), two coupled layers with $N = 2$ (dot-dashed line), etc. The different cases quickly converge as N increases, as shown in the inset in Fig. 4.2(a), where the frequency reaches a constant value around $N = 5$. Therefore, employing this test of convergence, we can demonstrate that the theory can describe the SW dynamics of a thick ferromagnetic film, which is also verified by the micromagnetic simulations [33]. At $N = 1$, the dispersion assumes constant dynamic magnetization across the film. However, when the modulation along the thickness is allowed by increasing N , the dispersion dramatically changes. The first out-of-phase higher-order modes become less energetic than the coherent one (mode oscillating in phase) due to the dipolar contribution that favors the out-of-phase magnetic oscillations. Thus, while at low wave vectors the uniform mode is the less energetic one, at higher wave vectors a kink develops (around $|k| \approx 3$ rad / μm in Fig. 4.2) above which the low-frequency mode is now the out-of-phase one, where the precession of the outer sublayers are out of phase. Hence, the kink point represents the point around which the uniform and out-of-phase mode have the same energy, and the critical point at which the kink occurs is strongly dependent on the film thickness since at higher (lower) thicknesses, this kink point is given by lower (higher) frequency. Of course, because the in-phase and out-of-phase modes usually can not have the same energy (or frequency), the kink point is also seen as an anticrossing point.

In order to look at the SW precessional amplitudes at different sublayers of the film, the system is divided into $N = 30$ sublayers so that the thickness of each sublayer is $d = 2$ nm (being the total thickness $d_t = 60$ nm). Thus, the sublayer-dependent precessional amplitudes can be clearly observed in Figs. 2(b-c) for $k = \pm 20$ rad / μm , a wave-vector magnitude that lies within the range of Brillouin light scattering

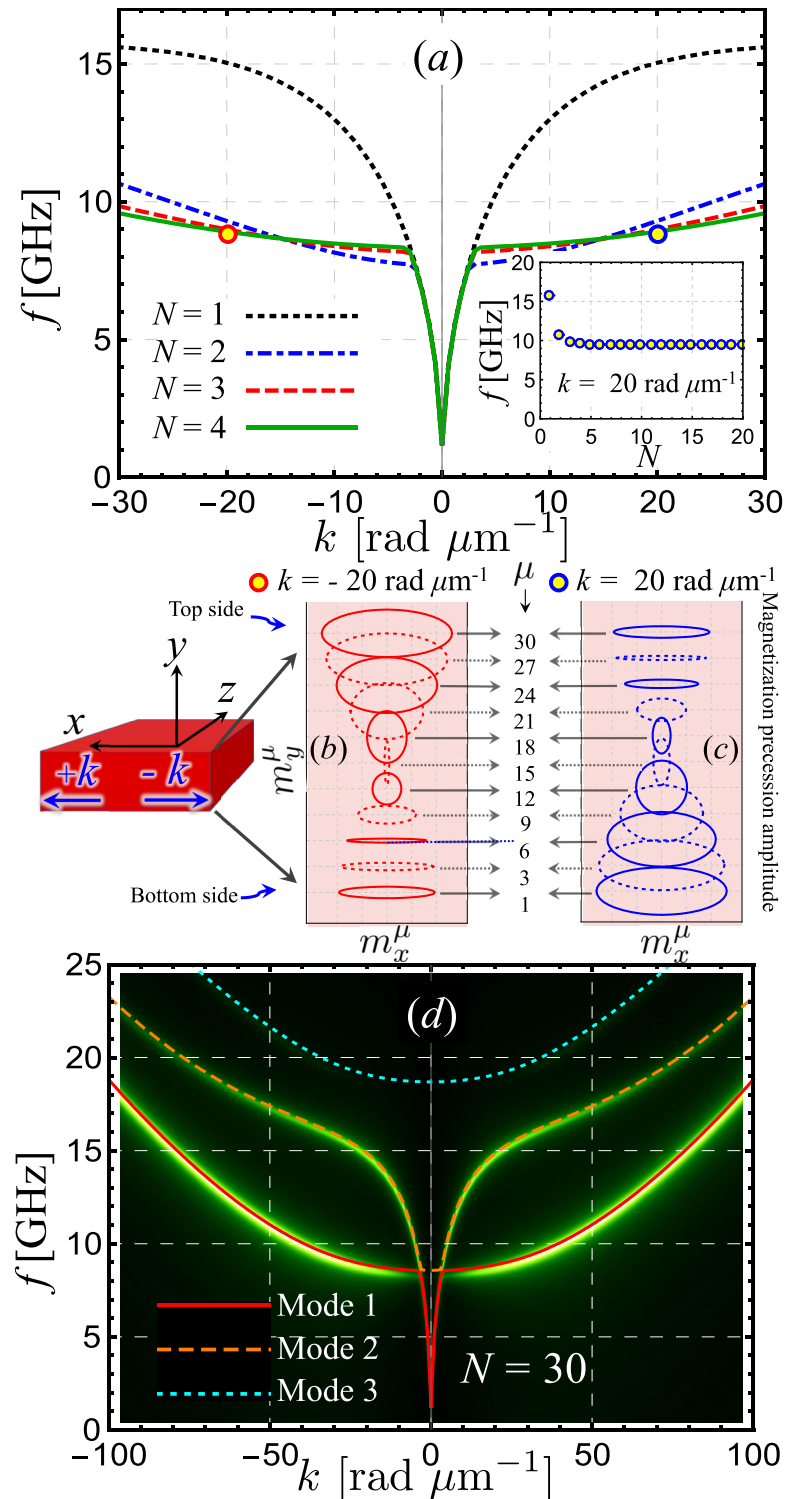


Fig. 4.2: (a) Spin-wave dispersion for a ferromagnetic film with constant saturation magnetization and total thickness $d_t = 60$ nm, which is divided into N sublayers. The inset illustrates the mode evaluated at $k = 20$ rad $/\mu\text{m}$ as a function of the number of sublayers, where a convergence is observed. (b,c) Depth-dependent magnetization precession for cases $k = \pm 20$ rad $/\mu\text{m}$, where $N = 30$ was chosen. Note that m_x^μ and m_y^μ correspond to the dynamic magnetization components that are perpendicular to the equilibrium magnetization, which is pointing along z . Also, the index μ goes from 1 to N , denoting thus the position of a given sublayer. (d) Comparison with micromagnetic simulations [33]. For the simplest case of uniform magnetization along the thickness, the frequency dispersion is clearly reciprocal.

measurements. We observe that the modes exhibit heterosymmetric profiles along the thickness [144], [146], together with a slightly different quantization condition of the standing waves in the perpendicular direction (y -axis), while the spin waves are propagating along the film's plane. In other words, for the first standing mode, the single node does not lie precisely at the center of the film. This behavior agrees with recent results described in Ref. [146]. Besides, we note that at $|k| = 20 \text{ rad}/\mu\text{m}$, the modes with $k < 0$ and $k > 0$ exhibit a different profile along the thickness, as they obtain a larger amplitude at the upper (lower) interface at negative (positive) wave vector. The standing character of the SWs can be explained through the dynamic dipolar interaction since, in essence, this asymmetric localization appears due to the asymmetry of the dipolar field within the film, which becomes prominent for thick films [144], [147], [148]. Thus, effectively the dynamic magnetization amplitude tends to compensate the dipole field asymmetry by increasing its amplitude on one side of the film [148]. Furthermore, since the dipolar interaction is k -dependent, the node positions and amplitudes of the standing modes are also k -dependent, indicating a connection between propagating (in-plane) waves and the perpendicular standing SWs. If the thickness is reduced (comparable with the exchange length), then the magnetization amplitudes on top and bottom are approximately equal, in such a way that the non-reciprocity is also reduced. Due to the breaking of symmetry along the thickness, non-reciprocity in frequency for two counterpropagating SWs is expected [148], as long as the FM film is thick enough so that the spin-wave amplitude is non-uniform along the thickness¹.

After describing the SW dynamics in the case of a homogeneous FM film, we will now address that of a system with graduated magnetization. Fig. 4.3 shows the SW spectra for different systems with $N = 30$, where the breaking of symmetry along the thickness has been included through a variation on M_s . Three cases are explored: Case 1: A smooth change of M_s whose profile is asymmetric with respect to the film thickness. Case 2: A smooth change of M_s around the center of the film thickness. Case 3: A linear variation of the saturation magnetization along the thickness. In all cases, the low frequency mode (Mode 1) at $k = \pm 20 \text{ rad}/\mu\text{m}$ corresponds to an out-of-phase one. Case 1 is illustrated in Fig. 4.3(a), where the

¹Nevertheless, if some interfacial effect, such as those induced by interfacial anisotropies or spin pumping, a notable non-reciprocity in the SW amplitudes can be observed [3], [149].

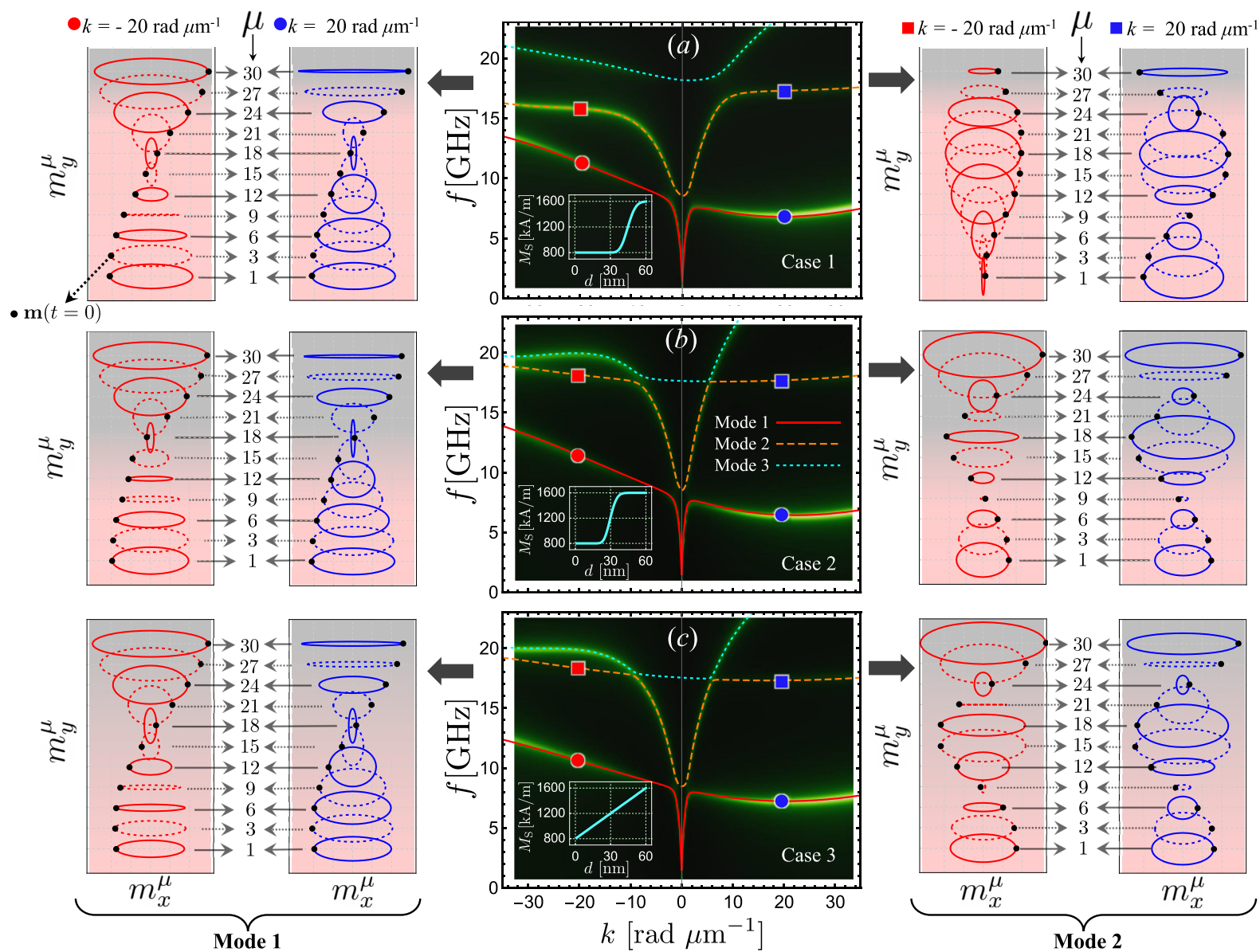


Fig. 4.3: Figure (a) shows the spin-wave dispersion of a $d_t = 60$ nm film for Case 1, where a smooth change of M_s is given in the top of the film. In (b) the Case 2 is depicted, where there is a smooth change of the saturation magnetization at the center of the film. Figure (c) illustrates Case 3, where a linear variation of the saturation magnetization is given. The saturation-magnetization profiles are shown in the respective insets. The right and left figures show the precessional amplitudes for the individual cases at $k = \pm 20$ rad / μm , where the time $t = 0$ has been highlighted (see filled black dots) to see the phase of the modes. The color code represents the numerical simulations, where the brighter color indicates a maximum of the response.

smooth change in M_s influences the SW dynamics since the symmetry along the thickness has been broken. For waves propagating along x , the frequency of Mode 1 is reduced in comparison to a counterpropagating wave so that the localization of the SW is different as well, as shown in the left side of Fig. 4.3(a). Interestingly, the second mode also manifests non-reciprocity, which can be explained by analyzing the precessional amplitudes of Mode 2, as shown on the right side of Fig. 4.3(a).

Here, it is easy to note that the second mode at $k = -20 \text{ rad}/\mu\text{m}$ manifest a coherent precession, with different magnetization amplitudes along the thickness, while for waves propagating at $k = 20 \text{ rad}/\mu\text{m}$, the mode is the one with two nodes. Thus, it can be inferred that the nature of the non-reciprocity of the second mode for Case 1 is mainly because the nature of the SW localization has been radically modified by inverting k .

Case 2 is depicted in Fig. 4.3(b). For such saturation-magnetization profile, it is evident that the first mode manifests a slightly larger non-reciprocity than Case 1. Nevertheless, Mode 2 is almost symmetric concerning the wave-vector inversion, which can be understood by analyzing the SW amplitudes at $k = \pm 20 \text{ rad}/\mu\text{m}$, since for both counterpropagating waves, the excitations are of the same nature with similar precession amplitudes. Case 3 is shown in Fig. 4.3(c), which is quite similar to Case 2. A possible explanation for this unexpected behavior may be the localization of the maxima of the precessional amplitude since for both cases; these maxima are given in the bottom and top sides of the film, where M_s is the same for Case 2 and Case 3. Note that overall the frequency non-reciprocity is accomplished of a non-reciprocity of the magnetization precession amplitude [see the top and bottom faces in Figs. 2(b) and (c)] so that the output signal amplitude (of a given measurement) will be asymmetric for the wave-vector inversion. This property is helpful for spin-wave logic, and switch applications [3], [9], and spin-wave isolators [150], where the spin-wave amplitude is wave-vector dependent.

To deeply understand the non-reciprocity induced by the graduation of M_s , the first mode of Case 1 will be analyzed from the point of view of the dipolar interaction. From the precessional amplitudes shown in Fig. 4.4(a-b), it can be inferred that the role of the bottom and top sublayers is preponderant for the occurrence of spin-wave non-reciprocity. Therefore, the dipolar interaction between layer $\mu = 30$ and $\nu = 1$ will be analyzed. The components of the dipolar field acting in sublayer μ due to sublayer ν are given in Eqs. (3.25) and (3.26). Here, it is evident that the terms that induce non-reciprocity are the ones proportional to ik , in such a way that if the non-reciprocal parts of these fields are defined as $\mathbf{h}_{\text{nr-dip}}^n = -(\hat{\mathbf{x}} \otimes \hat{\mathbf{y}} + \hat{\mathbf{y}} \otimes \hat{\mathbf{x}}) \cdot \mathbf{\Lambda}_{\text{dip}}^{\mu\nu} \cdot \mathbf{m}^\nu e^{i(\mathbf{k}\cdot\mathbf{r}-\omega t)}$, then the relative orientation of field $\mathbf{h}_{\text{nr-dip}}^{30,1}$ (non-reciprocal dipolar field acting on sublayer $\mu = 30$ due to sublayer $\nu = 1$) and the dynamic magnetization of the sub-layer 30 can be analyzed. Fig. 4.4(c)

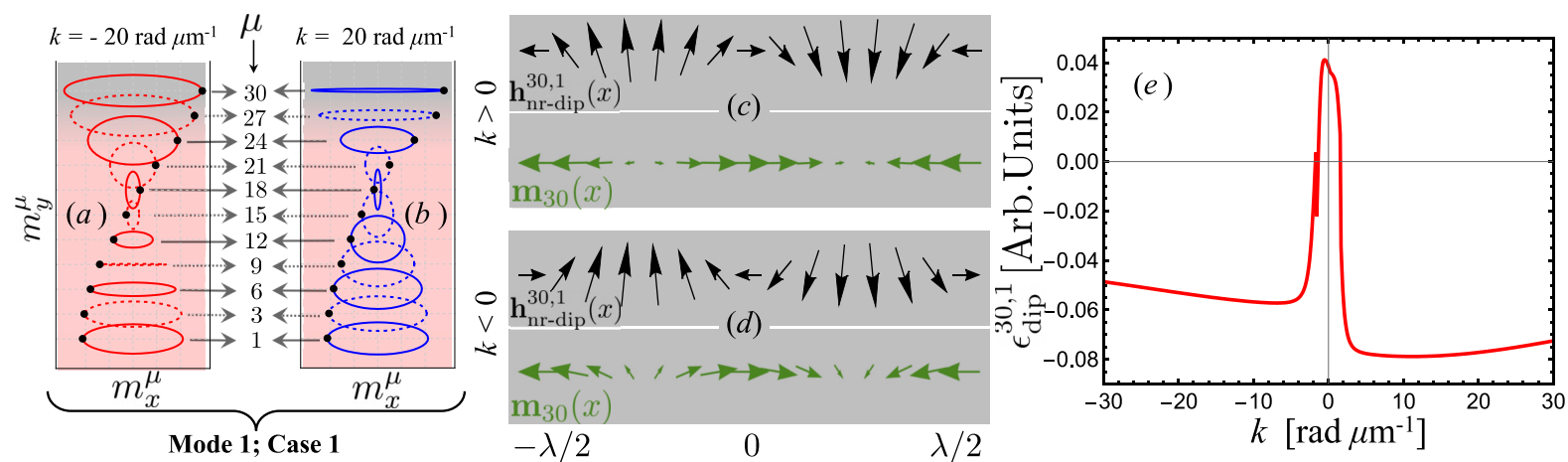


Fig. 4.4: (a) and (b) show the precessional amplitudes for Case 1. In (c) and (d) the relative orientation of the dynamic magnetization of sublayer $\mu = 30$ and dipolar field $h_{\text{nr-dip}}^{30,1}$ (see text for details) is shown for $k > 0$ and $k < 0$, respectively. The dipolar interaction between sublayer $\mu = 1$ and $\mu = 30$, as a function of the wave vector, is depicted in (e), where an evident reduction of the dynamic dipolar energy is observed for $k > 0$, in agreement with the relative orientations between the dynamic stray field and the dynamic magnetization shown in (c).

and (d) show the field $h_{\text{nr-dip}}^{30,1}$ and the dynamic magnetization of sublayer $\mu = 30$ at $k = \pm 20 \text{ rad } / \mu\text{m}$. At $k < 0$, it is noted that the in-plane dynamic magnetization m_x^{30} is opposite to the field $(h_{\text{nr-dip}}^{30,1})_x$, in such a way that the dipolar interaction due to in-plane components increase the energy of the system. Nevertheless, the out-of-plane components reduce the energy since the dipolar interaction and the dynamic magnetization are parallel. On the other hand, the opposite happens at $k > 0$. However, by noting that the in-plane components of the dynamic magnetization and the dynamic stray field are the ones that dominate the interaction between sublayers 1 and 30 ($\epsilon_{\text{dip}}^{30,1}$), then one can conclude that $f(+k) < f(-k)$. Here $\epsilon_{\text{dip}}^{\mu\nu} = (\mu_0/2)\mathbf{m}^\mu \cdot \mathbf{\Lambda}^{\mu\nu} \cdot \mathbf{m}^\nu$. This is shown in Fig. 4.4(e), where an evident reduction of the dipolar interaction is given for $k > 0$.

Fig. 4.5 shows the frequency shift $\Delta f = f(-k) - f(+k)$ between two counter-propagating SWs, for the first mode and three different thicknesses $d_t = 30, 60$ and 120 nm . The insets in each figure depict a reduced range of wave vectors, which is the typical range probed by Brillouin light scattering measurements [151]. The overall behavior of the Δf shows two critical wave vectors where the frequency shift becomes zero [see points A and B in Fig. 4.5(a)]. As the thickness increases point A appears at lower k values so that it is imperceptible for thicker films. Critical point A corresponds to the kink discussed above, which indicates the wave vector where the

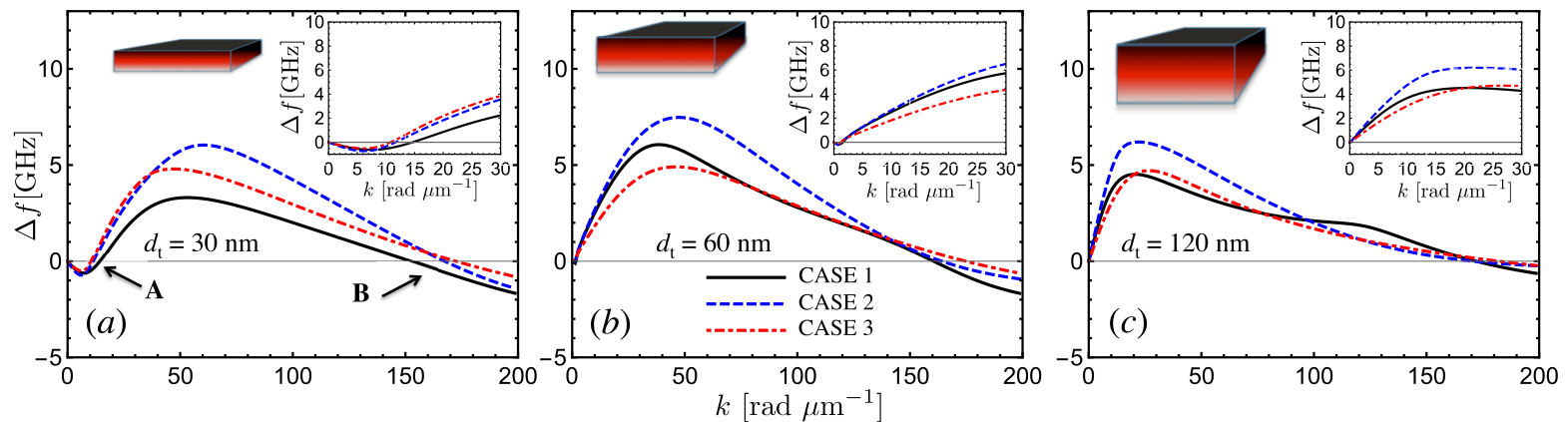


Fig. 4.5: Frequency shift Δf of Mode 1 as a function of the wave vector for Cases 1, 2 and 3. (a), (b) and (c) show the frequency shift for $d_t = 30$ nm, $d_t = 60$ nm and $d_t = 120$ nm, respectively. The insets illustrate the range of k -values probed by Brillouin light scattering measurements.

branch changes its phase, while point B is related to decreasing the dipolar energy as k increases. One can see that the thickness is very relevant for manipulating the magnitude of the frequency shift since if the sample is too thin or thick, then Δf is small in both cases. Thus, an optimal film thickness induces a large magnitude of the frequency shift.

Conclusions The spin-wave dynamics of a ferromagnetic film with graded magnetization saturation have been studied utilizing the Dynamic Matrix Method. It is demonstrated that the properties of the SWs in these films are notoriously modified compared to films with uniform magnetization. Interesting non-reciprocal and particular localization properties have been found, where a notable frequency shift is predicted, which is attributed to the dipolar interaction that is enhanced when a breaking of spatial symmetry along the thickness is present. An arbitrary profile of the saturation magnetization or any other magnetic parameter (surface anisotropy, exchange constant, etc.) can be described with the method developed here. Controlled by the graded profile, it is possible to obtain two counterpropagating waves where the phase of the mode can be radically different, depending on the SW propagation direction. Thus, this work proposes a way to tune the dynamic properties of SWs by introducing graduation of the magnetic properties, which is considered relevant for applications of magnon-based devices.

4.2 Band structure of a one-dimensional bilayer magnonic crystal

DOI

In this section, the dynamic properties of a bilayer one-dimensional bi-component magnonic crystal (MC) are studied using theoretical tools shown in chapter 3 for periodic systems (see Section 3.1.2). We could say that we use the periodic extension of the Dynamic Matrix Method for $N = 2$. Diverse geometrical configurations are analyzed, where the band structure of these MCs and spatial profiles of the collective modes are discussed.

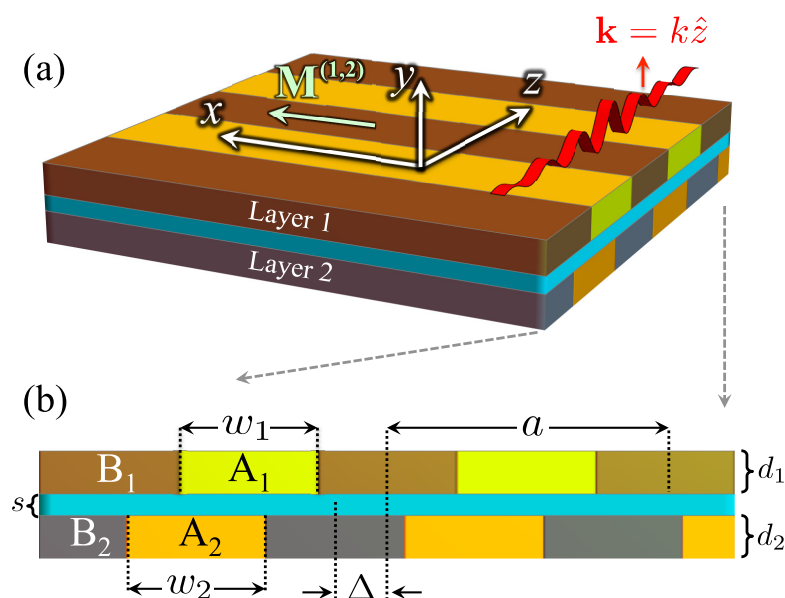


Fig. 4.6: (a) Overview of a 1D bi-component bilayer MC. The collective modes propagate along z , whereas the equilibrium magnetization is pointing along x . y is the normal axis. As reference, the top (bottom) MC layer is labelled $\nu = 1$ ($\nu = 2$). (b) Cross-section of a bilayer MC. Layer ν has magnetic components A_ν and B_ν , the width of the material A_ν being w_ν . Also, a displacement parameter Δ is introduced to describe an indirect coupling between layers 1 and 2. a is the lattice parameter, which is assumed to be the same for both MCs, and s is the thickness of the non-magnetic spacer.

The periodic bilayer system is shown in Fig. 4.6, where the geometrical parameters of the structure are defined. Standard values of Cobalt and Permalloy[152] are used for both bi-components. Specifically, the magnetic properties of material $A_1 = A_2 = A$ [Permalloy ($\text{Ni}_{80}\text{Fe}_{20}$)] are $M_s^A = 750$ kA/m and $\ell_{\text{ex}}^A = 6.1$ nm, whereas for material

$B_1 = B_2 = B$ (Cobalt), they are $M_s^B = 1200$ kA/m and $\ell_{\text{ex}}^B = 4.7$ nm. For both materials, an effective gyromagnetic ratio $\gamma = 0.01856$ GHz/G and thickness $d_{1,2} = 10$ nm are used. Also, the lattice parameter of the crystal is $a = 300$ nm, and the separation of the layers is $s = 1$ nm. As can be seen in Fig. 4.6, the Damon–Eshbach modes (SW propagation perpendicular to the equilibrium magnetization) are studied. Note that the equilibrium magnetization is pointing along the stripes of the 1D bilayer MC, and this state is stable in the absence of an external field, unlike the backward volume configuration (equilibrium magnetization perpendicular to the stripes), where a non-zero external field is required to make such a configuration stable. Therefore, in what follows, a zero bias field is assumed. To systematically study the band structure of a bilayer 1D bi-component MC, different coupling configurations were analyzed by (i) independently switching on and off the interlayer and dipolar interactions; (ii) varying the width w_1 , so that the transition from two coupled MCs (MC/MC) to an MC coupled with a ferromagnet (MC/FM) could be considered; and (iii) varying the displacement parameter Δ [see Fig. 4.6(b)].

Role of interlayer interactions Fig. 4.7(a–c) shows the SW dispersion curves of a monolayer MC, an exchange-coupled bilayer MC and a dipolar-coupled bilayer MC, respectively. Here, the first BG (1st BG) has been highlighted. In all three cases, the width of material A is half of the lattice parameter ($w_{1,2} = a/2$). In the dispersion curves, the points at $k = \pi/2a$ (around 5.2 rad/ μm) have been highlighted to analyze the spin-wave profiles at such wave vectors [see Mode I, Mode II, Mode III, and Mode IV in Fig. 4.7(a)]. In Fig. 4.7(a), the bands of an isolated MC show a typical SW spectrum, which is characterized by the emergence of magnonic BGs that are induced by the periodic magnetic contrast (periodic variations of M_s and ℓ_{ex}) along z . The real part of the in-plane magnetization component ($\text{Re}[m_z^{(\nu)}]$), in arbitrary units, is plotted at $k = \pi/2a$, where one sees that the low-frequency mode (Mode I) is mainly located in the low M_s material (central lighter part), whereas the high-frequency modes (Modes II, III, and IV) are located in both materials A and B. The SW localization observed for the low-frequency mode can be explained by the fact that the frequency of a continuous Py (evaluated at $k = \pi/2a$) is close to Mode I, unlike the Cobalt dispersion that is given at higher frequencies. Hence, the oscillations in the Cobalt are forced by the magnetization oscillations in Py.[138]

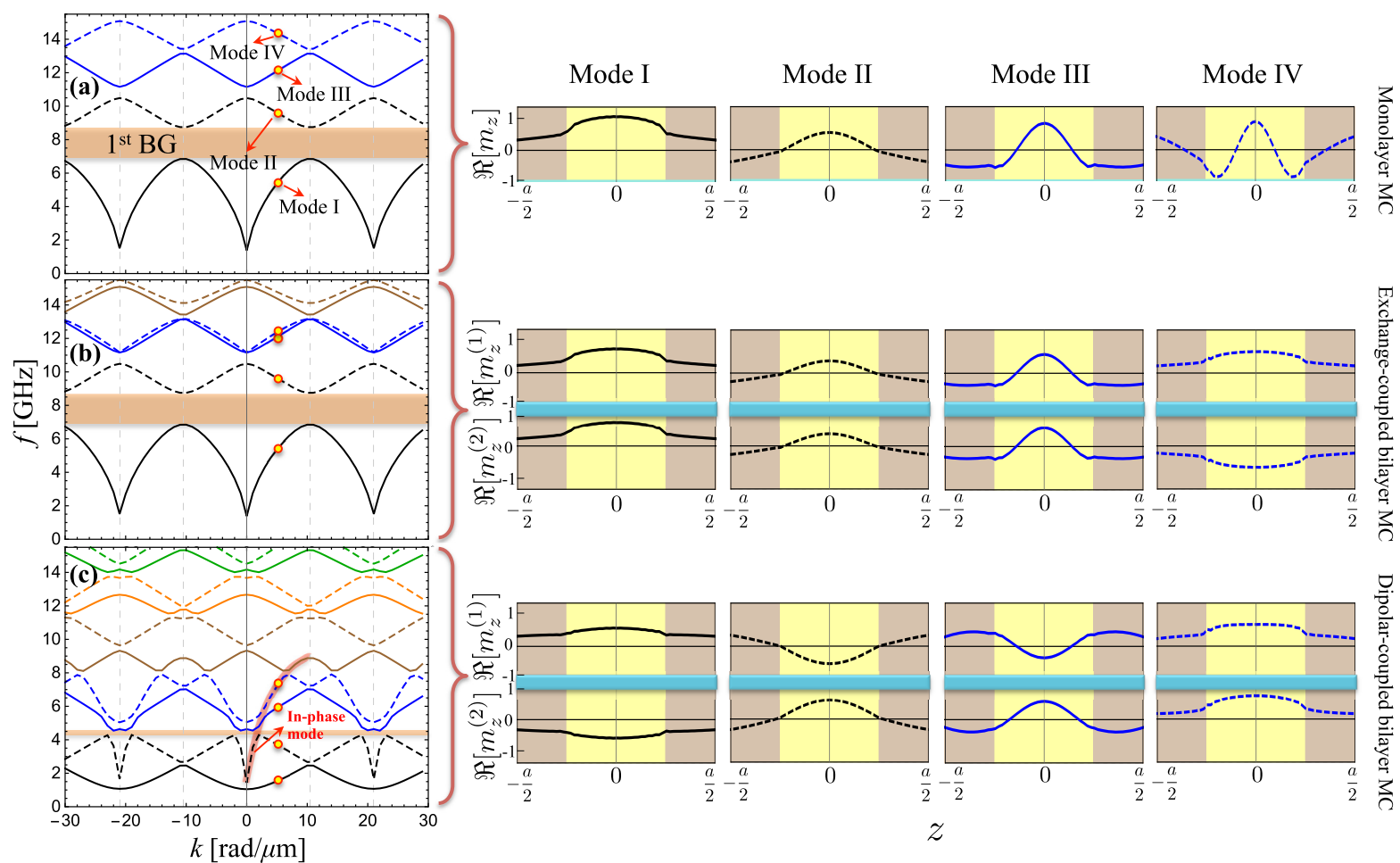


Fig. 4.7: SW dispersion curves of (a) a monolayer 1D bi-component MC, (b) an exchange-coupled bilayer MC and (c) a dipolar-coupled bilayer MC. The point $k = \pi/2a$ is highlighted in the dispersion curves for the first four branches (Modes I, II, III, and IV), whereas the real part of the in-plane magnetic components ($\text{Re}[m_z^{(\nu)}]$) are shown in the panel to the right of each plot. Dynamic components $m_z^{(\nu)}$ are expressed in arbitrary units. In (a)–(c) the first band gap is highlighted

Suppose one MC layer is coupled with another bi-component MC via the interlayer exchange interaction (with $J = 0.5 \text{ mJ/m}^2$). In that case, the modes that are oscillating in phase (the phase will be associated to the in-plane magnetization components) do not noticeably change their frequency compared with those for the monolayer MC [see Modes I, II and III of Fig. 4.7(a) and (b)]. Nevertheless, at a given frequency, the out-of-phase modes appear so that the SW spectrum is now altered. These out-of-phase branches are located at high frequencies [see Mode IV in Fig. 4.7(b)] because the dynamic interlayer energy is also high when the in-plane components of the magnetization are antiparallel (out-of-phase character). Below of the out-of-phase modes, the band-gap widths of a monolayer MC and a bilayer MC have the same magnitude [see 1st BG in Fig. 4.7(a) and Fig. 4.7(b)].

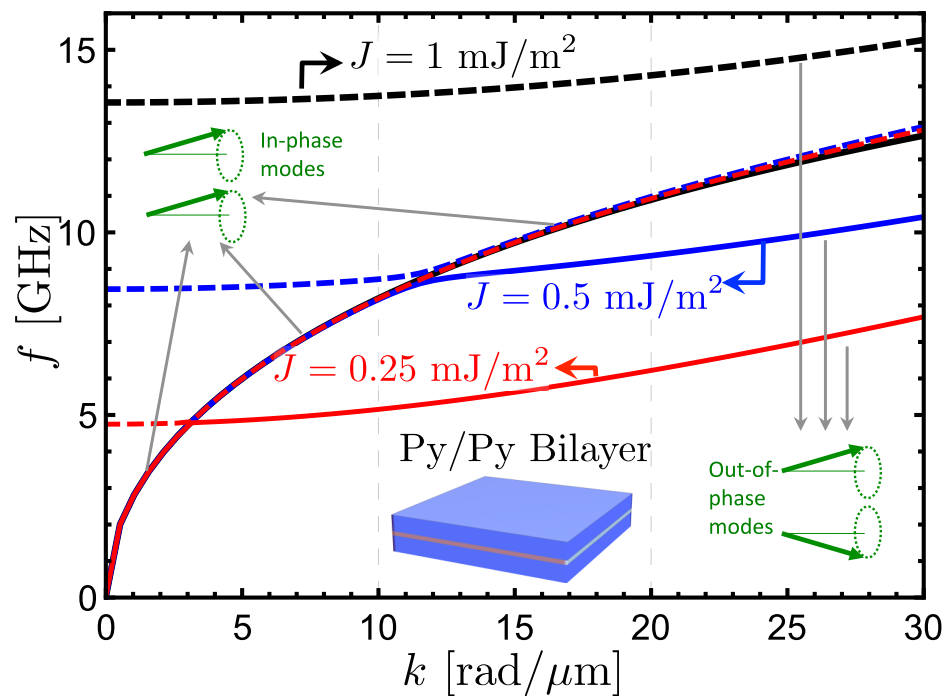


Fig. 4.8: Dispersion relation in a coupled bilayer system. Three cases are depicted, where the interlayer interaction is reduced from $J = 1 \text{ mJ/m}^2$ up to $J = 0.25 \text{ mJ/m}^2$. Under the reduction of the interlayer exchange energy, the out-of-phase mode is shifted down in frequency, while the in-phase mode is not notoriously modified.

If now the dipolar interaction is considered with the interlayer exchange interaction switched off, the SW dispersion curves of the bilayer structure are considerably modified. In this circumstance, the modes with an out-of-phase character are now of low energy because the dynamic magnetization follows a flux-closing, thus reducing the stray field or dynamic dipolar interaction. Thus, such modes are excited at low frequencies. This behavior is observed in Fig. 4.7(c) and their respective spin-wave profiles. The reduction of energy of the out-of-phase modes is also present in a continuous bilayer system. Fig. 4.8 shows the dispersion relation of a simple Py/Py structure, where it is observed that under the reduction of the interlayer exchange constant J , the out-of-phase modes shift down in frequency. An exciting feature of the SW dispersion is that the in-phase mode is not notoriously modified with the modulation of J so that even at $J = 0$, the dispersion of such mode is almost unaltered. This behavior is also observed in Fig. 4.7(c) (see the thick shaded line in the range $k = 0$ and $k = \pi/a$), where the in-phase mode in the low-frequency range follows the trend of the in-phase mode shown in Fig. 4.7(b) in the same k -range. Band gaps are also modified in the case illustrated in Fig. 4.7(c), where it is observed that a mini-band gap (with a BG width $< 0.4 \text{ GHz}$) is now the first BG. Interestingly, this mini-band gap appears out of the Brillouin zone edges and is

formed by the interaction of fast and slow waves propagating with different group and phase velocities. This behavior has been previously observed in bilayered MCs with micron-size periodicity, where the coupling between MCs is provided via the microwave electromagnetic fields.[153], [154] However, as will be shown in the following sections, under realistic values of the interlayer strength J , low-frequency in-phase modes will be mainly obtained and, therefore, for such frequency regime, the interlayer exchange interaction will be particularly analyzed.

From these results, one can observe that the influence of both dipolar and exchange interactions modifies the band structure of the bilayer MC enormously. These changes in the SW spectra, together with its great versatility regarding the manipulation of magnetic and geometric parameters, motivate the study of these multilayers structures as there are many ways to control the propagation of the collective spin modes, such as i) modifying the properties of the spacer (for instance, by enhancing or depleting the interlayer exchange interaction), ii) changing the manner of coupling between the MC layers (see the following sections), iii) inducing an antiparallel alignment of the magnetizations, iv) changing from DE to the backward volume geometry (magnetization parallel to the SW propagation), where the edge modes are prominent, etc.

Variation of width w_1 This section describes the transition from an MC/MC to an FM/MC system. For the analysis, the width w_1 (width of material A of layer 1) is varied. Fig. 4.9 shows the SW spectra for different values of w_1 , from $a/2$ to 0, where $a = 300$ nm. In Fig. 4.9(a–c), the interlayer exchange constant is $J = 0.5$ mJ/m², whereas in Fig. 4.9 (d–f), $J = 1$ mJ/m². In comparing Fig. 4.9(a–c) and Fig. 4.9(d–f), the low-frequency mode is noted to be slightly influenced by the increase in the interlayer exchange interaction, whereas the high-frequency modes are different. In the instances displayed in Fig. 4.9(a–c), there are many high-frequency branches in the range 11–15 GHz, whereas in Fig. 4.9(d–f) only two modes are observed in the same range. Because the interlayer exchange is reduced in Fig. 4.9(a–c), the dipolar interaction becomes more relevant and tends to reduce the frequency (or energy) of the out-of-phase modes (see discussion in Sec. ??A). Overall, the reduction in the frequency of the modes leads to flat modes just above the first BG. Nonetheless, if

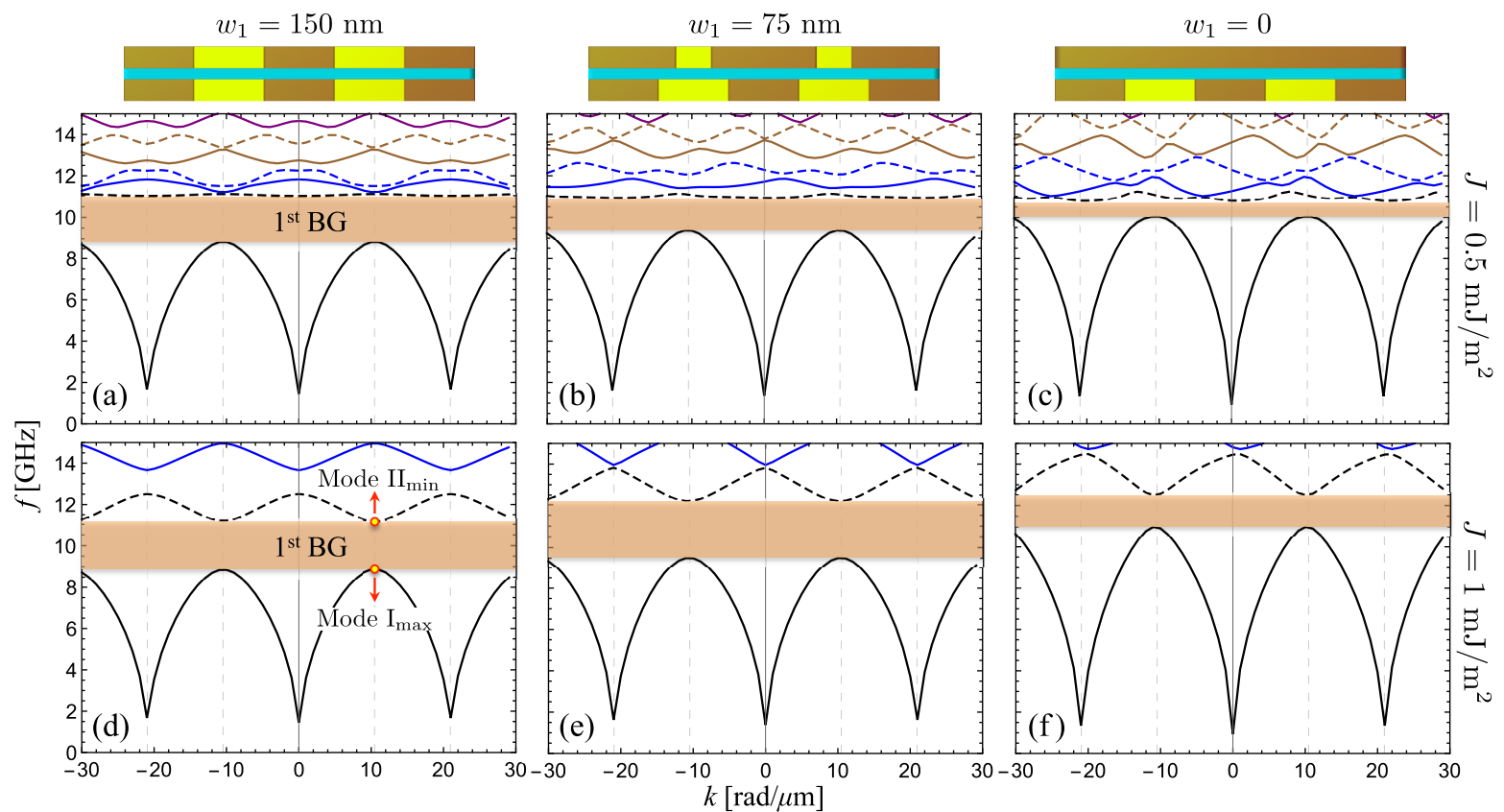


Fig. 4.9: Band structure of the collective SWs for different values of w_1 : the exchange constant is (a–c) $J = 0.5 \text{ mJ/m}^2$ and (b–f) $J = 1 \text{ mJ/m}^2$. In (d), the modes at the edges of the first band-gap have been highlighted.

the interlayer exchange coupling is even lower, the reduction in the frequency of the flat modes similarly decreases the BG width as in Fig. 4.7(c).

The first BG is highlighted in the dispersion curves (Fig. 4.9), where it is seen that the BG width is reduced as w_1 decreases [Fig. 4.9(a–c)], whereas in Fig. 4.9(d–f) a non-monotonic behavior is seen because at $w_1 = 75 \text{ nm}$ the BG width is higher than that for $w_1 = 0$ and $w_1 = 150 \text{ nm}$. This peculiar behavior is observed in Fig. 4.10, where the width and center of the first BG are depicted as a function of w_1 . In Fig. 4.10(a) is observed that at $J = 0.5 \text{ mJ/m}^2$ (solid line), the BG width decreases if w_1 is reduced, while at higher values of J (dashed and dotted lines), a non-monotonic behavior is obtained. Note that the increase of the BG width is accompanied by a shift to higher frequencies of the BG center [see Fig. 4.10(b)] when w_1 goes to zero. By comparing a bilayered MC with a monolayer MC (dots in Fig. 4.10) one can see that the BG width is more significant for a bilayer and that its center is located at higher frequencies. The latter can be understood due to the dipolar interaction since overall, the band-gap edges are modes oscillating in phase. Therefore the interlayer dipole-dipole interaction represents an extra

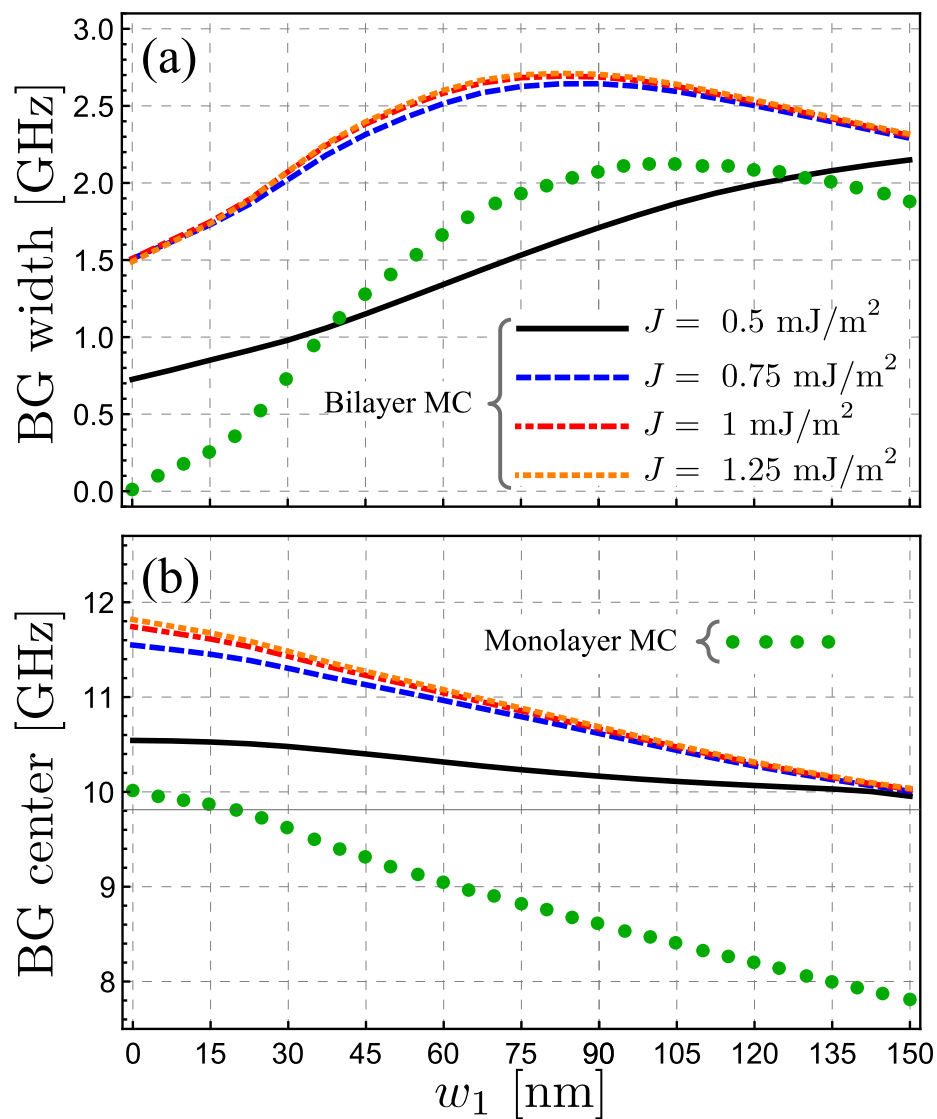


Fig. 4.10: Plot (a) shows the band-gap width as a function of w_1 for different values of the exchange constant (lines), while dots illustrated the case of a monolayer magnonic crystal (monolayer MC). In (b) the band-gap center against w_1 is depicted.

energy contribution that shifts the BG edges, and hence the BG center, to higher frequencies. To understand the physical mechanism that governs the behavior of the BG when w_1 is modulated, the interlayer exchange energy density $\epsilon_{\text{int}}(z)$ is analyzed. From Sec. 3.2.1, one can demonstrate that

$$\epsilon_{\text{int}}(z) = -\frac{J}{M_s^1(z)M_s^2(z)} \left[m_y^1(z)m_y^2(z) + m_z^1(z)m_z^2(z) \right]. \quad (4.1)$$

Then, this interaction is averaged in the unit cell so that $\bar{\epsilon}_{\text{int}} = (1/a) \int_0^a \epsilon_{\text{int}}(z) dz$. Fig. 4.11 shows $\bar{\epsilon}_{\text{int}}$ as a function of w_1 evaluated at the BG edges [modes I_{max} and II_{min} shown in Fig. 4.9(d)], where it is observed that as w_1 decreases the interaction energy $\bar{\epsilon}_{\text{int}}$ of both modes I_{max} and II_{min} increases. The reason behind the increase of $\bar{\epsilon}_{\text{int}}$ when w_1 decreases lies in the fact that the dynamic magnetization components

are not completely parallel if $w_1 < a/2$. For instance, at $w_1 = a/2$ one can observe that $\mathbf{m}^1(z)$ and $\mathbf{m}^2(z)$ are practically parallel (see SW profiles at $w_1 = a/2 = 150$ nm in Fig. 4.11). Nevertheless, when $w_1 < a/2$ the dynamic magnetization components are not completely parallel anymore (see SW profiles at $w_1 = 0$ and $w_1 = 75$ nm), in such a way that now $\bar{\epsilon}_{\text{int}}$ is higher according to Eq. (4.1). Note that the maximum separation of the modes I_{max} and II_{min} occurs at around $w_1 = a/4$ (75 nm), which is consistent with the highest BG width value obtained in Fig. 4.10(a). This maximum BG width will be located at $w_1 = 75$ nm as long as the modes at the BG edges correspond to the in-phase ones. In the case of $J = 0.5$ mJ/m² [solid line in Fig. 4.10(a)], it is possible to show that the dynamic magnetizations of mode II_{min} are oscillating out of phase; therefore, in this case, the interlayer dipolar interaction influences the frequency position of such mode inducing, thus, a monotonic decrease of the BG width.

Non-reciprocal properties are also observed when the symmetry along the thickness is broken [see Fig. 4.9(b,c) and 4.9(e,f)], so that two counterpropagating collective SWs, with wave vectors of the same magnitude, exhibit non-reciprocity in frequency due to the dipolar interaction.[4], [43], [140], [148] The exciting result is that the low-frequency mode behaves almost reciprocally, whereas the high-frequency modes are non-reciprocal. This behavior is understood by noting that the interlayer dipolar interaction depends on the sign and magnitude of the wave vector [see Eqs. (3.25) and (3.26)]. At $k = 0$, the interlayer dipolar interaction becomes zero and increases non-monotonically with magnitude k . [33] Therefore, because the high-frequency modes are coupled with high values of the lattice vector \mathbf{G} , these modes are influenced more by the dipolar interaction, and consequently, they are more non-reciprocal than the fundamental mode. If the contrast between materials A and B increases, the non-reciprocal behavior of the SW spectra becomes more evident (not shown), since the interlayer dipolar fields that induce the non-reciprocity depend on the magnetic contrast.

Variation of the displacement parameter Δ Next, the band structure of the bilayer MC is analyzed for different values of the displacement parameter Δ . The modes as a function of k are shown in Fig. 4.12, where Δ varies from zero to $a/2$ for two settings of the exchange constant, $J = 0.5$ mJ/m² and $J = 1$ mJ/m². As

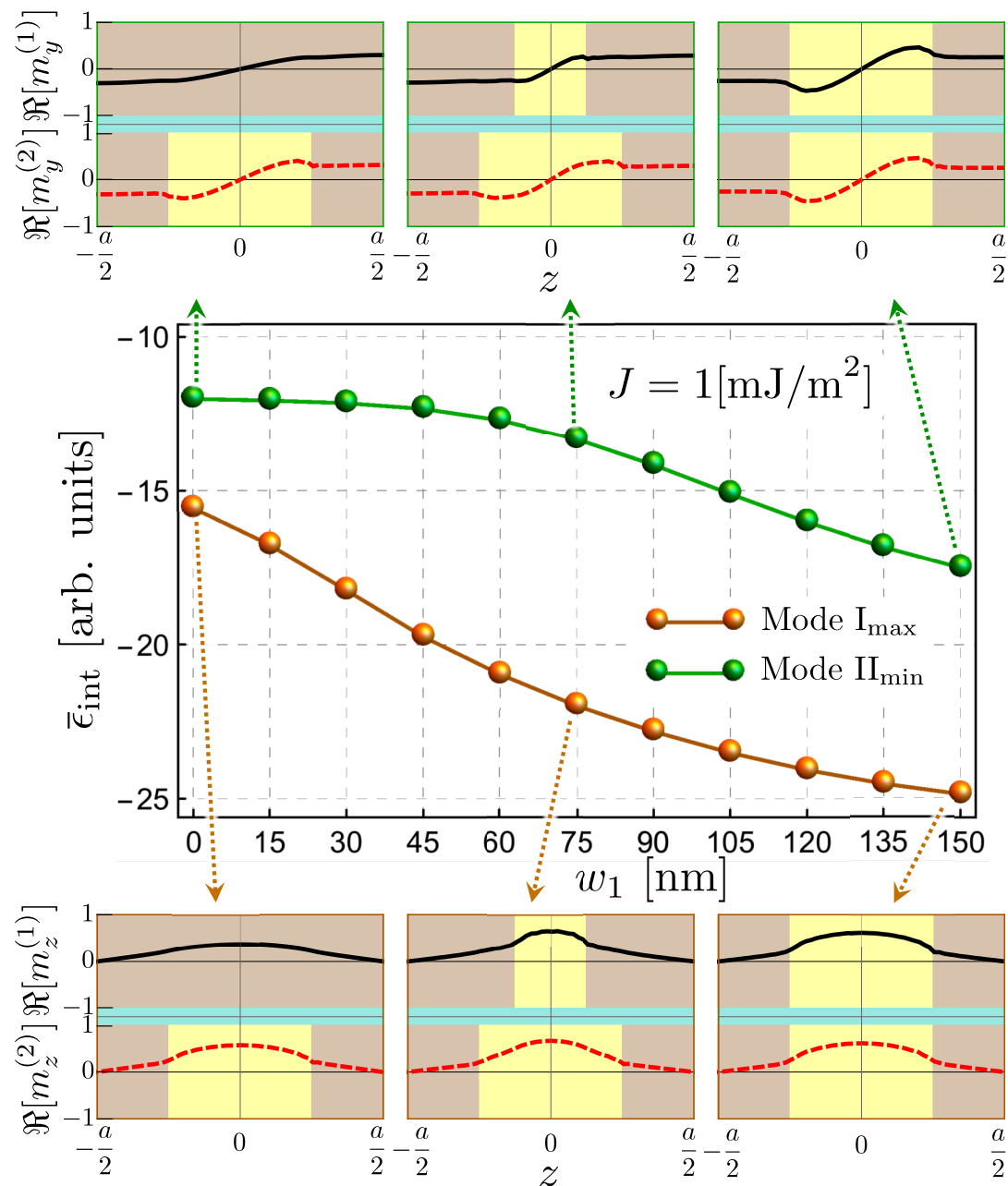


Fig. 4.11: The interlayer energy density $\bar{\epsilon}_{\text{int}}$ of modes I_{max} and II_{min} as a function of width w_1 is depicted. The SW profiles for cases $w_1 = 0$, $w_1 = 75$ nm and $w_1 = 150$ nm are shown.

expected, the dispersion is modified significantly when Δ increases; here, the most striking result is the reduction of the first BG, reaching a null BG width at $\Delta = a/2$. Furthermore, one can see that the SW dispersion is always reciprocal in frequency. This result is expected because the increase of Δ does not break symmetry along the thickness. In other words, the change of sign in k is analogous to rotating the bilayer system 180° around an in-plane axis and, since there is no breaking of symmetry along the thickness, both cases (k and $-k$) turn out to be similar. The width and center of the first band gap are illustrated in Fig. 4.13 as a function of the displacement Δ for different values of the interlayer exchange constant. In Fig. 4.13(a) it is observed that when Δ increases the BG width always decreases, reaching the zero

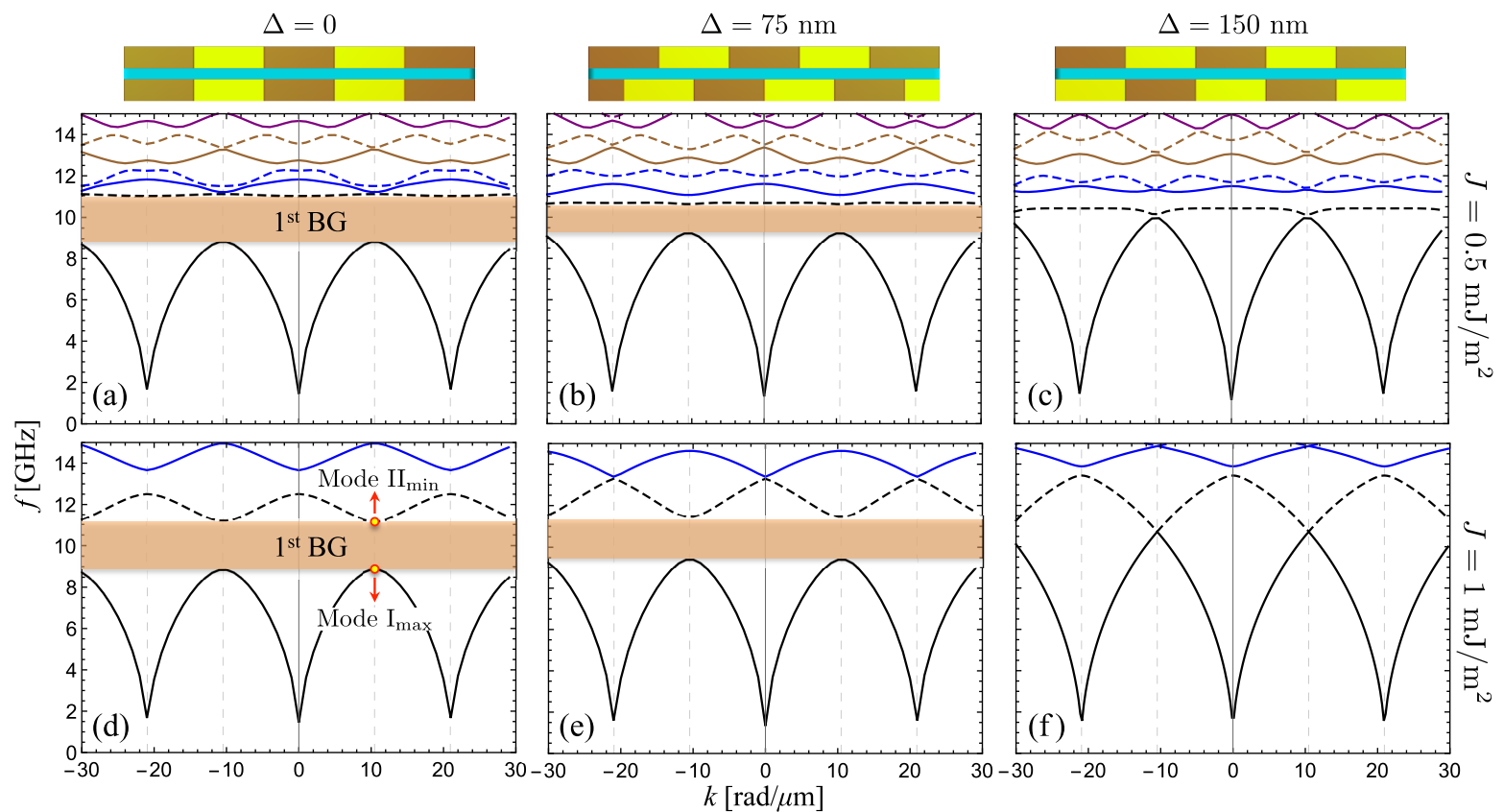


Fig. 4.12: Band structure of the collective SWs for different values of Δ . In (d), the modes at the band-gap edges are highlighted (see Fig. 4.14).

value at $\Delta = a/2$, while the BG center [see Fig. 4.13(b)] shifts up in frequency depending on the magnitude of J . The notorious contrast in the behavior of the forbidden band between the cases $J > 0.75 \text{ mJ/m}^2$ and $J = 0.5 \text{ mJ/m}^2$, as seen in Fig. 4.13, is related to the different oscillatory characteristics of the modes at the BG edges. While in the latter case, the high-frequency BG edge (Mode II_{min}) is an out-of-phase oscillatory state, the former cases correspond to in-phase states. Therefore, this oscillatory characteristic of the modes induces different behaviors of the forbidden band.

To understand the behavior obtained in Figs. 4.12 and 4.13, the absolute values of the in-plane magnetization components ($|m_z^v|$) at the 1st BG edges are calculated for different values of Δ . In Fig. 4.14(a,b), one can see that the standing wave character of Mode I_{max} exhibits an explicit node in a zone with high saturation magnetization (darker color), whereas Mode II_{max} has a node in a zone with low saturation magnetization (lighter color). This behavior is similar to a monolayer bi-component MC (not shown). In Fig. 4.14(b), the zone with reduced M_s along the thickness has been outlined with a dotted rectangle (in which the node appears). When Δ increases, the zones with reduced saturation magnetization along the

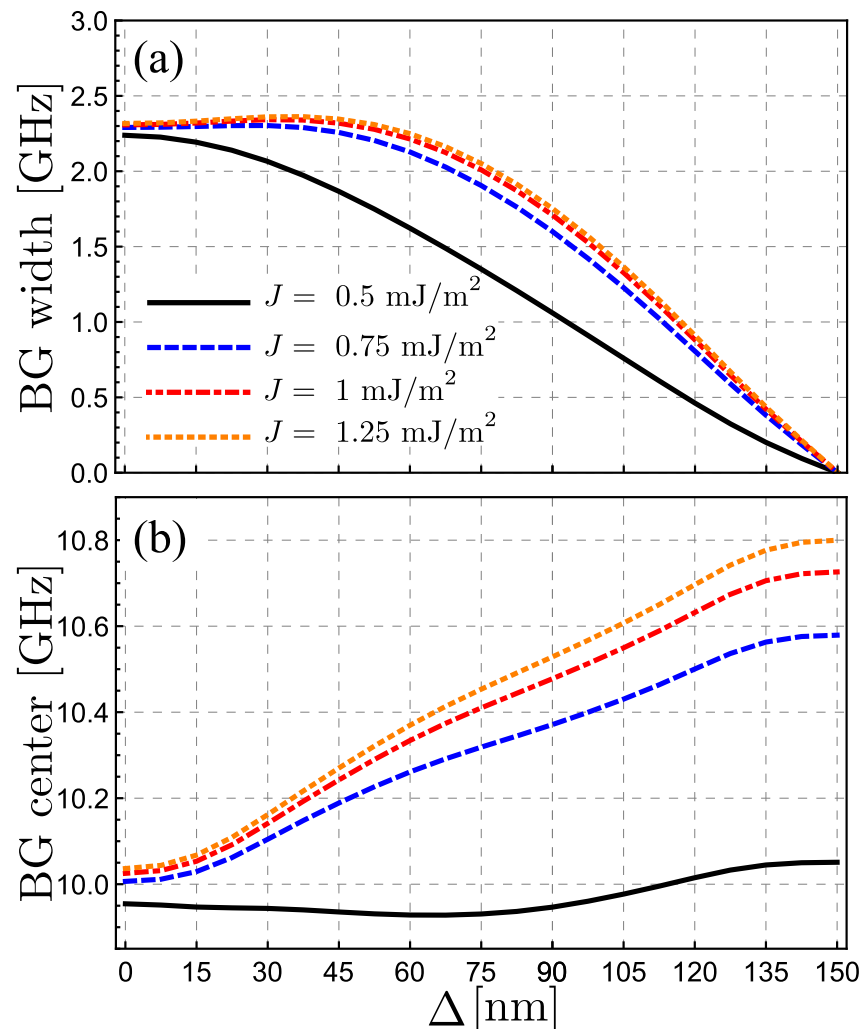


Fig. 4.13: Width (a) and center (b) of the first bang gap as a function of Δ for different values of the interlayer exchange constant.

thickness become narrower [Fig. 4.14(b,d,f,h)]. Therefore, the node of Mode II_{min} is shifted to the point that defines the center of the low saturation magnetization part (center of dotted rectangle). At $\Delta = a/2$ (150 nm), there is no area with reduced M_s along the thickness, and hence there is no longer a node. Thus, the standing character of Mode II_{min} is lost as the BG is closed, causing the SWs to propagate. An analogous analysis can be done for Mode I_{max} , for which the node is located in the zone with high M_s along its thickness. Note that at $\Delta = a/2$, Modes I_{max} and II_{min} have the same energy (or frequency) [Fig. 4.12(c,f)]. This behavior is evident from Fig. 4.14(i,j) as the localization of Mode I_{max} of layer 1 (2) is the same as Mode II_{min} in layer 2 (1). The analysis of the second BG becomes complex because there is a hybridization of the in-phase and out-of-phase modes due to the dipolar interaction [see Fig. 4.12(a–c)]. Also, the modes evaluated at the second BG edges [see Fig. 4.12(d–f)] exhibit nodes in both low and high saturation magnetization zones (not shown). Therefore, the previous discussion of the 1st BG width as a function of Δ does not apply for the second BG.

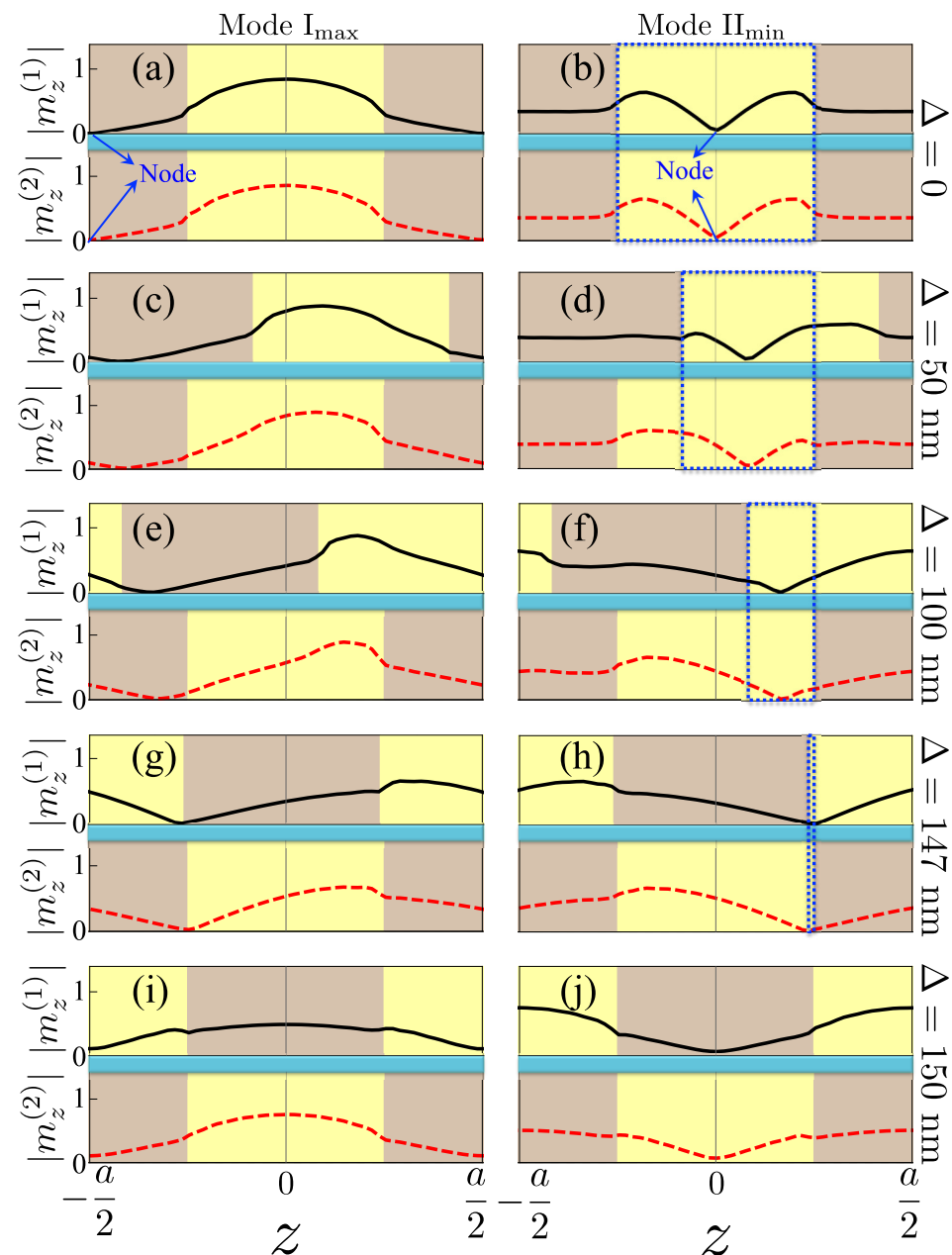


Fig. 4.14: Absolute value of the in-plane SW amplitudes of modes I_{\max} and II_{\min} for different values Δ . In (a), the node is located in the high saturation magnetization zone, whereas in (b), the node is located in the low M_s zone. The dotted rectangles in (b), (d), (f), and (h) outline the zone with low saturation magnetization along the thickness. Dynamic components $m_z^{(\nu)}$ are expressed in arbitrary units.

Conclusions The dynamic magnetic properties of a coupled bilayer MC have been studied. The bilayer MC's band structure exhibits striking features compared to a monolayer MC. The out-of-phase modes induced by the interlayer dipolar interaction emerged above the first BG by reducing the interlayer exchange coupling. Under certain conditions, these high-frequency modes can be flat or non-reciprocal. Interestingly, the collective modes' non-reciprocal properties are preponderant for the high-frequency modes, whereas the fundamental mode remained almost reciprocal. In addition, the band-gap widths can, in various ways, be modulated to

increase in magnitude or decrease to zero. The bilayer MCs can thereby manipulate the propagation of the collective spin waves in several ways and thus are considered excellent candidates in the design of reconfigurable spin-based devices.

4.3 Spin-wave focusing induced by dipole-dipole interaction in synthetic antiferromagnets

DOI

In this section, we use the dynamic matrix method to study the focusing features of the spin-waves induced by the dipole-dipole interaction in synthetic antiferromagnets. With the help of micromagnetic simulations, the focused waves are analyzed in different types of antiferromagnetically coupled bilayers. First, the antiparallel state is induced by introducing a non-magnetic layer providing a negative interlayer exchange constant. Then, the antiparallel state of the bilayer is stabilized through an exchange bias coupling, where a unidirectional anisotropy is induced by the interaction between the ferromagnet and an antiferromagnetic layer. Finally, the spin-wave dispersion and focusing properties of a magnetization-graded synthetic antiferromagnet are discussed.

To systematically study the band structure of a synthetic antiferromagnet, we will use the standard values for Permalloy and Cobalt. Specifically, the saturation magnetization of Py is $M_s^{\text{Py}} = 800$ kA/m, while the exchange constant $A_{\text{ex}}^{\text{Py}} = 7.5$ pJ/m. [155] For Cobalt the saturation magnetization and the exchange constant, respectively, are $M_s^{\text{Co}} = 1400$ kA/m and $A_{\text{ex}}^{\text{Co}} = 28$ pJ/m. [156] We use an effective gyromagnetic ratio $\gamma = 0.01856$ GHz/G for both materials, while the thickness of the non-magnetic spacer is $s = 1$ nm. We will use an interlayer exchange constant of $J_{\text{inter}} = -0.1$ mJ/m² that favors an antiparallel state of the magnetizations. Note that such an antiparallel equilibrium state can be stabilized at small external fields (even at zero field); therefore, in what follows, a small field of 2 mT will be used. Also, to consider the dynamic evolution of the magnetization along the thickness,

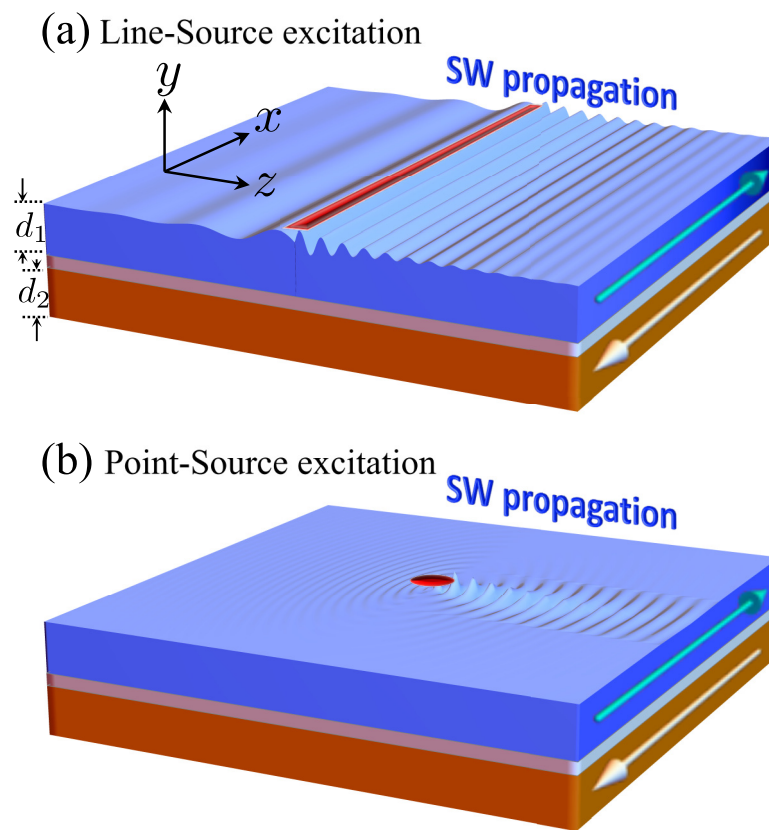


Fig. 4.15: Schematic representation of the spin-wave propagation in a synthetic antiferromagnet. Magnetization of the upper layer points along $+x$, while the magnetization of the bottom layer is oriented along $-x$. In (a), the SW propagation is excited utilizing an external line source, while in (b), a point-source excitation is applied. For case (b), the highly focused SWs generated by the non-reciprocal properties of the spin waves are schematically represented.

the number of divisions used is $N = 26$. Because we want to enhance the non-reciprocal properties of the system, we will consider that the magnetizations are always in-plane.

Spin-wave dispersion and iso-frequency curves Figs. 4.16(a), 4.16(b) and 4.16(c) shows the dispersion of the SWs for $d_{1,2} = 2, 12$ and 24 nm, respectively. In such dispersions, the SWs are propagating along the z -axis, while the magnetizations of both layers are pointing along $+x$ and $-x$ (see Fig. 4.15). We note that the spin-wave dispersion becomes asymmetric when the thicknesses of the magnetic layers increase at moderated wave vectors ($k < 20$ rad/ μm), which is correlated with the dipolar interaction that also increases with the thickness and, at the same time, induces the non-reciprocity in the SW propagation[42], [50] (such wave vector range can be probed by inelastic Brillouin light scattering experiments). When both layers are in an antiparallel state, there is a propagation sense where

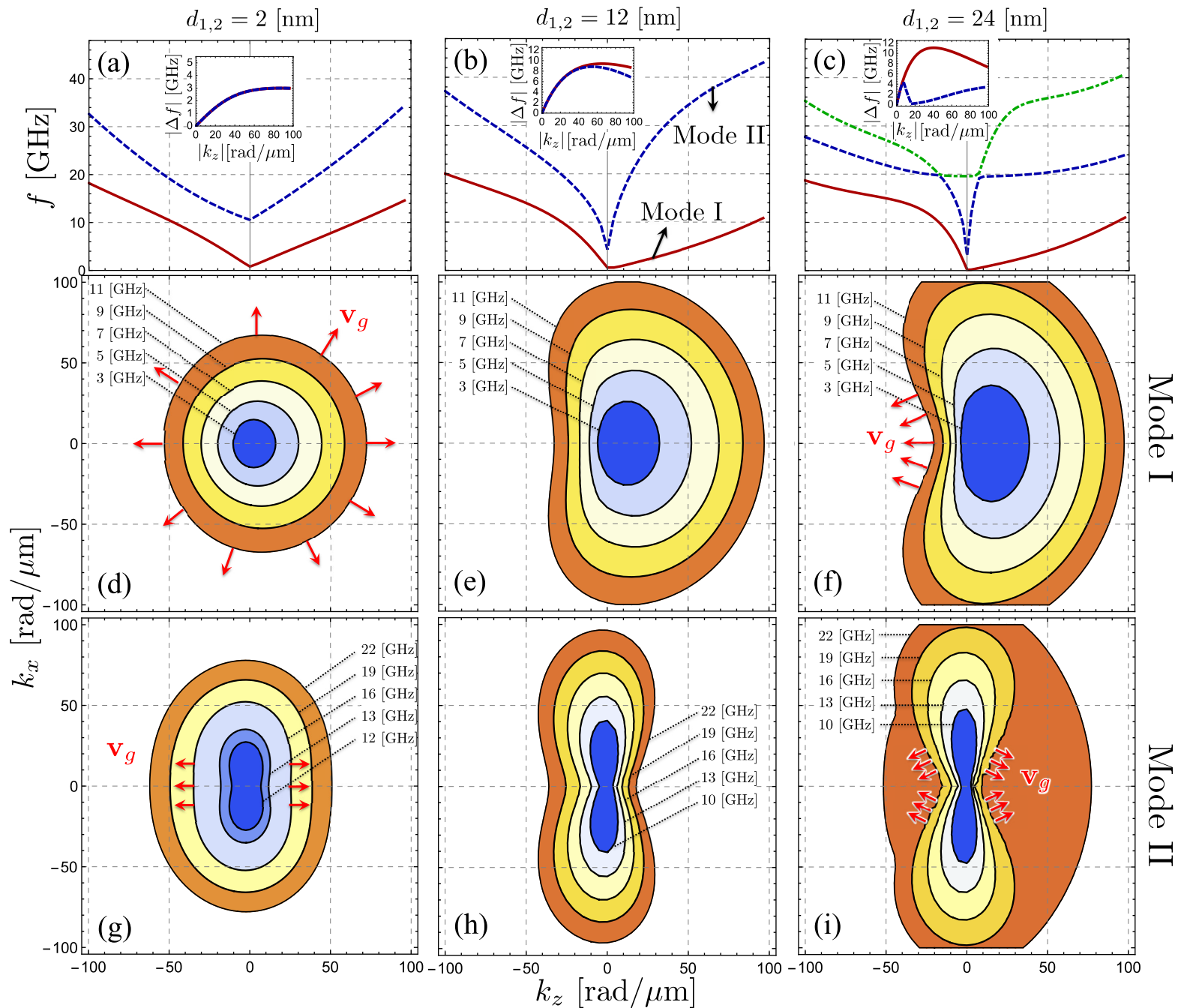


Fig. 4.16: Figures (a)–(c) shows the dispersion relation of the spin waves for synthetic antiferromagnets with different thicknesses, while the insets depict the frequency non-reciprocity Δf as a function of the wave vector for the first two modes labeled as Mode I and II. Figures (d)–(i) show a contour plot generated at a fixed frequency in k -space of Mode I [(d)–(f)] and Mode II [(g)–(i)]. In these figures, the red arrows (that are included by hand) illustrate the orientation of the group velocity (\mathbf{v}_g) of the spin waves.

the dynamic stray fields induced by layer 1 (2) are disposed so that they are always parallel to the local dynamic magnetization of layer 2 (1). Thus, the dynamic dipolar interaction is considerably reduced (and consequently, the frequency is reduced) when the wave propagates in some particular direction.[42] To analyze the propagation in all directions, we have generated a contour plot in k -space at fixed frequencies (isofrequency curves). Figs. 4.16(d)–(f) show the isofrequency

curves (also called slowness surfaces) for the low-frequency mode (Mode I) are depicted as a function of the in-plane wave vector, where the group velocity vector v_g is denoted by the red arrows that are normal to the isofrequency curves.

Due to the degrees of freedom of the magnetization dynamics in a bilayer system, at least two modes with different oscillation phases can be excited. Furthermore, if the thicknesses of the FM layers increases, several higher modes can be observed at low frequencies, since as the thickness increases, the dynamical energy (or frequency) of such modes is reduced. Fig. 4.16(c) shows the case where three modes are observed between the range of 0 - 50 GHz. Nevertheless, for the sake of simplicity, we will focus on the first two low-frequency modes. In Figs. 4.16(g)–(i), we can see the evolution of the isofrequency curves for Mode II at different film thicknesses. Here, in comparison with Mode I, we can see that the focusing properties of the spin-wave propagation are entirely different. In Fig. 4.16(g), we observe highly focused waves that result from the flattening on the left and right parts of the slowness surfaces (see red arrows in the isofrequency curves evaluated at 16 GHz) and propagate in both $+z$ and $-z$ directions. As the thickness increases, interference patterns can be induced along both directions [see red arrows in Fig. 4.16(i)]. The notorious change in the curve evaluated at $f = 22$ GHz [in Fig. 4.16 (i)] occurs since Mode II hybridizes with the next high-frequency mode so that a drastic change of the dispersion and phase occurs. This effect is also observed in the frequency shift Δf , shown in the inset of Fig. 4.16(c), where at about $k = 9$ rad/ μm the frequency shift of Mode II is drastically reduced.

According to the behavior observed for the isofrequency curves of Mode I, it is clear that such curves are very similar to the one obtained in heavy-metal/ferromagnet alloys, where the interfacial DM interaction induces unidirectional caustic beams in the Damon-Eshbach geometry.[17], [77] The case illustrated in Fig. 4.16(d), for instance, is similar to the one with a small Dzyaloshinskii-Moriya constant (D), while the case shown in Fig. 4.16(f) is following larger values of the DM strength. Despite these similarities, both systems present notable differences. For instance, synthetic antiferromagnets are not restricted to ultrathin films (as in heavy-metal/ferromagnet alloys). Indeed, non-reciprocal and focusing properties are enhanced when the thickness increases. Also, because several paths can reach the antiferromagnetic state, there are varied alternatives to manipulate the focalization

of the spin waves. In this sense, it is feasible to cancel the focalization of the waves just changing the magnitude of the external field since the bilayer becomes parallel at high fields, and then, the system loses the non-reciprocal properties. An exciting aspect of our system is that the unidirectional steering of the waves is achieved mainly for the low-frequency mode since the high-frequency one presents focalized propagation of waves in both directions ($+z$ and $-z$). However, this focalization of the high-frequency modes is not a trivial result, since even when the frequency shift Δf is similar in magnitude [see insets in Figs. 4.16(a) and (b)], the focusing properties have different characteristics.

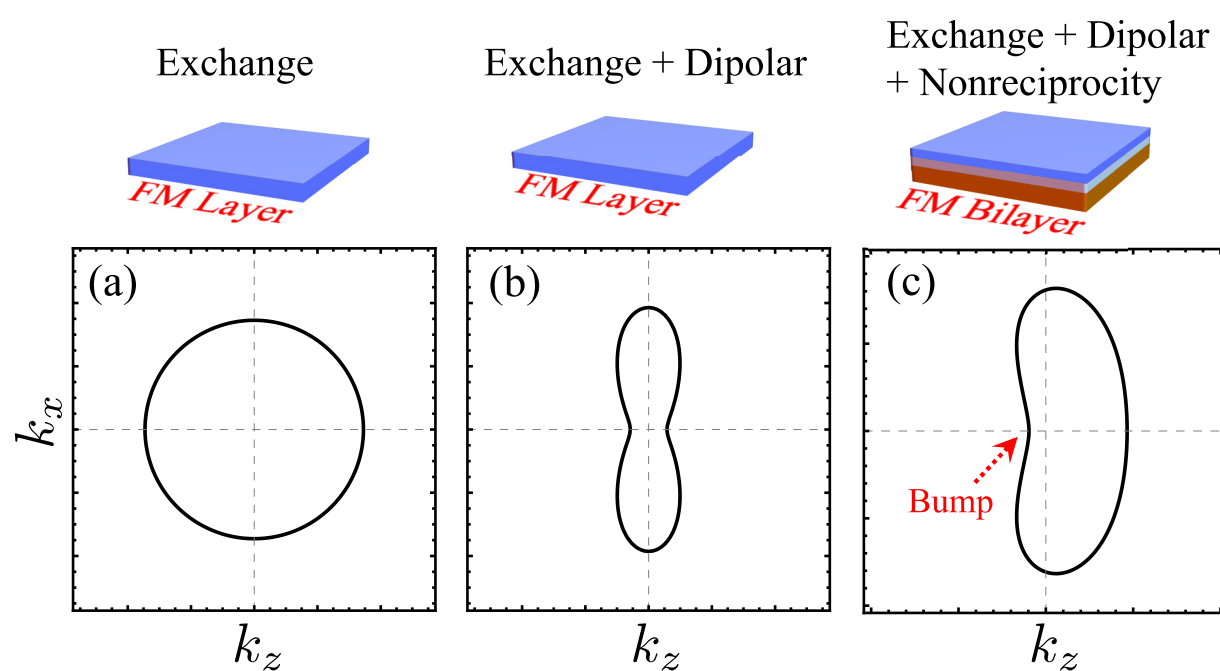


Fig. 4.17: Schematic representation of the isofrequency curves for a single FM layer when (a) only exchange and (b) exchange plus dipolar interaction are active. In case (c), the isofrequency curve is depicted for an antiferromagnetically coupled bilayer, where the dynamic dipolar coupling induces non-reciprocity in frequency.

To understand the formation of highly focused spin waves, we will analyze the main interactions that control the magnonic dispersion. In one isolated ferromagnetic layer where the exchange interaction dominates, the isofrequency curves will be a circle (frequency is proportional to k^2), so that the curvature is constant. Consequently, the energy propagates homogeneously in all in-plane directions [see Fig. 4.17(a)]. When the dipolar interaction is active, backward volume and Damon Eshbach modes (wave vector parallel and perpendicular to the magnetization, respectively) have different features, and the isofrequency curve presents a variable curvature, as shown Fig. 4.17(b). In such a case, caustic waves may appear, where the highly focused waves propagate reciprocally.[11], [157], [158] Instead, in a syn-

thetic antiferromagnet, the dynamic dipolar interaction induces different dispersion properties for BV and DE modes and also induces non-reciprocity in frequency.[42] Such non-reciprocity implies a distortion in the shape of the isofrequency curve, where (under a significant non-reciprocity) the part with the lowest wave-vector magnitude will look like a bump, as shown in Fig. 4.17(c). The critical point now is that the part with the bump entails a change of sign in the curvature so that there are some regions where the curvature will be zero, and therefore non-reciprocal caustic waves are formed. Thus, the strongly anisotropic dispersion induced by the dipolar interaction in a synthetic antiferromagnet can be helpful to steer spin waves, allowing a concentration of the energy. Also, since a synthetic ferromagnet can be stabilized in varied ways, there are many degrees of freedom to control the causticity and the focusing of the spin waves.

In Fig. 4.16 we analyzed the antiparallel configuration stabilized by a negative interlayer exchange constant. Nonetheless, such an antiferromagnetic state can be stabilized by other means. The following example will analyze the focusing properties when the antiferromagnetic state is reached by coupling an FM layer (Co) with an antiferromagnetic (AFM) film. In Fig. 4.18(a), a schematic representation of the system is shown, where the Co layer is pinned along $-x$, via an exchange bias field $\mu_0 H_{EB} = 15$ mT, while the Cobalt and Permalloy films are coupled through an interlayer exchange $J_{inter} = 0.001$ mJ/m², so that the Py layer is almost free. Note that in this case, the interlayer exchange coupling is very different in comparison with the structure shown in Fig. 4.16, since here the system does not require a negative (and strong) J_{inter} to reach the antiferromagnetic state. Namely, even at $J_{inter} = 0$, the bilayer will be in an antiferromagnetic state for small external fields. In small fields, the magnetizations of both layers are pointing along $-x$, while for high values of the external field, both magnetizations can follow the field direction ($+x$). In the intermediate case ($\mu_0 H = 2$ mT), the upper layer of Permalloy can follow the field (which is applied to $+x$), while the Co layer remains pinned along $-x$. Thus, an antiparallel alignment of the magnetizations is reached for this system. Figs. 4.18(b)–(d) shows the isofrequency curves of the first Mode at three different thicknesses and evaluated at $\mu_0 H = 2$ mT. For simplicity, we show only the low-frequency mode since the second mode (not shown) exhibits similar properties in comparison with the case illustrated in Fig. 4.16. Here, we can see that the evolution of the curves is different in comparison with the system studied

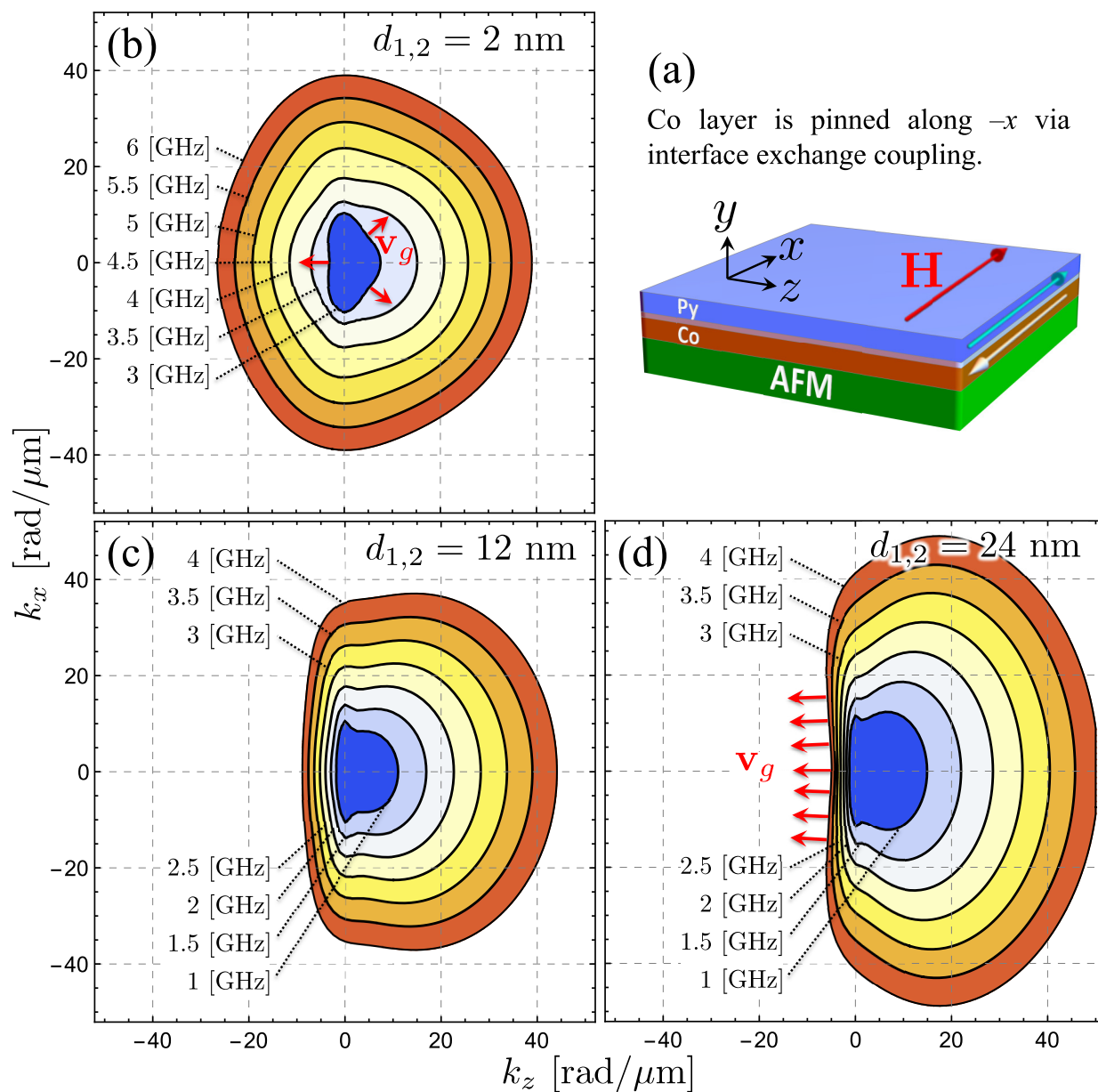


Fig. 4.18: In (a), the schematic representation of the system is shown. The external field is applied along $+x$ so that the Py layer is also oriented along $+x$, while the Co layer is pinned along $-x$ due to the exchange-bias coupling at the FM/AFM interface. In (b), (c) and (d) the isofrequency curves for $d_{1,2} = 2$ nm, 12 nm and 24 nm are depicted, respectively.

in Fig. 4.16. At small thicknesses, the isofrequency curve at 3 GHz exhibits three zones with slight curvatures [see red arrows of the group velocity in Fig. 4.18(b)] so that we can predict three focalized waves. These focusing effects change as the frequency increases since the isofrequency curves do not have a range of wave vectors with small curvatures at significant frequencies (higher than 6 GHz). Interestingly, at larger thicknesses, the unidirectional propagation of the focused waves is allowed and slightly varies as the frequency increases [see Figs. 4.18(c) and (d)]. In Figs. 4.18(d), the direction of the group velocity is highlighted, where

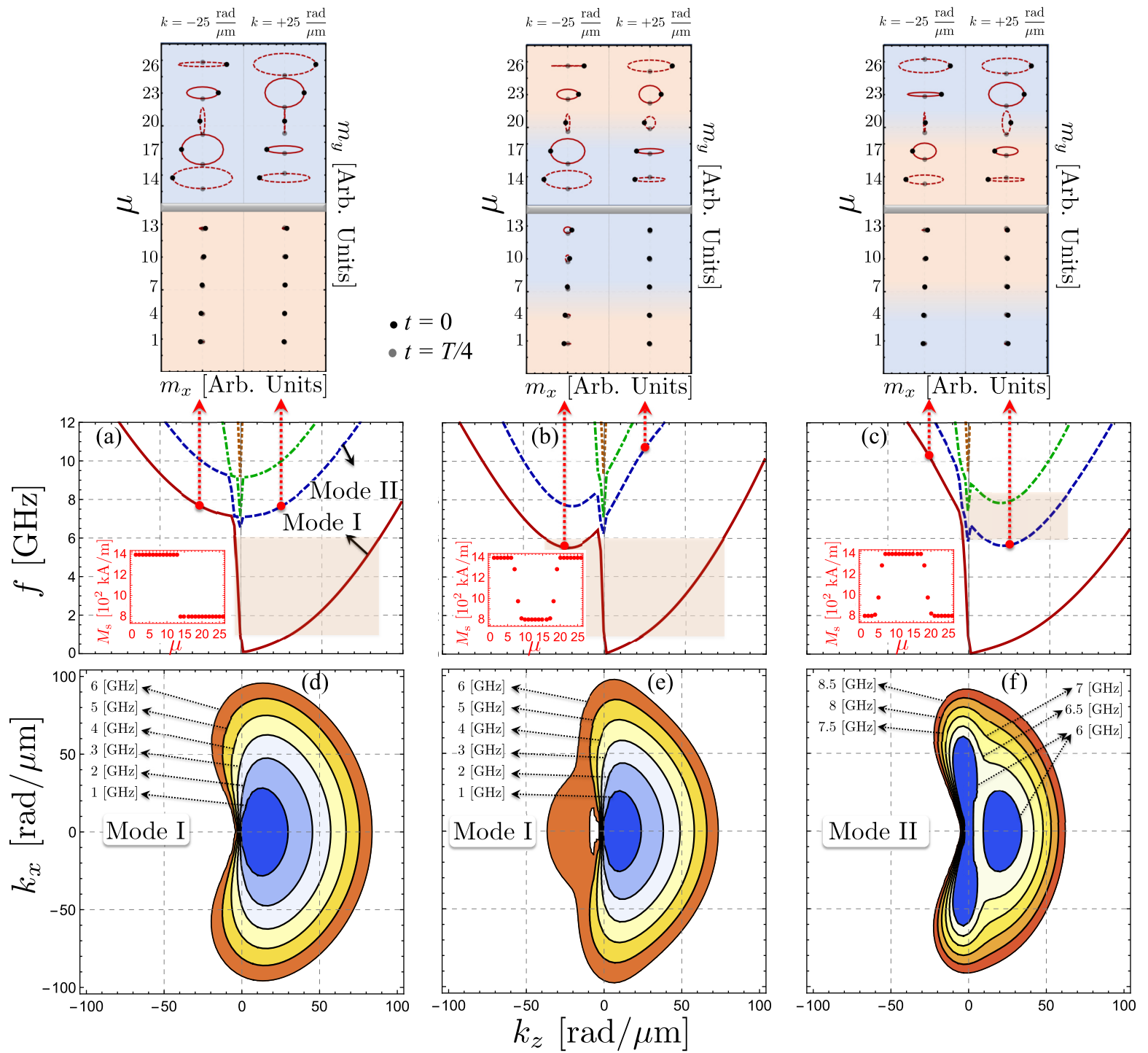


Fig. 4.19: In figure (a), the dispersion relation of a typical bilayer Co/NM/Py system is shown, while in (b) and (c), the dispersion of a bilayer with the graduation of the saturation magnetization is depicted. The insets in (a)–(c) illustrate the saturation magnetization as a function of the thickness. Upper plots illustrate the SW profiles calculated at $k = \pm 25 \text{ rad}/\mu\text{m}$. In (d) and (e), the iso-frequencies of Mode I are shown, while in (f) the iso-frequencies curves are given for Mode II. The shaded areas in (a)–(c) illustrate the range of frequencies used to calculate the isofrequency curves in (d)–(f). The thickness of both the Co and Py layer is 60 nm, where each FM layer has been divided into 13 sublayers.

Magnetization-graded synthetic antiferromagnets Finally, we will consider a more particular case, where both FM layers' saturation magnetization will be graduated to modify the non-reciprocity of the spin waves and their respective focalization properties. Here, to enhance the effect of the magnetic graduation, each FM film has a thickness of 60 nm. Fig. 4.19 illustrates three different cases where the saturation magnetization varies across the thickness of the entire structure. Sublayers between $n = 1$ and 13 correspond to the bottom layer, while the sublayers labeled between $n = 14$ and 26 correspond to the upper layer. For the case without graduation, where M_s changes abruptly between two values [Fig. 4.19(a)], one can appreciate a notable non-reciprocity of the fundamental mode (Mode I), while the upper-frequency modes have almost symmetric dispersion. An exciting aspect of the thick bilayer systems is the wide range of frequencies (0-6 GHz) where the SWs have a large group velocity at negative wave vectors, and such behavior is enhanced as the thicknesses increase.[4] Note that the magnitude of the spin-wave group velocity is about 7 km/s in the range of frequency between 0-7 GHz, which is connected with the strong non-reciprocity induced by dipolar interaction in thick films. Such order of magnitude has been previously reported in magnetic systems.[159], [160] By analyzing the SW profiles (upper plots of Fig. 4.19), we can establish that in Fig. 4.19(a) the second mode (and some of the other high-frequency modes) corresponds to an excitation of the upper FM layer. Therefore, such mode has the same energy for the two counterpropagating waves, since if the excitation is given only in one FM layer, the symmetry along the thickness is not broken, and therefore SWs propagating along $+z$ and $-z$ have the same dynamic energy or frequency. Now, under a different profile of variation of the saturation magnetization [see Figs. 4.19(b) and (c)], the dispersion is not significantly modified at frequencies lower than 5 GHz, so that the degree of the SW focalization of the fundamental mode is similar either with or without graduation of M_s . Nevertheless, the high-frequency modes are modified since they are non-reciprocal when the saturation magnetization varies along the thickness. Because the mode is mainly excited in one layer, it is expected that the variation of M_s induces non-reciprocity of the SWs since now the symmetry is broken along the thickness where the amplitude of the magnetization oscillations is remarkable. Figs. 4.19(d) and (e) depict the isofrequency curves of Mode I. Here, we see that Mode I has similar focalization characteristics at low frequencies (lower than 5 GHz), even when the saturation magnetization

has been varied across the thickness. This behavior is in concordance with the slight modification of the non-reciprocal properties of Mode I. Nevertheless, the isofrequency curves change at high frequencies because the second mode reduces its frequency at $+k$ or $-k$ depending on the type of gradation. This effect is observed in Fig. 4.19(e), where at 6 GHz the isofrequency curve is modified at negative wave vectors since the fundamental mode hybridizes with Mode II. The isofrequency curves of Mode II are shown in Fig. 4.19(f), where one can see that the non-reciprocity of the mode strongly influences its focusing properties. For instance, at 6 GHz, the curves depicted for Mode II indicate that it is possible to create non-trivial interference patterns since spin waves with different wavelengths are propagating at the same frequency.[77] It is worth mentioning that the results presented in Fig. 4.19 are not notoriously modified if the magnetization profile change abruptly or gradually (not shown). Namely, if a gradual (abrupt) magnetization change is considered in Fig. 4.19(a) [Figs. 4.19(b) and (c)], the SW dispersion does not significantly change, unless the magnetization gradation is extended along the whole thickness.

Overall, it is observed that magnetic gradation can be an essential ingredient in controlling the spin-waves focalization. In realistic materials, such magnetic gradation can be implemented in multilayered structures,[113], [114], [161]–[165] in which extended interfaces are created by either directly tuning the thicknesses of the magnetic layers[114], [162], [163] or by interdiffusion via heat-treatment.[113], [161], [164], [165] Also, over the last few years, the realization of vertically graded thin films has been achieved in epitaxial compositionally graded alloy films, where gradation of the exchange strength,[116] and saturation magnetization[110] can be induced along the thickness. Here, the depositions are performed at room temperature by sputtering deposition,[110], [116], [166] while the graded layers are fabricated by co-sputtering, keeping the power of one material fixed while changing that of the other to achieve the intended composition profile.[110], [116], [166]

Conclusions We have theoretically addressed the focusing spin-wave properties for synthetic antiferromagnets. By analyzing the isofrequency curves, we have observed that the bilayer systems show a focalized spin-wave propagation when such waves are excited by a single point source. We have also analyzed the role of

magnetic layer thicknesses and magnetic grading on focusing properties, and, as a general result, we have seen that the focalization characteristics of the fundamental and high-frequency modes are entirely different. Depending on the frequency range, it is possible to create highly-focused spin waves where the low-frequency mode only influences the focalization properties. In contrast, the focusing properties of the high-frequency modes are a superposition of more than one mode, exhibiting thus a more complex propagation. Finally, we can conclude that bilayer systems are excellent candidates for inducing and controlling highly focused spin waves and non-reciprocal interference patterns, which are essential for a new generation of magnonic devices such as demultiplexers, circulators, and isolators.

4.4 Propagation of localized spin-wave modes within magnetization-graded stripes

This section studies the localized propagation of spin-waves in magnetization-graded ferromagnetic (FM) stripes. Here, we employ the dynamic matrix method in such a way that the stripe system is divided into many coupled small strips. Therefore, it turns out to be trivial to incorporate graduation of magnetic properties along the stripe width, which allows us to analyze the influence of the graduation on the localization of the spin waves. The system under consideration is shown in Fig. 4.20. Here, we highlight the geometrical properties [see Fig. 4.20(a)] and the use of the DMM in Fig. 4.20(b).

Like the previous sections, typical values for Permalloy (Py: $\text{Ni}_{80}\text{Fe}_{20}$) will be used. Namely, the saturation magnetization of Py is $M_s^{\text{Py}} = 800$ kA/m, while the exchange constant $A_{\text{ex}}^{\text{Py}} = 9.9$ pJ/m. Also, the gyromagnetic ratio is $\gamma = 185.66$ GHz/T, and the stripe thickness is $d = 1$ nm. Regarding the discretization of the ferromagnetic stripe, such a system is divided into small sub-strips so that $b = 4$ nm. This size is less than the exchange length ($\ell_{\text{ex}} = 4.96$ nm), which is also verified utilizing a convergence test. Namely, if $b < 4$ nm the SW spectra do not notoriously change.

The transition from a stripe to a thin film is first studied to identify the nature of the calculated spin-wave modes. For this purpose, a bias field of $H = 300$ mT is

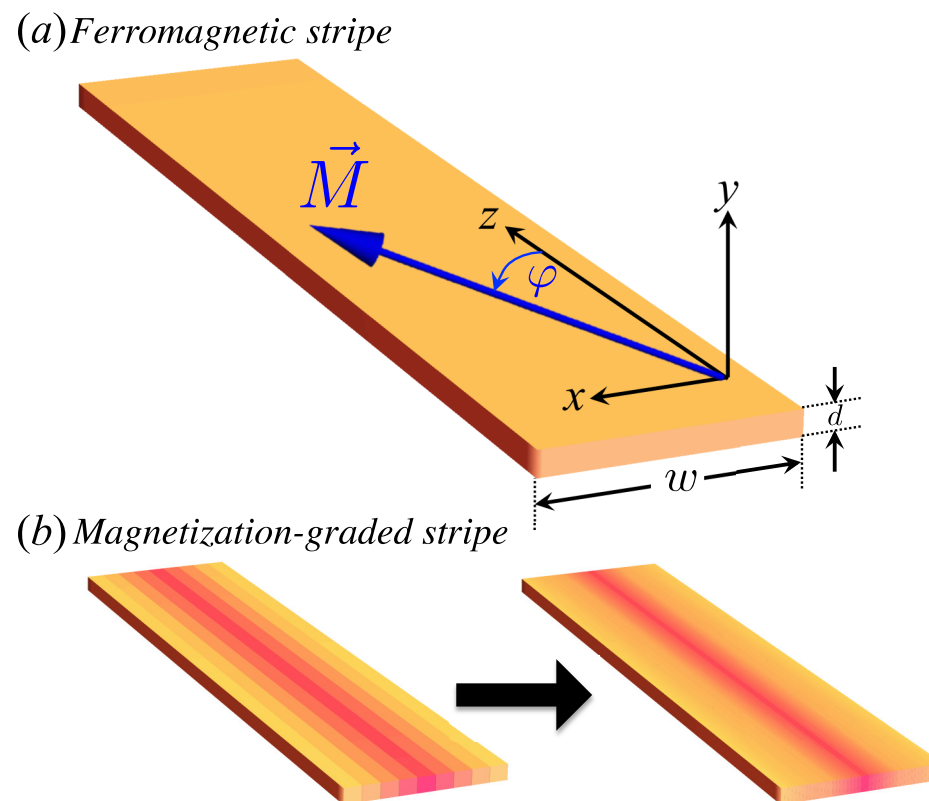


Fig. 4.20: (a) Illustration of the coordinate system and the main geometrical parameters of a magnetic stripe. Figure (b) shows a schematic representation of the dynamic matrix approach, where the system is divided into many sub-stripes, which allow to include magnetic graduation along the width. The color graduation represents the variation of the magnetic properties along the stripe width.

applied along the x axis, while the spin waves propagate along z . The idea here is to study the so-called Damon-Eshbach configuration ($\mathbf{M} \perp \mathbf{k}$), for which the modes can effectively exhibit a notable localization in some zones of the stripe width. In backward-volume configuration ($\mathbf{M} \parallel \mathbf{k}$) instead, the modes do not present a significant localization, even if there is magnetic graduation along the stripe width. Therefore, in what follows, the equilibrium magnetization is always pointing along x ($\varphi = \pi/2$), while the propagation is along the long stripe axis z . Open circles in Figs. 4.21(a)–(d) describe the SW dispersion of a thin film, while lines correspond to the modes of the FM stripe, for which the first five low-frequency modes are plotted. By analyzing the spin-wave profile across the width (upper 3D plots of Fig. 4.21), it is observed that the magnetic excitations depicted in Fig. 4.21(a) correspond to edge modes (labeled as EM1 and EM2), which are not degenerate at small widths. One can note that EM1 and EM2 have in-phase and out-of-phase characteristics, respectively. Similar to the perpendicular standing spin-wave modes in a thick FM film, the out-of-phase mode presents higher dynamical energy than the in-phase one, which is correlated with the dynamic exchange interaction between the magnetic

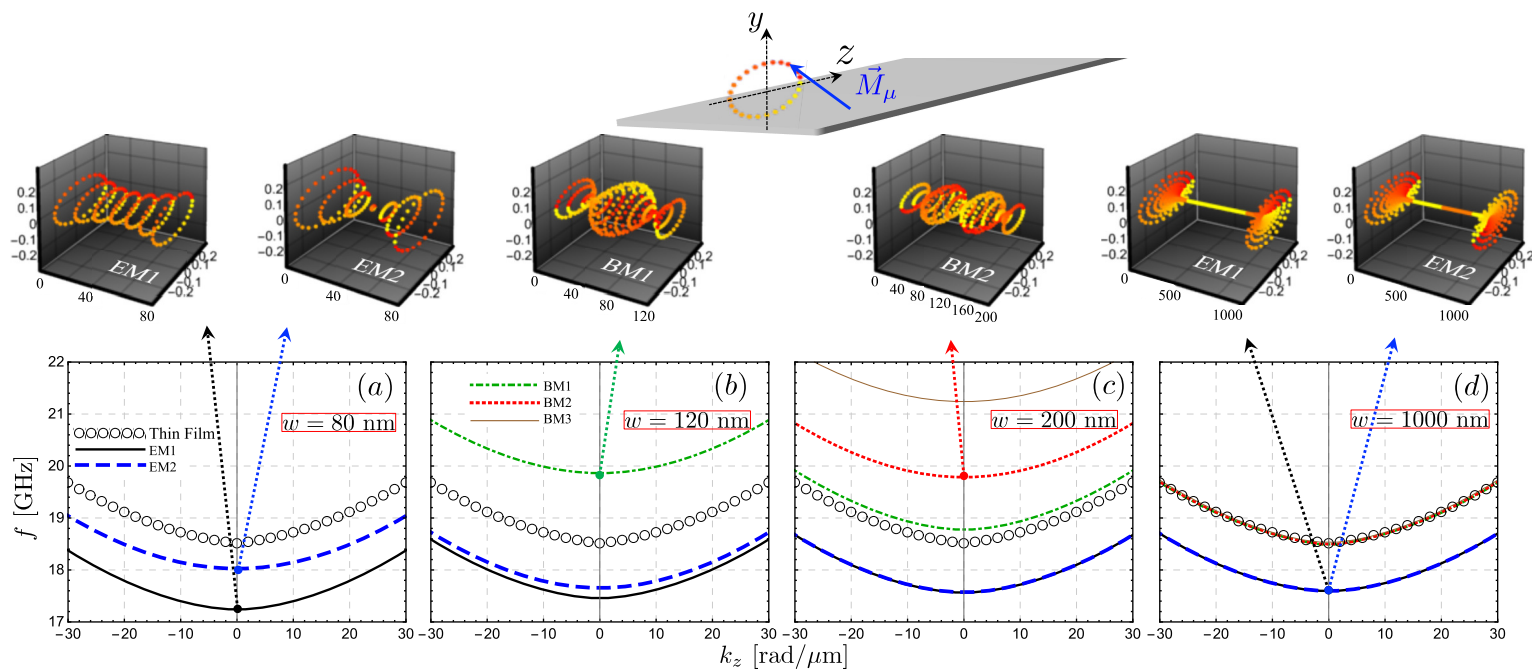


Fig. 4.21: Figures (a)–(d) shows the dispersion relation of the spin waves for a stripe with different widths w . Open circles show the SW dispersion of an FM thin film, while the lines are the modes of a magnetic stripe. To illustrate the bandstructure of the stripe system, the first five modes have been considered. Upper 3D graphics correspond to the spin-wave profiles along the width for zero wave vector, where the dynamic magnetization components are calculated in arbitrary units. EM and BM are referred to as edge and bulk modes, respectively.

moments. As the width increases, however, the modes become degenerate since the exchange energy of mode EM2 is reduced. Thus, both edge modes have the same frequency for wider stripes since they are too far away from each other [see Figs. 4.21(c) and (d)]. These low-frequency edge modes are associated with the reduction of the internal field at the edges of the stripe since the surface magnetic charges generate a demagnetizing field that is strong at the edges and opposite to the external field. Therefore, the internal field (external field minus demagnetizing field) is reduced in magnitude at the stripe edges, allowing thus the excitation of low-frequency modes in such zones. If the stripe width increases, the higher-frequency modes are observed in the frequency range shown in Fig. 4.21. Here, the third bulk mode (BM1) is localized mainly in the stripe center [see upper profile in Fig. 4.21(b)] so that as the stripes' width increases, such a mode should match with the one of an FM film. This behavior is clearly observed in Figs. 4.21(d), where at $w = 1000$ nm, the third (BM1), fourth (BM2), and fifth (BM3) modes match with the thin-film mode. This matching of the modes is an expected behavior since the mode quantization due to the geometrical confinement becomes irrelevant

for large values of w . In fact, in a standard physical picture, the bulk standing SW modes in a magnetic stripe exhibit different frequencies due to term of the type $k_{\perp} = n\pi/w_{\text{eff}}$, [167] where k_{\perp} is the quantized wave vector along the stripe width, and w_{eff} is an effective stripe width (proportional to w) that considers the dipolar boundary conditions at the stripe edges. Thus, upon increasing w , the term $k_{\perp} = n\pi/w_{\text{eff}}$ tends to zero, and all standing waves are excited close to the $n = 0$ mode, which corresponds to the mode of the infinite film.

The results presented in Fig. 4.21 confirm the validity of the theoretical method, where edge and bulk modes have been identified, connecting the bulk modes with the one of an FM thin film. Furthermore, due to the reduction of the internal field at the rim of the stripe, low-frequency edge modes are excited, while the high-frequency ones present non-zero amplitude oscillation in both the center and edges of the FM stripe. The idea is to change the magnetic properties along the stripe width to obtain a localized propagation of spin waves. Note that the edge modes already provide a scenario for localized propagation due to a locally reduced internal field. Nonetheless, creating a sample with perfect edges is not a simple task. Such edges typically present an unavoidable roughness or defects that can prevent the natural behavior of the spin waves traveling in such zones. Another option mentioned already above is to induce domain walls, where such walls allow to induce channeled SWs within the domain walls. [13] However, domain walls strongly depend on the material and are not robust against external magnetic fields. Besides, due to the nature of the formation of the walls, it is not easy to modify its shape, for instance, to bend the wall in arbitrary directions. Therefore, alternative ways to channel the SWs are of interest, and, in this context, magnetic gradation is proposed as a potential alternative for creating a localized propagation of waves. More precisely, the influence of magnetization gradation along the stripe width on the mode profiles will be studied. Besides the principle feasibility of this route, an immediate question is to how large extent the magnetic modulation has to be chosen to create a notable SW localization? That question will be addressed in what follows.

Fig. 4.22 shows the case where the saturation magnetization presents a non-monotonic profile along the stripe width (for the case of $w = 200$ nm), with a M_s reduction in the central part [see Fig. 4.22(b)]. The fractional reduction of the

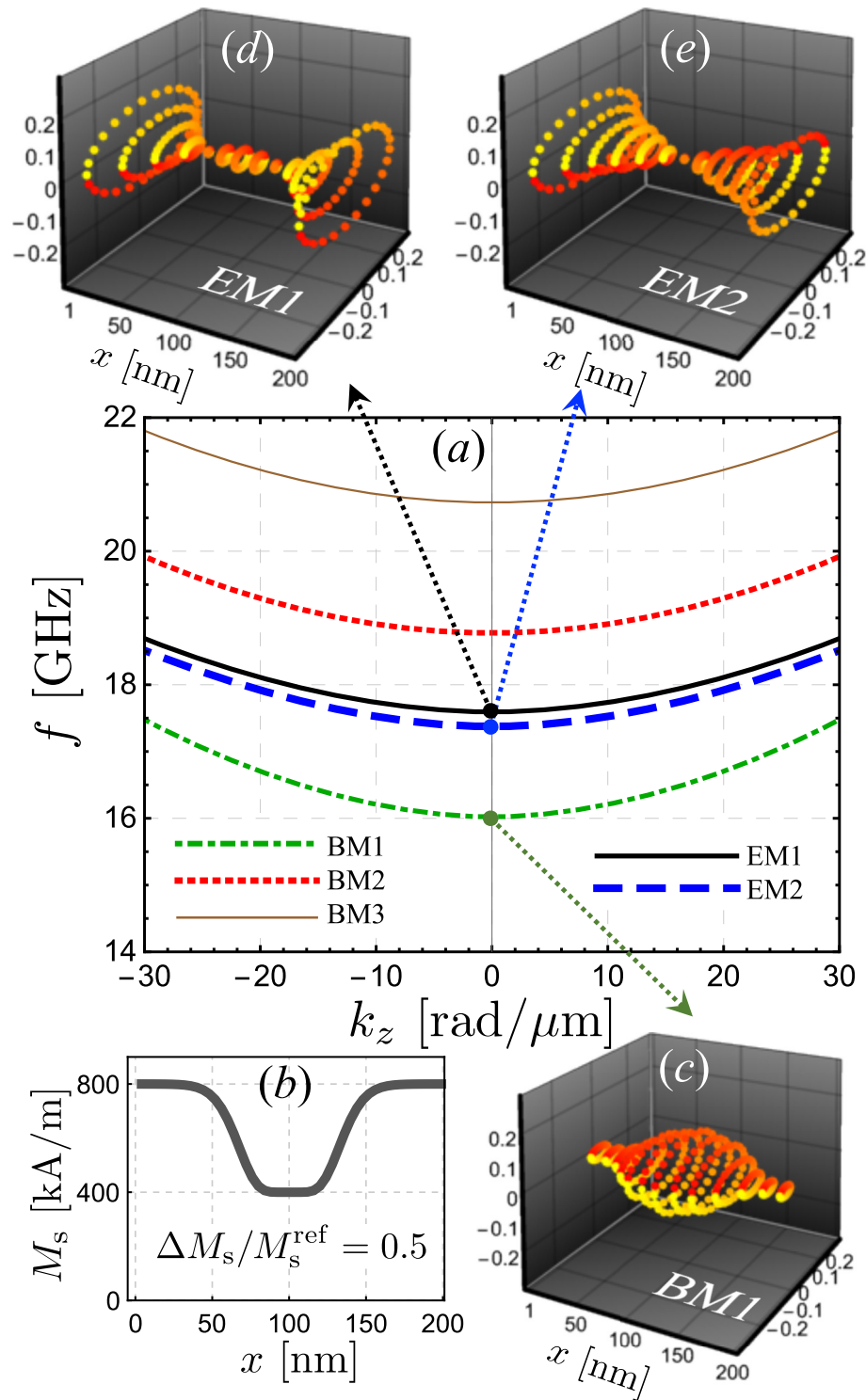


Fig. 4.22: SW spectra of a magnetized-graded stripe. In (a) the spin-wave dispersion is shown, where the bulk mode BM1 is the lowest-frequency mode. Figure (b) shows the saturation magnetization profile, where a reduction of M_s is included. Figures (c), (d) and (e) depict the SW profiles along the stripe width for modes BM1, EM1 and EM2; respectively. Dynamic magnetization components m_z and m_y are calculated in arbitrary units.

saturation magnetization is given by $\Delta M_s / M_s^{\text{ref}} = 0.5$ (50%), where M_s^{ref} is the reference value of the saturation magnetization of Py (800 kA/m), while ΔM_s corresponds to M_s^{ref} minus the value of saturation magnetization evaluated at the center of the stripe. Overall, the SW bandstructure is notably modified in the presence

of such magnetization profile as shown Fig. 4.22(a). Indeed, the frequency of the bulk modes is reduced, which is connected with the decrease of the saturation magnetization at the stripe center. Band BM1 corresponds to the low-frequency mode, which has a pronounced localization at the stripe center as shown by Fig. 4.22(c). The edge modes are slightly modified, and now EM1 is excited at less frequency than mode EM2. In Figs. 4.22(d) and (e), it is observed that EM1 has a small magnetization oscillation amplitude in the stripe center (zone with reduced M_s), which increases its dynamical energy and, hence, the frequency of EM1 is lower than for EM2. The localization of the mode labeled as BM1 is a remarkable result in Fig. 4.22 since it demonstrates that a localized propagation of SWs is achievable in magnetization-graded FM stripes. Nonetheless, the reduction of a 50% of the saturation magnetization ($\Delta M_s/M_s^{\text{ref}} = 0.5$) is a significant change of magnetic properties. Therefore, it is of interest to investigate what is the M_s reduction required to reach a reasonable localization degree. Fig. 4.23 shows the absolute value of the out-of-plane component of the dynamic magnetization of mode BM1 as a function of x evaluated at $k = 0$. Here, it is possible to see how the SW localization evolves as $\Delta M_s/M_s^{\text{ref}}$ is reduced. Under a reduction of a 30% ($\Delta M_s/M_s^{\text{ref}} = 0.3$), the bulk mode BM1 is still mainly localized within the FM stripe center. Nevertheless, when the reduction is only 20% (or less), the mode is no longer localized in the stripe center. Here, the edge modes dominate (frequency of EM1 and EM2 are comparable with BM1), and consequently, the main oscillation amplitude is given at the stripe edges. Also, the case $\Delta M_s/M_s^{\text{ref}} = 0.2$ depicts a more asymmetric profile along the stripe width (see Fig. 4.23), which is due to the hybridization between bulk mode BM1 and the edges modes. The hybridization, thus, limits the possible localization of SWs within the center of the stripe. Nevertheless, for the small width of 200 nm, the hybridization problem is overcome only via a significant reduction of the saturation magnetization, as shown in Fig. 4.23.

Thus, it is still possible to create localized modes slightly modifying the saturation magnetization (less than 20%).

For the previous system shown in Figs. 4.22 and 4.23, the stripe width is small enough ($w = 200$ nm) to allow the hybridization of bulk mode BM1 with the edge modes. Therefore, in such a case, a significant reduction of the saturation magnetization is needed to localize the first bulk mode, as shown Fig. 4.23. On the

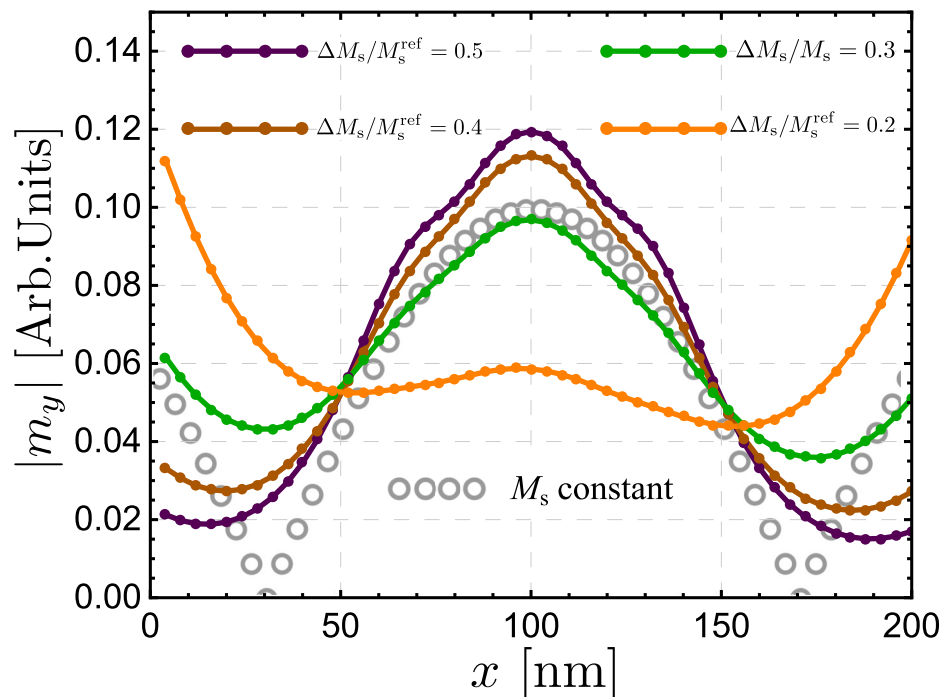


Fig. 4.23: Absolute value of the out-of-plane dynamic component of the magnetization (for mode BM1) as a function of x for different values of the fractional reduction of the saturation magnetization $\Delta M_s/M_s^{\text{ref}}$. Open circles depicts the case of uniform saturation magnetization.

other side, the localization properties of BM1 (evaluated at $k = 0$) are shown in Fig. 4.24, where a wider stripe with $w = 1000$ nm is considered. Here, it is evident that BM1 is channeled around the zone with reduced M_s without the influence of the edge modes. Also, if the magnetization profile of mode BM1 is evaluated at $k \neq 0$, the spatial structure of BM1 along the stripe width remains almost unaltered, so the discussion presented here applies to any wave vector state in the range $|k| < 30$ rad/ μm . The insets of Fig. 4.24 depict the cases where the saturation magnetization is reduced by 15% (left) and 5% (right). Surprisingly, even when the reduction of the saturation magnetization is small, the bulk mode is able to present a notable degree of localization. One may observe in Fig. 4.24 that as M_s decreases, the localization in the center of the stripe is enhanced, while the oscillations outside this center region are more strongly suppressed. As a reference, the case of constant saturation magnetization is shown (see open circles in Fig. 4.24).

It is worth mentioning that the results reported here also apply to thicker stripes ($d \leq 10$ nm), as long as the dynamic magnetization does not vary across the stripe thickness. Namely, the degree of localization of the SW modes in such thicker stripes is similar to the one reported here for ultra-thin stripes. Besides, if the

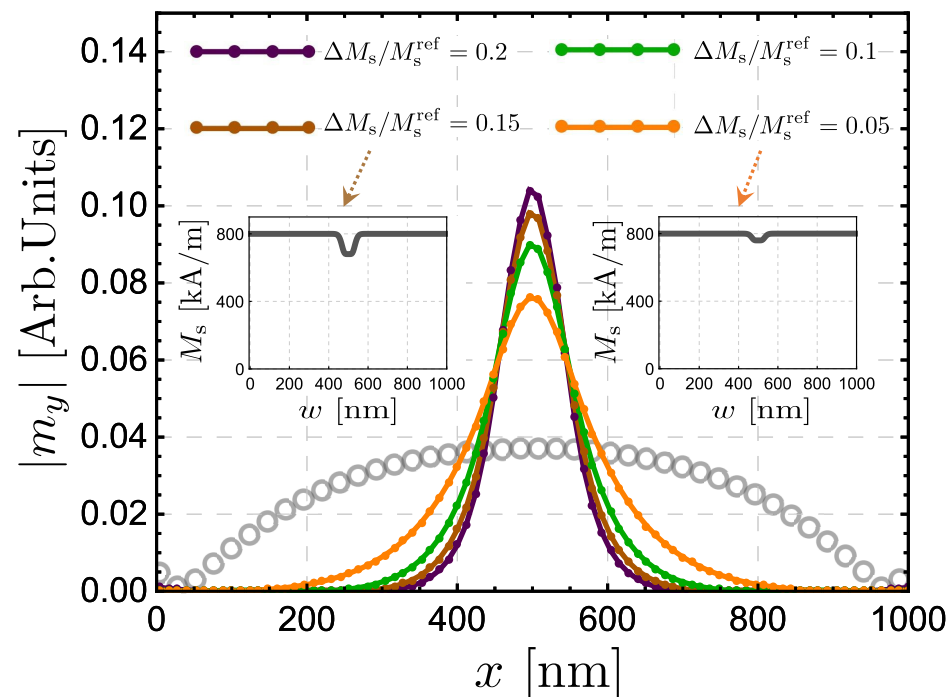


Fig. 4.24: Absolute value of the out-of-plane dynamic component of the magnetization (for mode BM1) as a function of x for different values of the fractional reduction of the saturation magnetization $\Delta M_s/M_s^{\text{ref}}$. The insets show the saturation magnetization profiles for the cases of $\Delta M_s/M_s^{\text{ref}} = 0.15$ (left) and $\Delta M_s/M_s^{\text{ref}} = 0.05$ (right). Open circles depicts the case of uniform saturation magnetization.

graduation position along the stripe width changes, the localization of the magnetic excitations also changes. For instance, if the graduation is active just on one edge of the stripe, a robust localization of an edge mode will be induced in such a graduated part (not shown). However, a real complication in guiding localized edge modes is that they are susceptible to scattering due to roughness or imperfections in the sample. In order to avoid these undesirable effects, it has proposed the use of spin waves with topological properties. In this case, unidirectional modes protected to backscattering can be excited in the interface between two systems characterized by collective excitations with different topologies.[86] On the other hand, the experimental viability to create graduated samples is currently feasible. For instance, the realization of vertical graduation along the thickness in thin films is achieved in epitaxial compositionally graded alloy films by co-sputtering, keeping the power of one material fixed while changing that of the other to achieve the intended composition profile.[110], [116], [166] Combinatorial material deposition can also be employed to fabricate samples with lateral gradients. A review of this method is found in Ref. [168], which typically results, however, in extended thin films. To achieve lateral gradients within single mesoscopic or nanoscopic structures,

lithographic masks can be used to manipulate the structures locally. Such a route was successfully used by co-authors of this paper on FeAl-alloys.[169] A direct way to locally change magnetic properties employing a focused ion beam has been demonstrated in Ref. [170] and Ref. [171], and could be employed similarly to realize the graded structures suggested in this paper.

Conclusions We have theoretically studied the spin-wave spectra of a magnetization-graded ferromagnetic stripe. A localized spin-wave propagation has been obtained by modifying the saturation magnetization along the stripe width. The relation between the fractional decreases of the saturation magnetization and the degree of localization has been explored. It is demonstrated that channeled spin waves can be excited in magnetization-graded ferromagnetic stripes, even when the saturation magnetization is reduced by less than 10%. These results are relevant for future applications associated with magnonic waveguides at the nanometer scale.

Conclusions and Perspectives

Here we distill the main conclusions of this thesis. We have developed and extended a powerful theoretical tool, called the Dynamic Matrix Method, that is able to describe the spin wave dynamics of various extended ferromagnetic nanostructures. The theory is versatile enough to treat multilayered (or striped) ferromagnetic systems in different geometric and coupling configurations, where the individual layers can be thick or thin and uniform, graded or periodic in their magnetic parameters. We have successfully applied the method in thick layers, magnetization-graded layers and stripes, bilayered magnonic crystals, and synthetic antiferromagnets. Due to the semi-analytical character of the theoretical model, the spin-wave dispersion and the dynamic magnetization profiles calculations can be contrasted with readily available analytical expressions that allow interpreting the physical phenomena involved in a much better way. Much of our results have been compared with micromagnetic simulations, where the agreement between both methods has been very good in all cases. Finally, it is worth emphasizing the advantages of the Dynamic Matrix Method with respect to simulations. Even though numerical simulations can be used to reproduce the dynamic properties of the systems discussed in the previous section, in the simulations there is a lack of explanatory power of the physics behind the results (no analytical expression to hold to), without mentioning the notorious computational time required for a systematic exploration of the different magnetic parameters of the system. Thus, the Dynamic Matrix Method allows analyzing the role of the different interactions on the spin-wave dynamics in an easy way since the modification of each interaction can be realized directly. Besides, even when the method studied in this thesis has a numerical character, there are analytical expressions in the calculations that can be used to interpret and understand the physical origin of the results.

These results are not, by any means, the end of the road. There are multiple doors that this thesis leaves open. For starters, the method could be applied as is to study similar ferromagnetic nanostructures, such as magnetization-graded magnonic crystals (layered or striped), where the temporal evolution of the magnetization along the thickness can be studied. Another possibility is extending the method to calculate the spin wave dynamic properties in magnetic textures (e.g. domain walls) or cylindrical nanostructures. In the latter system, the Dynamic Matrix Method can be applied to calculate the spin wave spectra of thick nanotubes, which has not been reported so far. Another line of inquiry contemplates how different boundary conditions can be included in the model. As presented in this treatment, the Dynamic Matrix Approach considers free boundary conditions at the edges. Nonetheless, surface phenomena may be included in the calculations by considering the surface interactions as bulk interactions, where such terms are present only in the magnetic cells at the boundaries. The key idea is that, for small cells, these interactions (included at the surfaces or boundaries) are quite equivalent to introducing them through proper boundary conditions. Thus, the current theoretical model can include surface anisotropies, the Dzyaloshinskii-Moriya interaction, and other interfacial contributions.

Bibliography

- [1]A. Khitun, M. Bao, and K. L. Wang, “Magnonic logic circuits,” *Journal of Physics D: Applied Physics*, vol. 43, no. 26, p. 264 005, Jul. 7, 2010 (cit. on p. 1).
- [2]A. V. Chumak, V. I. Vasyuchka, A. A. Serga, and B. Hillebrands, “Magnon spintronics,” *Nature Physics*, vol. 11, no. 6, pp. 453–461, Jun. 2015 (cit. on pp. 1, 4).
- [3]J. H. Kwon, J. Yoon, P. Deorani, *et al.*, “Giant nonreciprocal emission of spin waves in Ta/Py bilayers,” *Science Advances*, vol. 2, no. 7, e1501892, Jul. 29, 2016 (cit. on pp. 1, 39, 41).
- [4]V. Sluka, T. Schneider, R. A. Gallardo, *et al.*, “Emission and Propagation of Multi-Dimensional Spin Waves with nanoscale wavelengths in Anisotropic Spin Textures,” *Nature Nanotechnology*, vol. 14, no. 4, pp. 328–333, Apr. 2019. arXiv: 1807.00897 (cit. on pp. 1–3, 27, 51, 64).
- [5]A. G. Gurevich and G. A. Melkov, *Magnetization Oscillations and Waves*. Boca Raton: CRC Press, 1996, 445 pp. (cit. on pp. 1, 11).
- [6]V. V. Kruglyak, S. O. Demokritov, and D. Grundler, “Magnonics,” *Journal of Physics D: Applied Physics*, vol. 43, no. 26, p. 264 001, Jul. 7, 2010 (cit. on p. 1).
- [7]N. Locatelli, V. Cros, and J. Grollier, “Spin-torque building blocks,” *Nature Materials*, vol. 13, no. 1, pp. 11–20, Jan. 2014 (cit. on p. 1).
- [8]G. E. W. Bauer, E. Saitoh, and B. J. van Wees, “Spin caloritronics,” *Nature Materials*, vol. 11, no. 5, pp. 391–399, May 2012 (cit. on p. 1).
- [9]M. Jamali, J. H. Kwon, S.-M. Seo, K.-J. Lee, and H. Yang, “Spin wave nonreciprocity for logic device applications,” *Scientific Reports*, vol. 3, no. 1, p. 3160, Dec. 2013 (cit. on pp. 1, 4, 41).
- [10]B. Lenk, H. Ulrichs, F. Garbs, and M. Münzenberg, “The building blocks of magnonics,” *Physics Reports*, vol. 507, no. 4-5, pp. 107–136, Oct. 2011 (cit. on p. 1).

- [11]M. Krawczyk and D. Grundler, “Review and prospects of magnonic crystals and devices with reprogrammable band structure,” *Journal of Physics: Condensed Matter*, vol. 26, no. 12, p. 123 202, Mar. 26, 2014 (cit. on pp. 1, 60).
- [12]A. V. Chumak, A. A. Serga, and B. Hillebrands, “Magnonic crystals for data processing,” *Journal of Physics D: Applied Physics*, vol. 50, no. 24, p. 244 001, Jun. 21, 2017 (cit. on pp. 1, 4).
- [13]H. Yu, J. Xiao, and H. Schultheiss, “Magnetic texture based magnonics,” *Physics Reports*, vol. 905, pp. 1–59, Apr. 2021 (cit. on pp. 1, 69).
- [14]E. Albisetti, S. Tacchi, R. Silvani, *et al.*, “Optically Inspired Nanomagnonics with Nonreciprocal Spin Waves in Synthetic Antiferromagnets,” *Advanced Materials*, vol. 32, no. 9, p. 1 906 439, Mar. 2020 (cit. on pp. 1, 2).
- [15]P. Graczyk, J. Kłos, and M. Krawczyk, “Broadband magnetoelastic coupling in magnonic-phononic crystals for high-frequency nanoscale spin-wave generation,” *Physical Review B*, vol. 95, no. 10, p. 104 425, Mar. 20, 2017 (cit. on p. 1).
- [16]D. A. Bozhko, V. I. Vasyuchka, A. V. Chumak, and A. A. Serga, “Magnon-phonon interactions in magnon spintronics (Review article),” *Low Temperature Physics*, vol. 46, no. 4, pp. 383–399, Apr. 2020 (cit. on p. 1).
- [17]A. Barman, G. Gubbiotti, S. Ladak, *et al.*, “The 2021 Magnonics Roadmap,” *Journal of Physics: Condensed Matter*, vol. 33, no. 41, p. 413 001, Oct. 13, 2021 (cit. on pp. 2, 59).
- [18]K. Di, V. L. Zhang, H. S. Lim, *et al.*, “Direct Observation of the Dzyaloshinskii-Moriya Interaction in a Pt/Co/Ni Film,” *Physical Review Letters*, vol. 114, no. 4, p. 047 201, Jan. 28, 2015 (cit. on p. 2).
- [19]J. Cho, N.-H. Kim, S. Lee, *et al.*, “Thickness dependence of the interfacial Dzyaloshinskii–Moriya interaction in inversion symmetry broken systems,” *Nature Communications*, vol. 6, no. 1, p. 7635, Nov. 2015 (cit. on p. 2).
- [20]H. T. Nembach, J. M. Shaw, M. Weiler, E. Jué, and T. J. Silva, “Linear relation between Heisenberg exchange and interfacial Dzyaloshinskii–Moriya interaction in metal films,” *Nature Physics*, vol. 11, no. 10, pp. 825–829, Oct. 2015 (cit. on p. 2).
- [21]M. Belmeguenai, J.-P. Adam, Y. Roussigné, *et al.*, “Interfacial Dzyaloshinskii-Moriya interaction in perpendicularly magnetized Pt/Co/AlO_x ultrathin films measured by Brillouin light spectroscopy,” *Physical Review B*, vol. 91, no. 18, p. 180 405, May 20, 2015 (cit. on p. 2).

- [22]A. K. Chaurasiya, C. Banerjee, S. Pan, *et al.*, “Direct Observation of Interfacial Dzyaloshinskii-Moriya Interaction from Asymmetric Spin-wave Propagation in W/CoFeB/SiO₂ Heterostructures Down to Sub-nanometer CoFeB Thickness,” *Scientific Reports*, vol. 6, no. 1, p. 32 592, Dec. 2016 (cit. on p. 2).
- [23]S. Tacchi, R. E. Troncoso, M. Ahlberg, *et al.*, “Interfacial Dzyaloshinskii-Moriya Interaction in Pt / CoFeB Films: Effect of the Heavy-Metal Thickness,” *Physical Review Letters*, vol. 118, no. 14, p. 147 201, Apr. 3, 2017 (cit. on p. 2).
- [24]R. A. Gallardo, D. Cortés-Ortuño, R. E. Troncoso, and P. Landeros, “Spin waves in thin films and magnonic crystals with Dzyaloshinskii–Moriya interactions,” in *Three-Dimensional Magnonics*, G. Gubbiotti, Ed., Singapore: Jenny Stanford Publishing, 2019, pp. 121–160 (cit. on pp. 2, 4).
- [25]M. Kataoka, “Spin Waves in Systems with Long Period Helical Spin Density Waves Due to the Antisymmetric and Symmetric Exchange Interactions,” *Journal of the Physical Society of Japan*, vol. 56, no. 10, pp. 3635–3647, Oct. 15, 1987 (cit. on p. 2).
- [26]D. Cortés-Ortuño and P. Landeros, “Influence of the Dzyaloshinskii–Moriya interaction on the spin-wave spectra of thin films,” *Journal of Physics: Condensed Matter*, vol. 25, no. 15, p. 156 001, Apr. 17, 2013 (cit. on p. 2).
- [27]Y. Iguchi, S. Uemura, K. Ueno, and Y. Onose, “Nonreciprocal magnon propagation in a noncentrosymmetric ferromagnet LiFe₅O₈,” *Physical Review B*, vol. 92, no. 18, p. 184 419, Nov. 18, 2015 (cit. on p. 2).
- [28]S. Seki, Y. Okamura, K. Kondou, *et al.*, “Magnetochiral nonreciprocity of volume spin wave propagation in chiral-lattice ferromagnets,” *Physical Review B*, vol. 93, no. 23, p. 235 131, Jun. 16, 2016 (cit. on p. 2).
- [29]T. Weber, J. Waizner, G. S. Tucker, *et al.*, “Non-reciprocal magnons in non-centrosymmetric MnSi,” *AIP Advances*, vol. 8, no. 10, p. 101 328, Oct. 2018 (cit. on p. 2).
- [30]T. J. Sato and K. Matan, “Nonreciprocal Magnons in Noncentrosymmetric Magnets,” *Journal of the Physical Society of Japan*, vol. 88, no. 8, p. 081 007, Aug. 15, 2019 (cit. on p. 2).
- [31]J. A. Otálora, M. Yan, H. Schultheiss, R. Hertel, and A. Kákay, “Curvature-Induced Asymmetric Spin-Wave Dispersion,” *Physical Review Letters*, vol. 117, no. 22, p. 227 203, Nov. 23, 2016 (cit. on p. 2).
- [32]D. D. Sheka, O. V. Pylypovskyi, P. Landeros, *et al.*, “Nonlocal chiral symmetry breaking in curvilinear magnetic shells,” *Communications Physics*, vol. 3, no. 1, p. 128, Dec. 2020 (cit. on p. 2).

- [33]R. A. Gallardo, P. Alvarado-Seguel, T. Schneider, *et al.*, “Spin-wave non-reciprocity in magnetization-graded ferromagnetic films,” *New Journal of Physics*, vol. 21, no. 3, p. 033 026, Mar. 28, 2019 (cit. on pp. 2, 37, 38, 51).
- [34]M. Grassi, M. Geilen, D. Louis, *et al.*, “Slow-Wave-Based Nanomagnonic Diode,” *Physical Review Applied*, vol. 14, no. 2, p. 024 047, Aug. 18, 2020 (cit. on p. 2).
- [35]A. F. Franco and P. Landeros, “Enhancement of the spin-wave nonreciprocity in antiferromagnetically coupled multilayers with dipolar and interfacial Dzyaloshinskii-Moriya interactions,” *Physical Review B*, vol. 102, no. 18, p. 184 424, Nov. 19, 2020 (cit. on p. 2).
- [36]K. Mika and P. Grünberg, “Dipolar spin-wave modes of a ferromagnetic multilayer with alternating directions of magnetization,” *Physical Review B*, vol. 31, no. 7, pp. 4465–4471, Apr. 1, 1985 (cit. on p. 2).
- [37]P. Grünberg, “Some ways to modify the spin-wave mode spectra of magnetic multilayers (invited),” *Journal of Applied Physics*, vol. 57, no. 8, pp. 3673–3677, Apr. 15, 1985 (cit. on p. 2).
- [38]P. Grünberg, R. Schreiber, Y. Pang, M. B. Brodsky, and H. Sowers, “Layered Magnetic Structures: Evidence for Antiferromagnetic Coupling of Fe Layers across Cr Interlayers,” *Physical Review Letters*, vol. 57, no. 19, pp. 2442–2445, Nov. 10, 1986 (cit. on p. 2).
- [39]P. X. Zhang and W. Zinn, “Spin-wave modes in antiparallel magnetized ferromagnetic double layers,” *Physical Review B*, vol. 35, no. 10, pp. 5219–5225, Apr. 1, 1987 (cit. on p. 2).
- [40]G. Binasch, P. Grünberg, F. Saurenbach, and W. Zinn, “Enhanced magnetoresistance in layered magnetic structures with antiferromagnetic interlayer exchange,” *Physical Review B*, vol. 39, no. 7, pp. 4828–4830, Mar. 1, 1989 (cit. on p. 2).
- [41]J. Barnaś and P. Grünberg, “Spin waves in exchange-coupled epitaxial double-layers,” *Journal of Magnetism and Magnetic Materials*, vol. 82, no. 2-3, pp. 186–198, Dec. 1989 (cit. on p. 2).
- [42]R. Gallardo, T. Schneider, A. Chaurasiya, *et al.*, “Reconfigurable Spin-Wave Nonreciprocity Induced by Dipolar Interaction in a Coupled Ferromagnetic Bilayer,” *Physical Review Applied*, vol. 12, no. 3, p. 034 012, Sep. 9, 2019 (cit. on pp. 2, 3, 57, 58, 61).
- [43]K. Di, S. X. Feng, S. N. Piramanayagam, *et al.*, “Enhancement of spin-wave nonreciprocity in magnonic crystals via synthetic antiferromagnetic coupling,” *Scientific Reports*, vol. 5, no. 1, p. 10 153, Sep. 2015 (cit. on pp. 2, 51).

- [44]P. Alvarado-Seguel and R. A. Gallardo, “Band structure of a one-dimensional bilayer magnonic crystal,” *Physical Review B*, vol. 100, no. 14, p. 144 415, Oct. 9, 2019 (cit. on p. 2).
- [45]R. Verba, V. Tiberkevich, E. Bankowski, *et al.*, “Conditions for the spin wave non-reciprocity in an array of dipolarly coupled magnetic nanopillars,” *Applied Physics Letters*, vol. 103, no. 8, p. 082 407, Aug. 19, 2013 (cit. on p. 2).
- [46]R. Camley, “Nonreciprocal surface waves,” *Surface Science Reports*, vol. 7, no. 3-4, pp. 103–187, Jul. 1987 (cit. on p. 2).
- [47]J. Lan, W. Yu, R. Wu, and J. Xiao, “Spin-Wave Diode,” *Physical Review X*, vol. 5, no. 4, p. 041 049, Dec. 28, 2015 (cit. on pp. 2, 3).
- [48]N. Reiskarimian and H. Krishnaswamy, “Magnetic-free non-reciprocity based on staggered commutation,” *Nature Communications*, vol. 7, no. 1, p. 11 217, Sep. 2016 (cit. on pp. 2, 3).
- [49]D. L. Sounas and A. Alù, “Non-reciprocal photonics based on time modulation,” *Nature Photonics*, vol. 11, no. 12, pp. 774–783, Dec. 2017 (cit. on pp. 2, 3).
- [50]M. Ishibashi, Y. Shiota, T. Li, *et al.*, “Switchable giant nonreciprocal frequency shift of propagating spin waves in synthetic antiferromagnets,” *Science Advances*, vol. 6, no. 17, eaaz6931, Apr. 22, 2020 (cit. on pp. 2, 3, 57).
- [51]M. Berry and C. Upstill, “IV Catastrophe Optics: Morphologies of Caustics and Their Diffraction Patterns,” in *Progress in Optics*, vol. 18, Elsevier, 1980, pp. 257–346 (cit. on p. 3).
- [52]Y. A. Kravtsov and Y. I. Orlov, *Caustics, Catastrophes and Wave Fields* (Springer Series on Wave Phenomena), red. by L. M. Brekhovskikh, L. B. Felsen, and H. A. Haus. Berlin, Heidelberg: Springer Berlin Heidelberg, 1993, vol. 15 (cit. on p. 3).
- [53]L. Froehly, F. Courvoisier, A. Mathis, *et al.*, “Arbitrary accelerating micron-scale caustic beams in two and three dimensions,” *Optics Express*, vol. 19, no. 17, p. 16 455, Aug. 15, 2011 (cit. on p. 3).
- [54]A. Tanaka, “Phase Space Caustics in Multicomponent Systems,” *Physical Review Letters*, vol. 80, no. 7, pp. 1414–1417, Feb. 16, 1998 (cit. on p. 3).
- [55]C. Charmousis, V. Onemli, Z. Qiu, and P. Sikivie, “Gravitational lensing by dark matter caustics,” *Physical Review D*, vol. 67, no. 10, p. 103 502, May 12, 2003 (cit. on p. 3).
- [56]A. I. Harte and T. D. Drivas, “Caustics and wave propagation in curved spacetimes,” *Physical Review D*, vol. 85, no. 12, p. 124 039, Jun. 19, 2012 (cit. on p. 3).

- [57]K. Pasmatsiou, “Caustic formation upon shift symmetry breaking,” *Physical Review D*, vol. 97, no. 3, p. 036 008, Feb. 12, 2018 (cit. on p. 3).
- [58]V. T. Buchwald, “RAYLEIGH WAVES IN TRANSVERSELY ISOTROPIC MEDIA,” *The Quarterly Journal of Mechanics and Applied Mathematics*, vol. 14, no. 3, pp. 293–318, 1961 (cit. on p. 3).
- [59]G. A. Northrop and J. P. Wolfe, “Ballistic phonon imaging in germanium,” *Physical Review B*, vol. 22, no. 12, pp. 6196–6212, Dec. 15, 1980 (cit. on p. 3).
- [60]P. Taborek and D. Goodstein, “Phonon focusing catastrophes,” *Solid State Communications*, vol. 33, no. 12, pp. 1191–1194, Mar. 1980 (cit. on p. 3).
- [61]R. E. Camley and A. A. Maradudin, “Phonon focusing at surfaces,” *Physical Review B*, vol. 27, no. 4, pp. 1959–1964, Feb. 15, 1983 (cit. on p. 3).
- [62]A. G. Every, “Formation of phonon-focusing caustics in crystals,” *Physical Review B*, vol. 34, no. 4, pp. 2852–2862, Aug. 15, 1986 (cit. on p. 3).
- [63]I. Epstein and A. Arie, “Arbitrary Bending Plasmonic Light Waves,” *Physical Review Letters*, vol. 112, no. 2, p. 023 903, Jan. 15, 2014 (cit. on p. 3).
- [64]X. Shi, X. Lin, F. Gao, *et al.*, “Caustic graphene plasmons with Kelvin angle,” *Physical Review B*, vol. 92, no. 8, p. 081 404, Aug. 11, 2015 (cit. on p. 3).
- [65]J. Spector, H. L. Stormer, K. W. Baldwin, L. N. Pfeiffer, and K. W. West, “Electron focusing in two-dimensional systems by means of an electrostatic lens,” *Applied Physics Letters*, vol. 56, no. 13, pp. 1290–1292, Mar. 26, 1990 (cit. on p. 3).
- [66]V. V. Cheianov, V. Fal’ko, and B. L. Altshuler, “The Focusing of Electron Flow and a Veselago Lens in Graphene *p-n* Junctions,” *Science*, vol. 315, no. 5816, pp. 1252–1255, Mar. 2, 2007 (cit. on p. 3).
- [67]J. Cserti, A. Pályi, and C. Péterfalvi, “Caustics due to a Negative Refractive Index in Circular Graphene *p-n* Junctions,” *Physical Review Letters*, vol. 99, no. 24, p. 246 801, Dec. 11, 2007 (cit. on p. 3).
- [68]V. Krivoruchko and A. Savchenko, “Electric Field Control of Magnon Power Flow in Thin Ferromagnet Films,” *Acta Physica Polonica A*, vol. 133, no. 3, pp. 463–465, Mar. 2018 (cit. on p. 3).
- [69]J. J. Bible and R. E. Camley, “Focusing of high-wave-vector magnons,” *Physical Review B*, vol. 95, no. 22, p. 224 412, Jun. 8, 2017 (cit. on p. 3).

- [70]F. Heussner, G. Talmelli, M. Geilen, *et al.*, “Experimental Realization of a Passive Gigahertz Frequency-Division Demultiplexer for Magnonic Logic Networks,” *physica status solidi (RRL) – Rapid Research Letters*, vol. 14, no. 4, p. 1900695, Apr. 2020 (cit. on p. 3).
- [71]V. Veerakumar and R. E. Camley, “Magnon focusing in thin ferromagnetic films,” *Physical Review B*, vol. 74, no. 21, p. 214401, Dec. 1, 2006 (cit. on p. 3).
- [72]V. E. Demidov, S. O. Demokritov, D. Birt, *et al.*, “Radiation of spin waves from the open end of a microscopic magnetic-film waveguide,” *Physical Review B*, vol. 80, no. 1, p. 014429, Jul. 27, 2009 (cit. on p. 3).
- [73]T. Schneider, A. A. Serga, A. V. Chumak, *et al.*, “Nondiffractive Subwavelength Wave Beams in a Medium with Externally Controlled Anisotropy,” *Physical Review Letters*, vol. 104, no. 19, p. 197203, May 13, 2010 (cit. on p. 3).
- [74]S. Mansfeld, J. Topp, K. Martens, *et al.*, “Spin Wave Diffraction and Perfect Imaging of a Grating,” *Physical Review Letters*, vol. 108, no. 4, p. 047204, Jan. 26, 2012 (cit. on p. 3).
- [75]T. Sebastian, T. Brächer, P. Pirro, *et al.*, “Nonlinear Emission of Spin-Wave Caustics from an Edge Mode of a Microstructured Co₂Mn_{0.6}Fe_{0.4}Si Waveguide,” *Physical Review Letters*, vol. 110, no. 6, p. 067201, Feb. 4, 2013 (cit. on p. 3).
- [76]R. Gieniusz, H. Ulrichs, V. D. Bessonov, *et al.*, “Single antidot as a passive way to create caustic spin-wave beams in yttrium iron garnet films,” *Applied Physics Letters*, vol. 102, no. 10, p. 102409, Mar. 11, 2013 (cit. on p. 3).
- [77]J.-V. Kim, R. L. Stamps, and R. E. Camley, “Spin Wave Power Flow and Caustics in Ultrathin Ferromagnets with the Dzyaloshinskii-Moriya Interaction,” *Physical Review Letters*, vol. 117, no. 19, p. 197204, Nov. 4, 2016 (cit. on pp. 3, 59, 65).
- [78]F. Heussner, A. A. Serga, T. Brächer, B. Hillebrands, and P. Pirro, “A switchable spin-wave signal splitter for magnonic networks,” *Applied Physics Letters*, vol. 111, no. 12, p. 122401, Sep. 18, 2017 (cit. on p. 3).
- [79]R. L. Stamps, J.-V. Kim, F. Garcia-Sanchez, *et al.*, “Spin waves on spin structures: Topology, localization, and nonreciprocity,” in *Spin Wave Confinement: Propagating Waves*, S. O. Demokritov, Ed., Second edition, Singapore: Pan Stanford Publishing, 2017, pp. 219–260 (cit. on p. 3).
- [80]J. M. Winter, “Bloch Wall Excitation. Application to Nuclear Resonance in a Bloch Wall,” *Physical Review*, vol. 124, no. 2, pp. 452–459, Oct. 15, 1961 (cit. on p. 3).

- [81]F. Garcia-Sanchez, P. Borys, R. Soucaille, *et al.*, “Narrow Magnonic Waveguides Based on Domain Walls,” *Physical Review Letters*, vol. 114, no. 24, p. 247 206, Jun. 18, 2015 (cit. on p. 3).
- [82]K. Wagner, A. Kákay, K. Schultheiss, *et al.*, “Magnetic domain walls as reconfigurable spin-wave nanochannels,” *Nature Nanotechnology*, vol. 11, no. 5, pp. 432–436, May 2016 (cit. on p. 3).
- [83]X. Xing and Y. Zhou, “Fiber optics for spin waves,” *NPG Asia Materials*, vol. 8, no. 3, e246–e246, Mar. 2016 (cit. on p. 3).
- [84]S. J. Hämäläinen, M. Madami, H. Qin, G. Gubbiotti, and S. van Dijken, “Control of spin-wave transmission by a programmable domain wall,” *Nature Communications*, vol. 9, no. 1, p. 4853, Dec. 2018 (cit. on p. 3).
- [85]A. Lara, V. Metlushko, and F. G. Aliev, “Observation of propagating edge spin waves modes,” *Journal of Applied Physics*, vol. 114, no. 21, p. 213 905, Dec. 7, 2013 (cit. on p. 3).
- [86]A. Roldán-Molina, A. S. Nunez, and J. Fernández-Rossier, “Topological spin waves in the atomic-scale magnetic skyrmion crystal,” *New Journal of Physics*, vol. 18, no. 4, p. 045 015, Apr. 19, 2016 (cit. on pp. 3, 73).
- [87]A. Lara, J. Robledo Moreno, K. Y. Guslienko, and F. G. Aliev, “Information processing in patterned magnetic nanostructures with edge spin waves,” *Scientific Reports*, vol. 7, no. 1, p. 5597, Dec. 2017 (cit. on p. 3).
- [88]M. Garst, J. Waizner, and D. Grundler, “Collective spin excitations of helices and magnetic skyrmions: Review and perspectives of magnonics in non-centrosymmetric magnets,” *Journal of Physics D: Applied Physics*, vol. 50, no. 29, p. 293 002, Jul. 26, 2017 (cit. on p. 3).
- [89]X. Xing, Y. Zhou, and H. Braun, “Magnetic Skyrmion Tubes as Nonplanar Magnonic Waveguides,” *Physical Review Applied*, vol. 13, no. 3, p. 034 051, Mar. 19, 2020 (cit. on p. 3).
- [90]U. Levy, M. Abashin, K. Ikeda, *et al.*, “Inhomogenous Dielectric Metamaterials with Space-Variant Polarizability,” *Physical Review Letters*, vol. 98, no. 24, p. 243 901, Jun. 13, 2007 (cit. on p. 4).
- [91]E. Hecht, *Optics*, 5th ed. Pearson Education India, 2002 (cit. on p. 4).
- [92]C. Markos, J. C. Travers, A. Abdolvand, B. J. Eggleton, and O. Bang, “Hybrid photonic-crystal fiber,” *Reviews of Modern Physics*, vol. 89, no. 4, p. 045 003, Nov. 27, 2017 (cit. on p. 4).

- [93]D. E. Boonzajer Flaes, J. Stopka, S. Turtaev, *et al.*, “Robustness of Light-Transport Processes to Bending Deformations in Graded-Index Multimode Waveguides,” *Physical Review Letters*, vol. 120, no. 23, p. 233 901, Jun. 6, 2018 (cit. on p. 4).
- [94]M. Vogel, R. Aßmann, P. Pirro, *et al.*, “Control of Spin-Wave Propagation using Magnetisation Gradients,” *Scientific Reports*, vol. 8, no. 1, p. 11 099, Dec. 2018 (cit. on p. 4).
- [95]M. Vogel, P. Pirro, B. Hillebrands, and G. von Freymann, “Optical elements for anisotropic spin-wave propagation,” *Applied Physics Letters*, vol. 116, no. 26, p. 262 404, Jun. 29, 2020 (cit. on p. 4).
- [96]D.-E. Jeong, D.-S. Han, and S.-K. Kim, “REFRACTIVE INDEX AND SNELL’S LAW FOR DIPOLE-EXCHANGE SPIN WAVES IN RESTRICTED GEOMETRY,” *SPIN*, vol. 01, no. 01, pp. 27–31, Jun. 2011 (cit. on p. 4).
- [97]Y. I. Gorobets and S. A. Reshetnyak, “Reflection and refraction of spin waves in uniaxial magnets in the geometrical-optics approximation,” *Technical Physics*, vol. 43, no. 2, pp. 188–191, Feb. 1998 (cit. on p. 4).
- [98]C. S. Davies and V. V. Kruglyak, “Graded-index magnonics,” *Low Temperature Physics*, vol. 41, no. 10, pp. 760–766, Oct. 2015 (cit. on p. 4).
- [99]A. V. Vashkovskii and E. H. Lokk, “Negative refractive index for a surface magneto-static wave propagating through the boundary between a ferrite and ferrite-insulator-metal media,” *Physics-Uspekhi*, vol. 47, no. 6, pp. 601–605, Jun. 30, 2004 (cit. on p. 4).
- [100]S.-K. Kim, S. Choi, K.-S. Lee, *et al.*, “Negative refraction of dipole-exchange spin waves through a magnetic twin interface in restricted geometry,” *Applied Physics Letters*, vol. 92, no. 21, p. 212 501, May 26, 2008 (cit. on p. 4).
- [101]P. Gruszecki and M. Krawczyk, “Spin-wave beam propagation in ferromagnetic thin films with graded refractive index: Mirage effect and prospective applications,” *Physical Review B*, vol. 97, no. 9, p. 094 424, Mar. 23, 2018 (cit. on p. 4).
- [102]J. Jorzick, S. O. Demokritov, B. Hillebrands, *et al.*, “Spin Wave Wells in Nonellipsoidal Micrometer Size Magnetic Elements,” *Physical Review Letters*, vol. 88, no. 4, p. 047 204, Jan. 14, 2002 (cit. on p. 4).
- [103]J. P. Park, P. Eames, D. M. Engebretson, J. Berezovsky, and P. A. Crowell, “Spatially Resolved Dynamics of Localized Spin-Wave Modes in Ferromagnetic Wires,” *Physical Review Letters*, vol. 89, no. 27, p. 277 201, Dec. 18, 2002 (cit. on p. 4).

- [104]V. V. Kruglyak, A. Barman, R. J. Hicken, J. R. Childress, and J. A. Katine, “Picosecond magnetization dynamics in nanomagnets: Crossover to nonuniform precession,” *Physical Review B*, vol. 71, no. 22, p. 220 409, Jun. 27, 2005 (cit. on p. 4).
- [105]V. E. Demidov, S. O. Demokritov, K. Rott, P. Krzysteczko, and G. Reiss, “Nano-optics with spin waves at microwave frequencies,” *Applied Physics Letters*, vol. 92, no. 23, p. 232 503, Jun. 9, 2008 (cit. on p. 4).
- [106]K. G. Fripp and V. V. Kruglyak, “Spin-wave wells revisited: From wavelength conversion and Möbius modes to magnon valleytronics,” *Physical Review B*, vol. 103, no. 18, p. 184 403, May 3, 2021 (cit. on p. 4).
- [107]C. Mathieu, J. Jorzick, A. Frank, *et al.*, “Lateral Quantization of Spin Waves in Micron Size Magnetic Wires,” *Physical Review Letters*, vol. 81, no. 18, pp. 3968–3971, Nov. 2, 1998 (cit. on p. 4).
- [108]J. Jorzick, S. O. Demokritov, C. Mathieu, *et al.*, “Brillouin light scattering from quantized spin waves in micron-size magnetic wires,” *Physical Review B*, vol. 60, no. 22, pp. 15 194–15 200, Dec. 1, 1999 (cit. on p. 4).
- [109]J. V. Mantese, A. L. Micheli, N. W. Schubring, *et al.*, “Magnetization-graded ferromagnets: The magnetic analogs of semiconductor junction elements,” *Applied Physics Letters*, vol. 87, no. 8, p. 082 503, Aug. 22, 2005 (cit. on p. 4).
- [110]L. Fallarino, P. Riego, B. Kirby, C. Miller, and A. Berger, “Modulation of Magnetic Properties at the Nanometer Scale in Continuously Graded Ferromagnets,” *Materials*, vol. 11, no. 2, p. 251, Feb. 6, 2018 (cit. on pp. 4, 65, 73).
- [111]C. Sudakar, R. Naik, G. Lawes, *et al.*, “Internal magnetostatic potentials of magnetization-graded ferromagnetic materials,” *Applied Physics Letters*, vol. 90, no. 6, p. 062 502, Feb. 5, 2007 (cit. on p. 4).
- [112]A. Berger, N. Supper, Y. Ikeda, *et al.*, “Improved media performance in optimally coupled exchange spring layer media,” *Applied Physics Letters*, vol. 93, no. 12, p. 122 502, Sep. 22, 2008 (cit. on p. 4).
- [113]T.-J. Zhou, B. C. Lim, and B. Liu, “Anisotropy graded FePt–TiO₂ nanocomposite thin films with small grain size,” *Applied Physics Letters*, vol. 94, no. 15, p. 152 505, Apr. 13, 2009 (cit. on pp. 4, 65).
- [114]B. J. Kirby, J. E. Davies, K. Liu, *et al.*, “Vertically graded anisotropy in Co/Pd multilayers,” *Physical Review B*, vol. 81, no. 10, p. 100 405, Mar. 8, 2010 (cit. on pp. 4, 65).

- [115]R. K. Dumas, Y. Fang, B. J. Kirby, *et al.*, “Probing vertically graded anisotropy in FePtCu films,” *Physical Review B*, vol. 84, no. 5, p. 054 434, Aug. 10, 2011 (cit. on p. 4).
- [116]B. J. Kirby, H. F. Belliveau, D. D. Belyea, *et al.*, “Spatial Evolution of the Ferromagnetic Phase Transition in an Exchange Graded Film,” *Physical Review Letters*, vol. 116, no. 4, p. 047 203, Jan. 29, 2016 (cit. on pp. 4, 65, 73).
- [117]L. Fallarino, B. J. Kirby, M. Pancaldi, *et al.*, “Magnetic properties of epitaxial CoCr films with depth-dependent exchange-coupling profiles,” *Physical Review B*, vol. 95, no. 13, p. 134 445, Apr. 27, 2017 (cit. on p. 4).
- [118]B. J. Kirby, L. Fallarino, P. Riego, *et al.*, “Nanoscale magnetic localization in exchange strength modulated ferromagnets,” *Physical Review B*, vol. 98, no. 6, p. 064 404, Aug. 3, 2018 (cit. on p. 4).
- [119]P. Landeros and D. L. Mills, “Spin waves in periodically perturbed films,” *Physical Review B*, vol. 85, no. 5, p. 054 424, Feb. 22, 2012 (cit. on p. 4).
- [120]M. Langer, R. A. Gallardo, T. Schneider, *et al.*, “Spin-wave modes in transition from a thin film to a full magnonic crystal,” *Physical Review B*, vol. 99, no. 2, p. 024 426, Jan. 24, 2019 (cit. on p. 4).
- [121]J. W. Kłos, D. Kumar, J. Romero-Vivas, *et al.*, “Effect of magnetization pinning on the spectrum of spin waves in magnonic antidot waveguides,” *Physical Review B*, vol. 86, no. 18, p. 184 433, Nov. 30, 2012 (cit. on p. 4).
- [122]M. Krawczyk, S. Mamica, M. Mruczkiewicz, *et al.*, “Magnonic band structures in two-dimensional bi-component magnonic crystals with in-plane magnetization,” *Journal of Physics D: Applied Physics*, vol. 46, no. 49, p. 495 003, Dec. 11, 2013 (cit. on p. 4).
- [123]M. Körner, K. Lenz, R. A. Gallardo, *et al.*, “Two-magnon scattering in permalloy thin films due to rippled substrates,” *Physical Review B*, vol. 88, no. 5, p. 054 405, Aug. 9, 2013 (cit. on p. 4).
- [124]R. A. Gallardo, A. Banholzer, K. Wagner, *et al.*, “Splitting of spin-wave modes in thin films with arrays of periodic perturbations: Theory and experiment,” *New Journal of Physics*, vol. 16, no. 2, p. 023 015, Feb. 6, 2014 (cit. on p. 4).
- [125]S. A. Odintsov, A. V. Sadovnikov, A. A. Grachev, *et al.*, “Spatial–frequency selection of magnetostatic waves in a two-dimensional magnonic crystal lattice,” *JETP Letters*, vol. 104, no. 8, pp. 563–567, Oct. 2016 (cit. on p. 4).

- [126]M. Langer, F. Röder, R. A. Gallardo, *et al.*, “Role of internal demagnetizing field for the dynamics of a surface-modulated magnonic crystal,” *Physical Review B*, vol. 95, no. 18, p. 184 405, May 5, 2017 (cit. on p. 4).
- [127]G. Gubbiotti, L. L. Xiong, F. Montoncello, and A. O. Adeyeye, “Collective spin waves in arrays of permalloy nanowires with single-side periodically modulated width,” *Applied Physics Letters*, vol. 111, no. 19, p. 192 403, Nov. 6, 2017 (cit. on p. 4).
- [128]R. A. Gallardo, T. Schneider, A. Roldán-Molina, *et al.*, “Dipolar interaction induced band gaps and flat modes in surface-modulated magnonic crystals,” *Physical Review B*, vol. 97, no. 14, p. 144 405, Apr. 10, 2018 (cit. on p. 4).
- [129]Z. K. Wang, V. L. Zhang, H. S. Lim, *et al.*, “Observation of frequency band gaps in a one-dimensional nanostructured magnonic crystal,” *Applied Physics Letters*, vol. 94, no. 8, p. 083 112, Feb. 23, 2009 (cit. on pp. 4, 5).
- [130]Q. Wang, A. V. Chumak, L. Jin, *et al.*, “Voltage-controlled nanoscale reconfigurable magnonic crystal,” *Physical Review B*, vol. 95, no. 13, p. 134 433, Apr. 19, 2017 (cit. on p. 4).
- [131]Z. K. Wang, V. L. Zhang, H. S. Lim, *et al.*, “Nanostructured Magnonic Crystals with Size-Tunable Bandgaps,” *ACS Nano*, vol. 4, no. 2, pp. 643–648, Feb. 23, 2010 (cit. on pp. 4, 5).
- [132]I. Barsukov, F. M. Römer, R. Meckenstock, *et al.*, “Frequency dependence of spin relaxation in periodic systems,” *Physical Review B*, vol. 84, no. 14, p. 140 410, Oct. 31, 2011 (cit. on p. 4).
- [133]F. S. Ma, H. S. Lim, Z. K. Wang, *et al.*, “Micromagnetic study of spin wave propagation in bicomponent magnonic crystal waveguides,” *Applied Physics Letters*, vol. 98, no. 15, p. 153 107, Apr. 11, 2011 (cit. on pp. 4, 5).
- [134]F. S. Ma, H. S. Lim, V. L. Zhang, *et al.*, “Band structures of exchange spin waves in one-dimensional bi-component magnonic crystals,” *Journal of Applied Physics*, vol. 111, no. 6, p. 064 326, Mar. 15, 2012 (cit. on pp. 4, 5).
- [135]S. Tacchi, G. Duerr, J. W. Klos, *et al.*, “Forbidden Band Gaps in the Spin-Wave Spectrum of a Two-Dimensional Bicomponent Magnonic Crystal,” *Physical Review Letters*, vol. 109, no. 13, p. 137 202, Sep. 28, 2012 (cit. on p. 4).
- [136]B. Obry, P. Pirro, T. Brächer, *et al.*, “A micro-structured ion-implanted magnonic crystal,” *Applied Physics Letters*, vol. 102, no. 20, p. 202 403, May 20, 2013 (cit. on p. 4).

- [137]S. Saha, S. Barman, J. Ding, A. O. Adeyeye, and A. Barman, “Time-domain study of spin-wave dynamics in two-dimensional arrays of bi-component magnetic structures,” *Applied Physics Letters*, vol. 102, no. 24, p. 242 409, Jun. 17, 2013 (cit. on pp. 4, 5).
- [138]J. Rychły, P. Gruszecki, M. Mruczkiewicz, *et al.*, “Magnonic crystals—Prospective structures for shaping spin waves in nanoscale,” *Low Temperature Physics*, vol. 41, no. 10, pp. 745–759, Oct. 2015 (cit. on pp. 4, 45).
- [139]G. Gubbiotti, X. Zhou, Z. Haghshenasfard, M. G. Cottam, and A. O. Adeyeye, “Reprogrammable magnonic band structure of layered permalloy/Cu/permalloy nanowires,” *Physical Review B*, vol. 97, no. 13, p. 134 428, Apr. 26, 2018 (cit. on p. 4).
- [140]R. A. Gallardo, D. Cortés-Ortuño, T. Schneider, *et al.*, “Flat Bands, Indirect Gaps, and Unconventional Spin-Wave Behavior Induced by a Periodic Dzyaloshinskii-Moriya Interaction,” *Physical Review Letters*, vol. 122, no. 6, p. 067 204, Feb. 13, 2019. arXiv: 1806.08333 (cit. on pp. 4, 51).
- [141]G. Gubbiotti, X. Zhou, Z. Haghshenasfard, *et al.*, “Interplay between intra- and inter-nanowires dynamic dipolar interactions in the spin wave band structure of Py/Cu/Py nanowires,” *Scientific Reports*, vol. 9, no. 1, p. 4617, Dec. 2019 (cit. on p. 4).
- [142]A. Aharoni, *Introduction to the Theory of Ferromagnetism* (Oxford Science Publications 109), 2nd ed. Oxford ; New York: Oxford University Press, 2000, 319 pp. (cit. on pp. 11, 13).
- [143]N. A. Lemos, *Analytical Mechanics*, English edition. Cambridge ; New York, NY: Cambridge University Press, 2018, 459 pp. (cit. on p. 12).
- [144]Y. Henry, O. Gladii, and M. Bailleul. “Propagating spin-wave normal modes: A dynamic matrix approach using plane-wave demagnetizing tensors.” arXiv: 1611.06153 [cond-mat]. (Nov. 18, 2016), [Online]. Available: <http://arxiv.org/abs/1611.06153> (visited on Nov. 29, 2021) (cit. on pp. 15, 21, 39).
- [145]A. Zangwill, *Modern Electrodynamics*. Cambridge: Cambridge University Press, 2013, 976 pp. (cit. on p. 17).
- [146]G. Dieterle, J. Förster, H. Stoll, *et al.*, “Coherent excitation of heterosymmetric spin waves with ultrashort wavelengths,” *Physical Review Letters*, vol. 122, no. 11, p. 117 202, Mar. 21, 2019. arXiv: 1712.00681 (cit. on p. 39).
- [147]R. Damon and J. Eshbach, “Magnetostatic modes of a ferromagnet slab,” *Journal of Physics and Chemistry of Solids*, vol. 19, no. 3-4, pp. 308–320, May 1961 (cit. on p. 39).

- [148]O. Gladii, M. Haidar, Y. Henry, M. Kostylev, and M. Bailleul, “Frequency nonreciprocity of surface spin wave in permalloy thin films,” *Physical Review B*, vol. 93, no. 5, p. 054 430, Feb. 29, 2016 (cit. on pp. 39, 51).
- [149]M. Jamali, A. K. Smith, and J.-P. Wang, “Nonreciprocal behavior of the spin pumping in ultra-thin film of CoFeB,” *Journal of Applied Physics*, vol. 119, no. 13, p. 133 903, Apr. 7, 2016 (cit. on p. 39).
- [150]S. Shichi, N. Kanazawa, K. Matsuda, *et al.*, “Spin wave isolator based on frequency displacement nonreciprocity in ferromagnetic bilayer,” *Journal of Applied Physics*, vol. 117, no. 17, p. 17D125, May 7, 2015 (cit. on p. 41).
- [151]G. Gubbiotti, S. Tacchi, M. Madami, *et al.*, “Brillouin light scattering studies of planar metallic magnonic crystals,” *Journal of Physics D: Applied Physics*, vol. 43, no. 26, p. 264 003, Jul. 7, 2010 (cit. on p. 42).
- [152]P. Malagò, L. Giovannini, R. Zivieri, P. Gruszecki, and M. Krawczyk, “Spin-wave dynamics in permalloy/cobalt magnonic crystals in the presence of a nonmagnetic spacer,” *Physical Review B*, vol. 92, no. 6, p. 064 416, Aug. 12, 2015 (cit. on p. 44).
- [153]M. A. Morozova, A. Y. Sharaevskaya, O. V. Matveev, E. N. Beginin, and Y. P. Sharaevskii, “Numerical modeling of wave processes in coupled magnonic crystals with periods shifted relative to each other,” *Physics of Wave Phenomena*, vol. 24, no. 1, pp. 1–6, Jan. 2016 (cit. on p. 48).
- [154]M. A. Morozova, A. Y. Sharaevskaya, A. V. Sadovnikov, *et al.*, “Band gap formation and control in coupled periodic ferromagnetic structures,” *Journal of Applied Physics*, vol. 120, no. 22, p. 223 901, Dec. 14, 2016 (cit. on p. 48).
- [155]J. Wei, Z. Zhu, C. Song, *et al.*, “Annealing influence on the exchange stiffness constant of Permalloy films with stripe domains,” *Journal of Physics D: Applied Physics*, vol. 49, no. 26, p. 265 002, Jul. 6, 2016 (cit. on p. 56).
- [156]M. Pousthomis, E. Anagnostopoulou, I. Panagiotopoulos, *et al.*, “Localized magnetization reversal processes in cobalt nanorods with different aspect ratios,” *Nano Research*, vol. 8, no. 7, pp. 2231–2241, Jul. 2015 (cit. on p. 56).
- [157]H. Yu, G. Duerr, R. Huber, *et al.*, “Omnidirectional spin-wave nanograting coupler,” *Nature Communications*, vol. 4, no. 1, p. 2702, Dec. 2013 (cit. on p. 60).
- [158]I. Bertelli, J. J. Carmiggelt, T. Yu, *et al.*, “Magnetic resonance imaging of spin-wave transport and interference in a magnetic insulator,” *Science Advances*, vol. 6, no. 46, eabd3556, Nov. 13, 2020 (cit. on p. 60).

- [159]H. Yu, R. Huber, T. Schwarze, *et al.*, “High propagating velocity of spin waves and temperature dependent damping in a CoFeB thin film,” *Applied Physics Letters*, vol. 100, no. 26, p. 262 412, Jun. 25, 2012 (cit. on p. 64).
- [160]C. Liu, J. Chen, T. Liu, *et al.*, “Long-distance propagation of short-wavelength spin waves,” *Nature Communications*, vol. 9, no. 1, p. 738, Dec. 2018 (cit. on p. 64).
- [161]D. Goll, A. Breitling, L. Gu, P. A. van Aken, and W. Sigle, “Experimental realization of graded L10-FePt/Fe composite media with perpendicular magnetization,” *Journal of Applied Physics*, vol. 104, no. 8, p. 083 903, Oct. 15, 2008 (cit. on p. 65).
- [162]M. Marcellini, M. Pärnaste, B. Hjörvarsson, and M. Wolff, “Influence of the distribution of the inherent ordering temperature on the ordering in layered magnets,” *Physical Review B*, vol. 79, no. 14, p. 144 426, Apr. 22, 2009 (cit. on p. 65).
- [163]B. J. Kirby, S. M. Watson, J. E. Davies, *et al.*, “Direct observation of magnetic gradient in Co/Pd pressure-graded media,” *Journal of Applied Physics*, vol. 105, no. 7, p. 07C929, Apr. 2009 (cit. on p. 65).
- [164]V. Alexandrakis, D. Niarchos, K. Mergia, *et al.*, “Magnetic properties of graded A1/L10 films obtained by heat treatment of FePt/CoPt multilayers,” *Journal of Applied Physics*, vol. 107, no. 1, p. 013 903, Jan. 2010 (cit. on p. 65).
- [165]J. S. Chen, L. S. Huang, J. F. Hu, G. Ju, and G. M. Chow, “FePt–C graded media for ultra-high density magnetic recording,” *Journal of Physics D: Applied Physics*, vol. 43, no. 18, p. 185 001, May 12, 2010 (cit. on p. 65).
- [166]L. Fallarino, B. J. Kirby, and E. E. Fullerton, “Graded magnetic materials,” *Journal of Physics D: Applied Physics*, vol. 54, no. 30, p. 303 002, Jul. 29, 2021 (cit. on pp. 65, 73).
- [167]K. Y. Guslienko, S. O. Demokritov, B. Hillebrands, and A. N. Slavin, “Effective dipolar boundary conditions for dynamic magnetization in thin magnetic stripes,” *Physical Review B*, vol. 66, no. 13, p. 132 402, Oct. 4, 2002 (cit. on p. 69).
- [168]M. L. Green, I. Takeuchi, and J. R. Hattrick-Simpers, “Applications of high throughput (combinatorial) methodologies to electronic, magnetic, optical, and energy-related materials,” *Journal of Applied Physics*, vol. 113, no. 23, p. 231 101, Jun. 21, 2013 (cit. on p. 73).
- [169]R. Bali, S. Wintz, F. Meutzner, *et al.*, “Printing Nearly-Discrete Magnetic Patterns Using Chemical Disorder Induced Ferromagnetism,” *Nano Letters*, vol. 14, no. 2, pp. 435–441, Feb. 12, 2014 (cit. on p. 74).

- [170]F. Röder, G. Hlawacek, S. Wintz, *et al.*, “Direct Depth- and Lateral- Imaging of Nanoscale Magnets Generated by Ion Impact,” *Scientific Reports*, vol. 5, no. 1, p. 16 786, Dec. 2015 (cit. on p. 74).
- [171]M. Nord, A. Semisalova, A. Kákay, *et al.*, “Strain Anisotropy and Magnetic Domains in Embedded Nanomagnets,” *Small*, vol. 15, no. 52, p. 1 904 738, Dec. 2019 (cit. on p. 74).

Colophon

This thesis was typeset with $\text{\LaTeX}2_{\epsilon}$. It uses the *Clean Thesis* style developed by Ricardo Langner. The design of the *Clean Thesis* style is inspired by user guide documents from Apple Inc.

Download the *Clean Thesis* style at <http://cleanthesis.der-ric.de/>.

